Steady-State and Transient Diesel Soot Emissions:
Development of a Mean Value Soot Model and Exhaust-Stream and In-Cylinder Measurements

Patrick Kirchen

2008

Steady-State and Transient Diesel Soot Emissions:
Development of a Mean Value Soot Model and Exhaust-Stream and In-Cylinder Measurements

by
Patrick Kirchen
born August 25, 1978
Citizen of Belpberg, BE and Canada

A thesis submitted to the ETH Zurich for the degree of
Doctor of Sciences

Accepted based on the recommendations of
Prof. Dr. K. Boulouchos, examiner
Prof. Dr. L. Guzzella, co-examiner

2008

Such is the way of the world
You can never know
Just where to put all your faith
And how will it grow

Gonna rise up
Burning back holes in dark memories
Gonna rise up
Turning mistakes into gold

Such is the passage of time
Too fast to fold
And suddenly swallowed by signs
Low and behold

Gonna rise up
Find my direction magnetically
Gonna rise up
Throw down my ace in the hole

- Eddie Vedder

Acknowledgements

Of all the pages in this booklet, this one is by far the most satisfying and enjoyable to write. There are many who have made the work presented here possible, but also many more who have made it bearable - or dare I say, enjoyable.

First and foremost, I would like to thank Professor Konstantinos Boulouchos for his never-ending support, encouragement, patience, and motivation. The German word *Doktorvater* doesn't really exist in English, though after these last three and a half years, I have grown rather fond of the term and am even more pleased that I have been fortunate enough to work with such an all-encompassing "doctor-father".

I would like to thank the numerous colleagues at the Measurement and Control Laboratory for the availability of the OM611 testbench, the very pleasant collaboration, and their understanding when the measurements took a little longer than planned. My sincerest appreciation also goes to Professor Lino Guzzella for his readiness to act as co-examiner.

Within the Laboratory for Aerothermochemistry and Combustion Systems, there are so many people I would like to thank that I can't list them all individually. I must, however, thank Peter Obrecht not only for his help with the thermodynamic analyses and instrumentation, but also for his patience and willingness to proofread countless "German" documents which I concocted. My thanks also go to our technicians who made my life that much easier. Finally I'd like to thank all those from the LAV with whom I've shared: a coffee; a lunch; a dinner; one or more beers; a ride in the cold, wet dark (or on a hot, dry afternoon); a late night forum on the beach; or a casual helicopter flight. Thank you all for the wonderful times.

Abstract

The soot emissions from diesel engines have serious health implications and have also been seen to influence the air quality and climate and, as such, must be reduced. To aid in the optimal operation of modern diesel engines, a mean value soot model (MVSM) was developed and validated for the rapid calculation of the engine soot emissions from diesel engines, operating under steady state and transient conditions. In addition, experimental investigations were carried out using exhaust stream and in-cylinder instrumentation to elucidate the influences of transient engine operation and fuel composition on the soot emissions.

The MVSM was developed through the reduction of an existing crank angle resolved soot model, based on the consideration of representative mixture states for combustion, soot formation, and soot oxidation. While the crank resolved model required the temporally resolved cylinder pressure, heat release rate, and fuel injection rate histories, the developed MVSM required only parameters available from the engine control unit. Because of this significant restriction in available information, the MVSM uses 16 model parameters to describe the combustion and soot formation and oxidation processes, which were determined for each engine and fuel combination using evolutionary algorithms. The parameterized MVSM was capable of calculating the engine out soot emissions in 10 ms per operating point, compared to 5 s required by the crank angle resolved model.

The MVSM was validated against steady-state exhaust stream soot measurements from two different engines operating with three different fuels, as well as for transient operation on one engine. It was found that the MVSM was capable of reproducing the qualitative and quantitative soot emission trends for the considered fuels and engines over a wide range of engine operating points. From the steady-state validation and sensitivity analyses, it was found that an accurate estimate of the EGR rate and intake charge temperature are required

to ensure acceptable performance from the MVSM. Given that these inputs were available with sufficient temporal resolution, the MVSM was capable of reproducing the qualitative and in part quantitative soot emissions tendencies during tip-in (load changes) and acceleration (engine speed changes) transients. The MVSM had difficulty consistently reproducing the magnitude of the soot emissions "spike", but it was capable of reproducing a short term reduction observed immediately after the transient. The strong dependance of the calculated soot emission on the temperature was attributed to the use of a equivalence ratio - temperature map to describe the soot formation process. In general, the MVSM was found to consider the formation processes almost exclusively while changes in oxidation relevant parameters had a relatively small influence on the calculated soot emissions.

The MVSM has shown itself to be capable of predicting the soot emissions during steady state operation over a wide range of operating conditions on different engines, with different fuels. It does however require further development in order to more accurately calculate the soot emissions during transient engine operation. To this end, the insensitivity of the MVSM to oxidation parameters must be explored and remedied. Additionally, the influences of transient operation on the soot emissions could be further investigated and used for the further development of the MVSM with particular regard to transient operation.

In addition to serving as a basis for the validation of the MVSM, the steady state and transient measurements were used to gain insight as to the underlying mechanisms of soot formation and oxidation. To validate the use of in-cylinder pyrometry to describe soot emissions tendencies noted in the exhaust stream, the in-cylinder particle concentrations at the end of oxidation were compared with the exhaust stream soot measurements. The correlation coefficient between the two methods was found to range from $R^2 = 0.42$ to $R^2 = 0.87$, depending on the cylinder under consideration and the sensor being used. During steady state measurements with a reference fuel and a second fuel with a lower aromatic content and evaporation temperature, the soot emissions were seen to be lower with the second fuel. Through the use of in-cylinder pyrometry measurements, the lower engine out emissions were attributed to reduced in cylinder soot formation, caused by the lower aromatic content.

From the exhaust stream soot measurements during the tip-in and acceleration transients, an increase in the soot emissions compared to steady-state operation was seen for the tip-in transients, though the acceleration transients

were not seen to have a considerable influence on the soot emissions. The increase in the soot emissions during the tip-in transients, particularly those of short duration at low engine speeds, was attributed a short-term oxygen deficit as quantified by the global relative oxygen-fuel ratio. This hypothesis was validated by the in-cylinder measurements which indicated that the soot emission increase corresponds with an unchanged soot formation process (compared to steady-state operation) coupled with a slow and incomplete oxidation.

Zusammenfassung

Die Russemissionen eines Dieselmotors haben beträchtliche Einflüsse auf die Gesundheit, Luftqualität und das globale Klima und müssen deshalb reduziert werden. Um die Entwicklung moderner Dieselmotoren gezielt auf minimale Russemissionen zu unterstützen, wurde ein Mittelwert Russmodell (MWRM) für die schnelle Vorausberechnung der Russemissionen beim stationären und transienten Betrieb entwickelt und validiert. Weiter wurden Untersuchungen anhand von Abgasstrom- und In-Zylindermessungen durchgeführt, um den Einfluss des transienten Betriebs und der Kraftstoffeigenschaften auf die Russemissionen zu bestimmen.

Das MWRM wurde durch die Reduktion eines bestehenden, kurbelwinkelaufgelösten Modells, unter der Berücksichtigung von repräsentativen Gemischzuständen für die Verbrennung, Russbildung und -oxidation hergeleitet. Während das kurbelwinkelaufgelöste Russmodell zeitlich aufgelöste Verläufe des Zylinderdrucks, der Brennstoffumsatzrate, und der Einspritzrate benötigt, berücksichtigt das MWRM lediglich Betriebsparameter als Modelleingänge, die bei einem serienmässigen Steuergerät vorhanden sind. Durch diese starke Einschränkung an verfügbaren Informationen, werden 16 Modellparameter verwendet um die Verbrennung, sowie die Russbildungs und -oxidationsprozesse zu beschreiben. Jede Motor - Kraftstoff - Kombination benötigt ein neues Set dieser Modellparameter die mittels evolutionärer Algorithmen bestimmt werden. Nach einer geeigneten Parametrierung ist das MWRM in der Lage, die zyklusspezifischen Russemissionen mit einer Rechenzeit von 10 ms zu berechnen, im Vergleich zu den 5 s, die das kurbelwinkelaufgelöste Modell benötigt. Anhand von Abgasstrom Russmessungen von zwei Motoren für den Betrieb mit insgesamt drei Kraftstoffen, wurde das MWRM parametriert, validiert, und mittels Sensitivitätsanalysen charakterisiert. Nach dieser Parametrierung konnte das MWRM die qualitativen und quantitativen Russemissionstendenzen für die berücksichtigten Kraftstoffe und Motoren über einen weiten Bere-

ich von Betriebspunkten wiedergeben ($R^2 \approx 0.7...0.9$). Bei der Validierung des stationären Betriebs und von zusätzlich durchgeführten Sensitivtätsanalysen wurde ersichtlich, dass eine genaue Kenntnis der AGR Rate und der Gemischtemperatur beim Schliessen des Einlassventils für eine optimale Leistungsfähigkeit des MWRMs nötig ist. Sind diese Grössen gut charakterisiert, ist das MWRM in der Lage, die qualitativen und zum Teil quantitativen Russemissionen während Anfahr-, bzw. Beschleunigungstransienten (Last- bzw. Drehzahlsprünge) vorherzusagen. Obwohl das MWRM die Russemissionsspitzen während den Transienten nur teilweise wiedergeben konnte, wurde die kurzfristige Reduktion der Russemissionen nach der Transiente auch bei der Berechnung beobachtet. Die starke Abhängigkeit der berechneten Russemissionen von der Temperatur beim Schliessen des Einlassventils, wurde auf die Modellierung der Kinetik der Russbildung und -oxidation, die auf einem Äquivalenzverhältnis - Temperatur Kennfelds beruht, zurückgeführt. Im allgemeinen wird die Russformation vom Model sehr stark gewichtet im Gegensatz zur Russoxidation. Dies führt dazu, dass oxidationsrelevante Betriebs- und Modellparameter nur einen vernachlässigbaren Einfluss auf den berechneten Russemissionen haben.

Zusätzlich zu der Parametrierung und Validierung des MWRMs, wurden die Russmessungen verwendet, um die grundlegenden Russbildungs und -oxidations - Mechanismen zu untersuchen. Um die Zulässigkeit von In-Zylinder Pyrometriemessungen zur Beschreibung von Tendenzen im Abgasstrom zu validieren, wurde der In-Zylinder Russwert zum Ende der Oxidation mit dem Russ im Abgasstrom verglichen. Der Korrelationskoeffizient zwischen den beiden Messmethoden liegt im Bereich zwischen R^2=0.42 und 0.87, je nachdem welcher Zylinder zur In-Zylinderrussmessung berücksichtigt worden ist. Bei der Verwendung eines alternativen, Diesel-ähnlichen Kraftstoffs, mit einer tieferen Zetanzahl, einem tieferen Aromatenanteil, und einer tieferen Verdampfungstemperatur, wurden tiefere Abgas Russemissionen bei allen betrachteten Betriebspunkten gemessen. Anhand der Pyrometrie Messungen, konnte eine reduzierte Russbildung festgestellt werden, was durch den tieferen Aromatenanteil zu erklären ist.

Bei den Abgasstrom-Messungen wurde eine Erhöhung der Russemission bei Anfahrtransienten gegenüber stationärem Betrieb festgestellt. Bei den Beschleunigungstransienten hingegen, konnte keine signifikante Änderung der Russemissionen gegenüber stationärem Betrieb festgestellt werden. Die Erhöhung der Russemissionen bei den Anfahrtransienten, besonders bei tieferen Drehzahlen und kurzen Transienten, wurden auf einen kurzfristigen Sauerstoff-

mangel zurückgeführt. Dies wurde von den in-Zylinder Messungen bestätigt. Die Erhöhung der Russemissionen entspricht dem Anstieg der Russbildung im Zylinder, die entsprechende Veränderung in der Russoxidation trat jedoch erst einige Zyklen später auf.

Das MWRM hat sich für die Berechnung der stationären Russemissionen, über einen breiten Betriebsbereich auf unterschiedlichen Motoren mit unterschiedlichen Kraftstoffen bewährt. Jedoch ist eine Weiterentwicklung notwendig, um genauere Berechnungen für den transienten Betrieb zu ermöglichen. In diesem Rahmen ist eine detaillierte Untersuchung der Oxidationsempfindlichkeit des MWRMs empfehlenswert. Zusätzlich könnten Erkenntnisse der Beeinflussung des transienten Betriebs der Russemissionen in der Weiterentwicklung des MWRMs einbezogen werden.

Contents

List of Figures

List of Tables

Chapter 1

Introduction

For four days in 1952, a thick fog caused by an inversion layer and black smoke from coal combustion and diesel buses covered London, England. An official estimate indicates that 4000 people died as a result of *The Great Fog*, though other sources put it as high as 12000 [109].

In 1974 a 14 year landmark study began in 6 American cities to determine the influence of air pollution on human health [27]. After accounting for the occupational exposure and detailed smoking history of the 8111 participants, *The Harvard Six Cities Study* found an undeniable increase in mortality for increasing fine particle[1] and sulfate particle concentration. The increase in mortality caused by these particles was greatest among all of the airborne pollutants considered, including sulfur dioxide and nitrogen dioxide.

The Swiss Federal Office for the Environment has estimated that over 3 million Swiss residents are exposed to excessive levels of fine particles. An estimated 3700 premature deaths are caused annually in Switzerland by fine particles, the most dangerous of which are those emitted by diesel engines [18].

The particulate emissions from combustion, in particular diesel engines, are well known to influence the health of living organisms and must therefore be reduced. This work outlines the development and validation of a numerical

---

[1]Fine particles were defined as those smaller than 2.5μm, now commonly referred to as PM2.5.

model capable of predicting the soot emissions from diesel engines, suitable for the use with engine control systems to optimize engine operation for minimum soot emissions.

1.1   Why are particles so bad?

The particles generated by diesel engines have a diameter on the order of 100 nm and are small enough to be inhaled deep into the lungs. Once they are in the lungs they can be deposited where they result in inflammatory reaction and can act as carcinogens [90]. If the particles are small enough, they can be absorbed into the blood stream and carried and deposited throughout the body. This includes transport to the liver, spleen, kidneys, heart, immune system, and central nervous system, including the brain [55], where they can once again act as carcinogens.

In addition to their carcinogenic and inflammatory influences, the particles can also have cardiovascular implications. For example, if the central nervous system is influenced, variations in the heart rate may result (cardiac arrhythmia) [67]. Additionally there is strong experimental evidence indicating that particles may result in atherogenesis (hardening of the arteries), which can result in a blockage or rupture of an artery, leading to a myocardial infarction (heart attack) [78], [56]. It is well accepted that combustion generated nanoparticles have an influence, though the pathways are generally not yet well understood. While PM2.5 and PM0.1 are known to have health effects, the influences of coarse (i.e. larger) particles should not be excluded.

Ambient particles can also influence the climate and atmospheric visibility. Particles influence the climate, in particular Earth's radiative balance through two effects: 1) the direct effect by which particles absorb and scatter radiation; and 2) the indirect effect through which particles modify the formation and properties of clouds [37]. The net effect, however is a resultant cooling of the atmosphere through the reflection of sunlight [43].

1.2   So, what can be done?

In light of the influences which diesel particles have on the climate and, more importantly, human health, the emission limits for diesel vehicles are becoming evermore stringent, as outlined in table 1.2. In the recent years, the permitted particle mass emissions (PM) have decreased drastically in both North America

	Passenger Vehicles			Heavy Duty		
	PM (mg/km)	NOx (mg/km)	Date	PM (g/kWh)	NOx (g/kWh)	Date
Euro 4	25	250	2005.1	0.02	3.5	2005.1
Euro 5	5	180	2009.9	0.02^b	2	2008.1
Euro 6	5	80	2014.9	0.01^b	0.4	2013.4
US 2007	6^a	43	2007	0.01	3.4	2007
US 2010				0.01	0.3	2010

Table 1.1: Comparison of European and American soot and NOx emission regulations for passenger and heavy duty diesel vehicles. [a] Fleet average value. [b] A number limit will also be introduced, likely on the order of $5x10^{11}$ particles/km.

and Europe. In Europe, the EURO 5 and later regulations will also include a number limit, to reduce the number of fine particles which is a relevant parameter from a health effects point of view, but under-represented by mass limits. Shown also in table 1.2 are the NO_x limits, for reference purposes, as a reduction in soot typically results in an increase in NO_x (for in-cylinder measures).

While in-cylinder means such as increased injection pressures or, advanced injection strategies have improved particle emissions, the newest regulations will most certainly require the use of an exhaust stream Diesel Particle Filter (DPF). A DPF mechanically removes the particles from the exhaust stream with efficiencies of approximately 97% by mass, and up to 99.9% by particle number [28]. The use of DPFs however, introduces increased backpressure, resulting in decreased fuel-economy and hence increased CO_2 emissions. Eventually the DPF becomes so laden with particles, that it must be regenerated, that is, the particles must be oxidized. The surface oxidation of soot in a non-catalyzed DPF requires temperatures of at least 600°C, which is typically higher than that seen during regular passenger car operation. In order to increase the exhaust gas temperature, the combustion can be modified, or additional fuel injected late in the combustion process, though this results in an additional increase in the fuel consumption [84]. Thus, some means of minimizing the DPF loading and regeneration frequency is desirable to reduce the fuel consumption penalty of a DPF. Currently no sensors capable of measuring the raw particle concentration are available for production applications [105],

and as such the filter state is commonly estimated using a differential pressure measurement across the filter. This method however, is not a direct measure of the particle emissions and does not provide time resolved information of the raw particle emissions. Furthermore, to minimize the raw particle emissions from the engine, it is necessary to be able to understand the particle formation processes during transient engine operation, as this has a considerable impact on the overall particle emissions [69].

1.3 Outline of this work

In light of the considerations listed above, this work aims to develop and validate a mean value soot model (MVSM) which:

1. is capable predicting the soot emissions throughout the entire steady-state engine operating map;

2. is capable predicting the soot emissions for engine operating conditions for which it was not parameterized, for example during transient engine operation;

3. requires a minimum of measured operating conditions for its parameterization;

4. uses only input parameters available from a standard engine control unit (ECU) or other realtime models;

5. has calculation times less than one engine cycle (20 ms at 6000 rpm for a four stroke engine).

The latter two points are aimed at ensuring that the developed MVSM is suitable for implementation with real ECUs.

After a review of the current understanding of soot emission fundamentals, measurement techniques and modeling methodologies in chapter 2, the development of the MVSM is outlined in chapter 3. Using the methodologies outlined in chapter 4, the exhaust stream and in-cylinder soot emissions measured during steady state and transient operation are presented in chapter 5. The various soot measurement methodologies are compared, and the influence of the engine operating parameters on the soot emissions, particularly during transient operation are investigated. Finally in chapter 6 the MVSM is parameterized and validated using the measured steady state transient soot emissions. Finally, several sensitivity analyses are carried out to gain further understanding of the behavior of the MVSM.

Chapter 2

State of the Art

2.1 Introduction

Although the modern diesel engine is an efficient and attractive power source for mobile and stationary applications, its particle emissions are a problem which must be addressed. As such, the legislation governing the diesel engine emissions is becoming evermore stringent, as shown in table 1.2. These emission limits will necessitate the implementation of exhaust aftertreatment systems (closed diesel particulate filters, and NOx reduction systems), though it is still necessary to understand the processes governing the formation of the particles during combustion, as well as how they can be characterized. In addition, knowledge of the influences of engine operating parameters on the particle emissions during both steady state and transient operation is needed so that the diesel engine operation can be optimized to minimize all emissions.

2.2 Particle Formation Fundamentals

The particles emitted from a modern diesel engine have a structure similar to that shown in figure 2.1, where an aggregate composed of many smaller primary particles can be seen. Such aggregate particles are formed during combustion and are the result of two competing processes: particle formation and particle oxidation. After the particles have been formed, other compounds can be absorbed onto them, influence their composition. In general, particles composed of elementary carbon are referred to as *soot*, though the particles
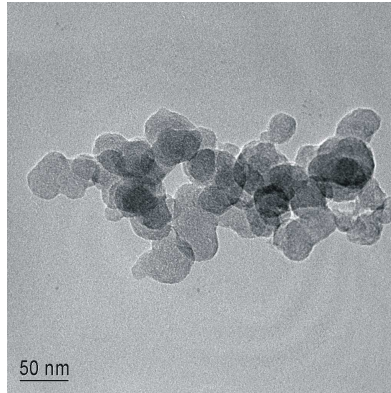
Figure 2.1: Representative particle from the exhaust stream of a modern diesel engine [70].

emitted by diesel engines are not pure soot. The fraction of elementary organic carbon in a particle can vary largely depending on the operating point, engine, and fuel being considered. This work will focus on elementary carbon (i.e. soot) fraction emitted from diesel engines, though the fundamentals of particle formation will be included for completeness.

The particle mass is an important measure of the particulate emissions from diesel engines, though the particle number concentration is also of great importance, especially from a health effect standpoint. The dominant particle formation and oxidation mechanisms and their influences on the particle mass, number and size are briefly outlined below.

2.2.1   Formation

The generally accepted particulate formation mechanism consists of four steps: fuel decomposition and formation of soot precursors and polycyclic aromatic hydrocarbons (PAH); particle inception; surface growth; and particle coagulation and agglomeration. These processes are shown graphically in figure 2.2 and are discussed briefly below.
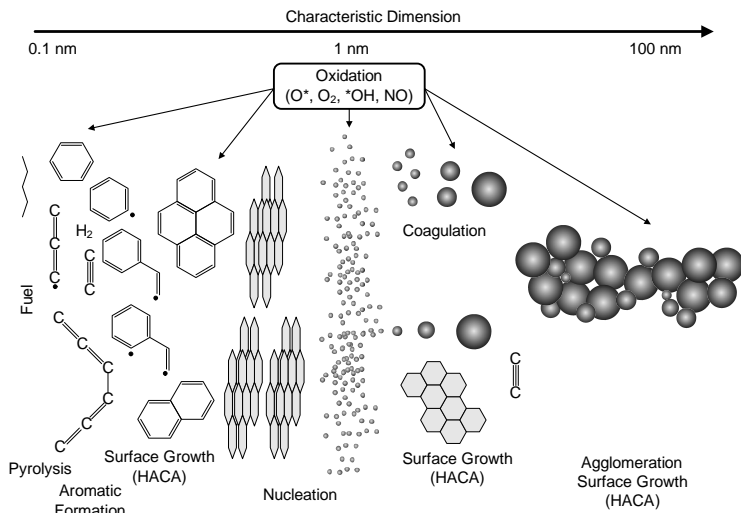
Figure 2.2: Schematic representation of the fundamental soot formation mechanisms during combustion. Adapted from [57], [13], [92] and [101]

PAH Formation

The building blocks for particle formation are aromatic hydrocarbon rings, which can be formed through pyrolysis of the injected fuel or may already be present in fuels with higher aromatic fractions. These first aromatic rings undergo planar growth, primarily by Hydrogen Abstraction, C2H2 Addition (HACA) [32], in which aromatic rings repeatedly undergo dehydrogenation by a hydrogen atom, followed by reaction with an acetylene molecule. Because both hydrogen atoms and acetylene are required for the HACA mechanism, this process is largely limited to the primary reaction zone, where the respective concentrations and temperature are sufficiently high. The rate limiting step is the formation of the first aromatic rings, which is also a function of the fuel, though the subsequent planar growth by the HACA mechanism is not strongly influenced by the fuel [60].

Particle Inception and Nucleation

After the planar PAH growth, the gas phase PAHs undergo transition to solid particles in a process known as particle inception or nucleation. The first

particles or nuclei are on the order of 1-2 nm and while having only a very small size, serve as the center for the subsequent surface growth. Thus the number of nucleation particles will have a strong influence on the final soot mass, though they themselves have only a small contribution to the mass. Fuels with high sulfur fractions result in higher particle emissions, as the sulfates can act as nucleation sites for the particles. Note that this will not be considered soot particles as the are not composed of elementary carbon.

Surface Growth

Once the first particles are formed, they undergo surface growth which adds considerable mass. Surface growth takes place by the adsorption of vapor phase hydrocarbons onto the particle, as well as through the HACA mechanism. Both of these processes require the presence of chemically active sites on the particle. As the particles get larger through surface growth, there are fewer and fewer site available and the surface growth rate decreases, a process termed surface aging.

Coagulation and Agglomeration

When two particles collide, they may form a new particle either through coagulation or agglomeration. In both cases, this results in an increase in the particle size, a decrease in the particle number, and no change in the soot volume fraction. When two small, relatively young, spherical particles collide they eventually form one new spherical particle, given that there is a sufficiently fast surface growth (coagulation). If the collision partners are old, large particles with fewer active sites, the surface growth will not be sufficiently fast for coagulation and an aggregate structure will result (agglomeration) leading to the structure shown in figure 2.1.
Figure 2.3 illustrates representative histories of the particle number, particle diameter, and soot volume fraction, which can be used to understand the individual effects of each of the particle formation mechanisms introduced above.

2.2.2   Oxidation

Particles can be oxidized during all stages of their formation, thereby reducing their number, diameter, and mass. During the early stages of soot formation when the first aromatic rings are being formed, the presence of oxygen inhibits
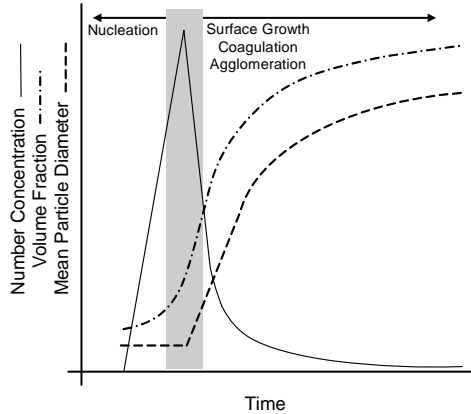
Figure 2.3: Representative particle number, volume fraction and particle diameter histories during soot formation. Adapted from [6]

the formation of a new ring or surface growth by reacting with an active site. Through a numerical investigation, it was found that the oxidation of the aromatics is largely a function of the O_2 concentration and not strongly influenced by the OH concentration [31]. Once the particles have been formed, it is also possible that they themselves are oxidized. In diesel engines, the exhausted soot concentration can be orders of magnitude lower than the maximum soot concentration measured during the combustion, due to oxidation. The difference between these two concentrations is due to oxidation which takes place given sufficiently high temperatures (>1300[K], [98]) and an excess of oxygen. For a soot particle to be oxidized, the oxygen must be adsorbed onto the soot particle after which it reacts with the carbon. The most common means of describing the particle oxidation is that presented in [74] where two types of reactive sites on the particle are considered to be available for oxidation. Though [74] considers only the partial pressure of oxygen, the OH radical is also assumed to play an important role in particle oxidation.

2.3   Characterization of Particle Emissions

Particulate emissions can be characterized by their mass concentration, number concentration, size, composition, opacity of the exhaust stream, or paper blackening. Depending on the measured quantity, the measurement is car-

ried out in the exhaust stream or within the combustion chamber itself. Only the most popular methods are presented here, though a detailed discussion of these and other methods is available in the literature [21].

2.3.1 Mass Concentration

Several methods exist by which the particulate mass concentration can be measured in the exhaust stream. The gravimetric method used for type approval measurements, draws a known quantity of exhaust gas is through a filter, onto which the particles are deposited. By measuring the mass of the filter before and after the sample is drawn through, the particle mass can be determined. Additionally, the composition of the deposited material can be analysed using coulometry to determine the elementary and organic carbon fractions. In a similar method, the paper blackening caused by drawing the sample through the filter can be measured, which results in the widely used Filter Smoke Number (FSN). It has been shown that the FSN correlates well with the elementary carbon concentration $[EC]$ according to the relationship given in equation 2.1.

$$[EC] = \frac{5.32 \cdot FSN \cdot e^{0.31 \cdot FSN}}{0.405} \tag{2.1}$$

where $[EC]$ is given in mg/m^3 at STP. Both the gravimetric and FSN methods are suited only to steady state measurements, as some time is required to extract the sample and deposit it on the filter (on the order of $1\,min$).

A photo-acoustic soot sensor, for example the AVL Micro Soot Sensor (MSS) can provide time resolved exhaust stream soot concentration measurements [87]. Using a partial flow dilution system, a diluted exhaust stream is routed through a chamber with optical accesses on either end, through which a modulated laser beam is guided. When the laser beam strikes a particle, the particle and its surrounding gases are heated and begin to expand. Because the laser beam is modulated, the heating process is periodic and the gas undergoes a periodic expansion and contraction process resulting in a pressure wave, the amplitude of which can be recorded using a microphone. It has been shown that the amplitude of the pressure wave correlates well with the elementary carbon concentration in the diluted exhaust stream and is well suited to the measurement of the soot emissions during transient engine operation. The commonly used opacimeter (for example AVL 439) is another optical technique suitable for determining the particle concentration during transient engine operation.

The particle concentration can be correlated to the light extinction measured by passing light through the exhaust gas.

2.3.2 Number Concentration

Of particular interest from a health effects standpoint, is the size and number of particles in the exhaust stream, as small particles which have only a very small mass are those considered the most dangerous. The size and number of particles are typically characterized by their size distribution, which requires counting the number of particles at a given size. Particle size can be classified using the particle mobility diameter as is done with the commonly used Scanning Mobility Particle Sizer (SMPS) [100] or according to the aerodynamic diameter, as is done when using an Electrical Low Pressure Impactor (ELPI) [45]. The number of particles can be determined either through direct counting using a Condensation Particle Counter (CPC), or by charge counting methods. After condensing liquid onto the particle, a CPC counts the number of particles on the basis of their light scattering. Alternatively, the particles can be charged (using corona or diffusion chargers) and then counted by measuring the electrical current generated when the particles are deposited on an electrical filter.

2.3.3 Pyrometry

By using the method of multi-color pyrometry, it is possible to measure the temporally (and potentially spatially) resolved particulate concentration and temperature in the combustion chamber during combustion. The light radiated from hot particles during combustion is recorded at two or more wavelengths and used to determine the particle temperature and the so-called KL factor (proportional to concentration) [41]. The radiation intensity emitted from a grey soot cloud at a given wavelength and temperature, $i_\lambda(T)$, is measured using a pyrometer. For the radiation emitted from a blackbody to have the same intensity, $i_{b,\lambda}(T_{app})$, it would have to be at the apparent temperature, T_{app}, where the two intensities can be related using the emissivity of the soot cloud at the considered wavelength, ε_λ:

$$\varepsilon_\lambda = \frac{i_{b,\lambda}(T_{app})}{i_{b,\lambda}(T)} \tag{2.2}$$

The radiation intensity from a blackbody at a given temperature and wavelength can be determined using Planck's distribution,

$$i_{b,\lambda}(T) = \frac{2C_1}{\lambda^5 \left(\exp\left(\frac{C_2}{\lambda T} \right) - 1 \right)} \tag{2.3}$$

where $C_1 = 3.74 \cdot 10^8 \, \text{W} \mu \text{m}^4/\text{m}^2$ and $C_2 = 1.44 \cdot 10^3 \, \mu \text{mK}$. The monochromatic emissivity of a soot cloud is commonly described using the empirical correlation suggested by Hottel and Broughton [41][1]:

$$\varepsilon_\lambda = 1 - \exp\left(-\frac{KL}{\lambda^\alpha} \right) \tag{2.4}$$

where K is the absorption coefficient, L is the relevant optical path length and α is a constant. By combining equations 2.2, 2.3, and 2.4, the so called KL factor can be defined as

$$KL = -\lambda^\alpha \ln \left(1 - \frac{\exp\left(\frac{C_2}{\lambda T} \right) - 1}{\exp\left(\frac{C_2}{\lambda T_{app}} \right) - 1} \right) \tag{2.5}$$

If radiation is considered at two different wavelengths, λ_1 and λ_2, and assuming that KL is independent of wavelength, equation 2.5 can be rewritten as

$$\left(1 - \frac{\exp\left(\frac{C_2}{\lambda_1 T} \right) - 1}{\exp\left(\frac{C_2}{\lambda_1 T_{app,1}} \right) - 1} \right)^{\lambda_1^\alpha} = \left(1 - \frac{\exp\left(\frac{C_2}{\lambda_2 T} \right) - 1}{\exp\left(\frac{C_2}{\lambda_2 T_{app,2}} \right) - 1} \right)^{\lambda_2^\alpha} \tag{2.6}$$

From the measured radiation intensities, it is possible to determine $T_{app,1}$ and $T_{app,2}$ using Planck's Law (equation 2.3), after which the actual soot cloud temperature, T, can be determined from an iterative solution of equation 2.6. The solution to equation 2.6 must satisfy the condition that $T > T_{app,1,2}$, as $\varepsilon \leq 1$. Once T has been determined, equation 2.5 is used to determine the KL factor.

The KL factor is the *optical thickness* of the gas cloud and is based on the assumption of a mixture with a uniform temperature and composition according to the definition

$$\kappa = \int_0^L KS\,ds \tag{2.7}$$

---

[1]Because of the empirical nature of this correlation, it should be noted that the wavelength is considered in units of μm.

where κ is the measure of the light attenuation for a given medium over a given path length. The extinction coefficient K is a physical property of the mixture and is a function of the mixture temperature, pressure, and composition. The extinction coefficient is the sum of the absorption coefficient[2] a and the scattering coefficient σ:

$$K = a + \sigma \tag{2.8}$$

If scattering is assumed to be small compared to absorption, the absorption coefficient is given by

$$a \propto \frac{1}{\lambda} \tag{2.9}$$

For Rayleigh scattering ($\lambda \ll D_p$), scattering cross section is of the form

$$\sigma_s \propto \frac{1}{\lambda^4} \tag{2.10}$$

Thus, for all λ absorption is the dominant mechanism for radiation attenuation and scattering can be neglected. In general KL is on the order of 1, implying that an optically thick medium is being considered and that the measured light intensity is that of the soot cloud surface. The temperature and concentration of the soot within the cloud is not well represented.

Pyrometry, however, is not without its limitations. Because pyrometry determines the soot cloud temperature and KL factor based on the recorded radiation intensity, it is limited to only the "hot" soot within its field of view. As radiation intensity is defined by the Stefan Boltzmann Law

$$i_b = \sigma T^4 \tag{2.11}$$

where σ is the Stefan Boltzmann constant, and the temperature influence is to the fourth power, particles at low temperatures will not have a sufficient radiation intensity to provide an adequate signal to noise ratio. If the soot cloud is outside of the field of view of the sensor, its radiation intensity cannot be recorded by the pyrometer, and hence will not contribute to the spatially averaged temperature and KL factor. Inhomogeneous temperature distributions within the combustion chamber, caused by an inhomogeneous distribution of the hot soot, will result in a higher temperature being measured than arithmetic mean temperature in the combustion chamber [110]. This is due to the exponential nature of the radiation intensity with increasing temperature (i.e.

---

[2] Recall that under Kirchoff's Law, the emissivity and absorptivity are equal, $\epsilon = a$.

the hotter regions are weighted more heavily). In addition to the radiation from the hot soot clouds, radiation reflected from the cylinder walls can also be recorded by the pyrometer. When the radiation in the visible spectrum is considered, the wall reflections result in temperature errors on the order of 1-2 K, and KL factor errors on the order of 10% for low soot concentrations (worst case scenario). If wavelengths in the infrared spectrum are considered, the errors in temperature and KL factor increase to 50 to 150 K and 50%, respectively [72], due to the enhanced reflection of the cylinder walls in this wavelength regime.

Contamination of the pyrometer window itself through the deposition of soot, can result in further errors in the measurements. In [72], a 14% reduction in transmission resulted in a 1% error in the temperature measurement and a 5% error in the KL factor ($\lambda = 0.55\mu$m). Due to the fact that temperature is determined based on the ratio of the two recorded light intensities (see equation 2.6) the temperature measurement is less influenced by window contamination than the KL factor, where the absolute radiation intensity is relevant (equation 2.5) [112]. A comprehensive discussion of the two color method for soot temperature and concentration determination can be found in [111].

Through the consideration of the in-cylinder soot temperature and concentration, the influence of engine parameters on particle formation and oxidation to be investigated directly, rather than inferred from exhaust stream measurements. It has been shown that the final KL-factor value after the formation and oxidation processes are completed correlates well with the measured exhaust stream particle concentration [58], [47].

Multi-color pyrometry can be used to characterize the soot formation and oxidation processes. As an approximation, the maximum of the KL-Factor history during combustion can be used to represent the soot formation (though soot oxidation is already taking place), while the difference between the KL-factor maximum and its end value can be used to characterize the oxidized soot fraction, as shown in figure 2.4.

2.4   Particle Emissions from Diesel Engines

While the processes outlined in section 2.2 are responsible for soot formation, the diesel engine presents a difficult environment to understand soot emissions due to the turbulent diffusion flame by which the fuel is converted. In addition to the heterogeneous nature of the diesel spray, the numerous global engine
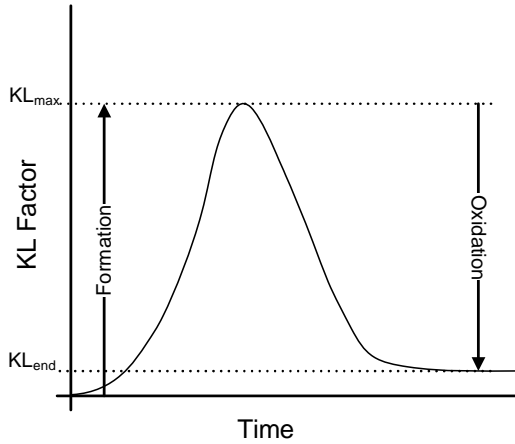
Figure 2.4: Representative KL-Factor history, indicating particle formation and oxidation phases, as well cylinder out emissions (KL_{end}).
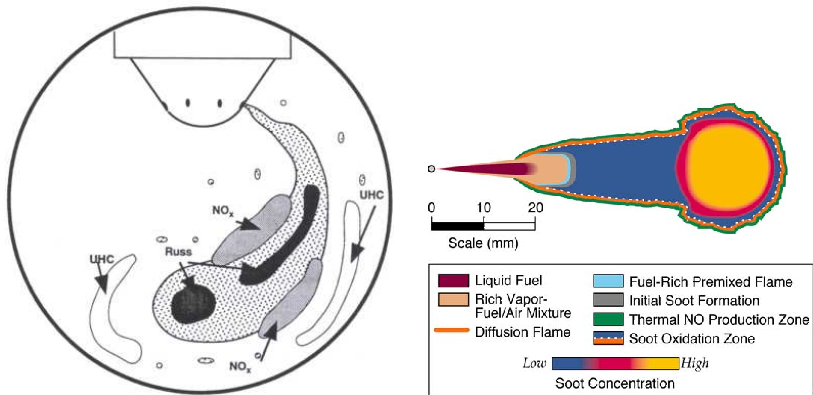
Figure 2.5: Conceptual models of diesel spray and associated emissions formation regions from [57] (left) and [24] (right).

operating parameters influencing particle emissions must be considered.
Figure 2.5 shows a representative diesel spray (only one spray of a multi-hole injector is shown for clarity) and elucidates the various emission formation zones. As discussed above, soot is formed under fuel rich conditions and high

temperatures, which is seen in the core of the spray. As the spray dissipates and the combustion is completed, the particles diffuse away from the flame and are carried into the outer, oxygen-containing regions of the combustion chamber where they can undergo oxidation. NOx is formed on the boundary of the spray diffusion flame where the temperatures and oxygen concentrations are sufficiently high.

2.4.1   Influence of Engine Operating Parameters

The strong dependence of the particle emissions on the local air-fuel ratio and temperature can be described by considering the $\phi - T$ map [3], shown in figure 2.6. For a given local equivalence ratio and temperature, such a map provides an estimate of the (normalized) generated soot quantity. Figure 2.6 indicates that the soot formation is at a maximum for temperatures of approximately 1900 K. At temperatures above and below this value the generated soot quantity decreases, as at lower temperatures particle inception reactions are too slow. The soot precursors are present, but the reactions do not take place. At higher temperatures, the oxidation rates are sufficiently high that the formed PAH are oxidized before they can undergo growth and subsequent particle inception.

Figure 2.6 was generated by carrying out a series of 0-D simulations of the detailed soot formation and oxidation chemistry for n-hexane at 6 MPa with 0% EGR at different temperatures and equivalence ratios. Figure 2.6 is the resulting soot yield after 1.0 ms calculation time in a constant volume control system. Thus, it should be noted, that while figure 2.6 is a powerful tool for the understanding of the soot kinetics with particular regard to the influences of temperature and equivalence ratio, it does not consider the influences of combustion, heat transfer, inhomogeneities in the combustion chamber, or the soot chemistry of an actual diesel fuel.

In addition, figure 2.6 shows the NO formation region, which is also a function of the local temperature and oxygen availability. There is, in general, a conflict between soot and NO_x emissions, in that a reduction in one usually results in the increase of the other and is commonly referred to as the soot-NOx tradeoff. The ideal combustion process would pass through the valley between the formation regions, which in practice is very difficult to do due to the highly heterogeneous nature of diesel combustion.

Though the engine out soot emissions are the result of localized phenomena within the combustion chamber and the spray itself, the global engine operat-

Figure 2.6: $\Phi - T$ map for soot and NO formation under diesel like conditions [3].

ing parameters do have a strong influence on the engine out soot emissions. In order to better understand these effects, the influences of the injection pressure, the injection timing, air-fuel ratio and EGR rate are discussed in detail below, based on measurements from two heavy duty research engines.
Using in-cylinder pyrometry results from [89] and exhaust stream size distribution measurements from [12] the influences of the injection pressure, injection timing, exhaust gas recirculation, engine load (air-fuel ratio) are presented. Additionally, the influences of fuel structure on the soot emissions will be discussed.

Injection Pressure

The injection pressure influences the particle emissions by changing the in-cylinder turbulence and diesel spray characteristics. If the particle mass and size distributions are considered, as shown in figure 2.7, a decrease in particle

Figure 2.7: Influence of the injection pressure on the particle size distribution (left, [12]) and in-cylinder soot concentration history (right, [89])

mass, number, and size are seen for an increase in the injection pressure, due primarily to enhanced oxidation. Figure 2.7 also shows the KL-Factor histories for the several different injection pressures. For the higher injection pressures, more soot is formed (characterized by the higher maximum KL-factor values) due to faster diffusion combustion rates. The final KL-factor values and exhaust stream measurements, however, decrease with increasing injection pressure. The enhanced oxidation brought on by increasing the injection pressure can be attributed to the increased turbulence and thus better transport of the particles to the remaining oxygen for particle oxidation. Additionally, because the combustion process is faster at higher injection pressures, more time remains available for the soot oxidation after combustion is completed.

Injection Timing

By varying the timing of the beginning of fuel injection, the particle emissions are influenced primarily through changes in the in-cylinder temperatures which impact the premixed combustion fraction as well as the oxidation process. Figure 2.8 indicates that an advancement of the injection timing results in a decrease in the number of particles in the exhaust stream, while the size distribution remains largely unchanged. When the KL-Factor histories shown in right hand side of figure 2.8 are considered, it can be seen that for retarded injection timings, particle formation increases while oxidation decreases. The increase in the particle formation can be attributed to the reduced premixed fraction for later injection, caused by the higher gas temperatures and hence reduced ignition delays. Furthermore, retarded injection timings lead to lower peak temperatures, which, coupled with the exponential dependence of oxi-
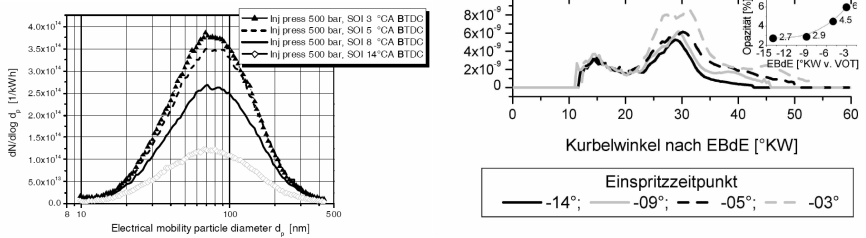
Figure 2.8: Influence of the injection timing on the particle size distribution (left, [12]) and in-cylinder soot concentration history (right, [89])
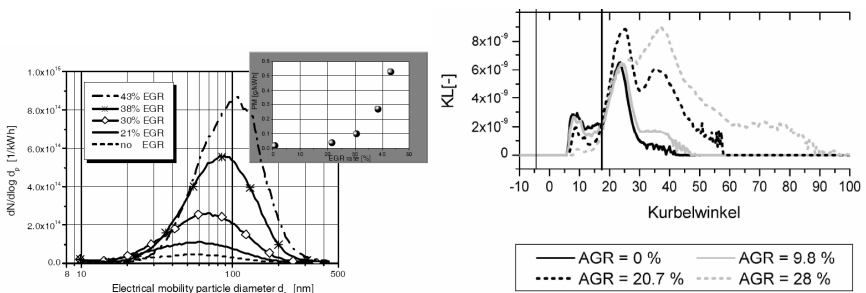
Figure 2.9: Influence of the EGR rate on the particle size distribution (left, [12]) and in-cylinder soot concentration history (right, [89])

dation on the temperature, results in decreased oxidation rates. While late injection timings do result in higher exhaust gas temperatures, the dominant effect is nonetheless the decreased maximum temperature.

Exhaust Gas Recirculation

Recirculating exhaust gases into the cylinder increases the particulate emissions through decreased oxygen availability and lower in-cylinder temperatures (which also results in decreased NOx emissions). The increase in the particle number and mass emissions with increasing EGR rates described above is evident in figure 2.9, as is an increase in the mode particle diameter. As the particle concentration increases by increasing the EGR rate, the likelihood of particles colliding also increases, resulting in enhanced coagulation and agglomeration rates. Furthermore, the recirculated particles act as nuclei for
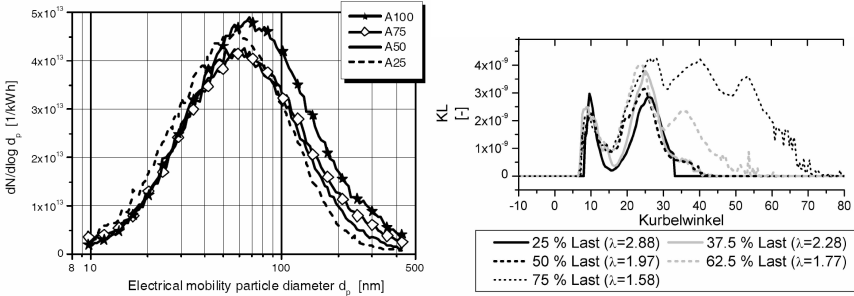
Figure 2.10: Influence of the relative air-fuel ratio on the particle size distribution (left, [12]) and in-cylinder soot concentration history (right, [89])

further growth in the subsequent combustion cycles.

The time resolved KL-Factor histories shown in right hand side of figure 2.9 indicate that the increasing EGR rate initially slows the particle formation mechanism, due to lower combustion temperatures. As combustion progresses and finally ends, however, the oxygen deficiency results in higher particle concentrations. Finally, the lower oxygen concentration and lower exhaust temperatures result in slower particle oxidation rates, as characterized by the decreasing gradients to the right of the KL-Factor maximum.

Load and Air-Fuel Ratio

The load in a diesel engine is controlled by varying the air-fuel ratio, which also influences the particle emissions. As the fuel load is increased, the relative oxygen concentration decreases and results in increased particle emissions. From figure 2.10 it can be seen that the increase in particle mass is largely due to an increase in the number of larger particles ($d_p > 50$ nm). In general, it is assumed that the increased particle emissions are due to the low oxygen concentration inhibiting particle oxidation, as well as the higher temperatures and higher fuel quantities resulting in shorter ignition delays and higher diffusion combustion fractions. These trends can also be seen in figure 2.10, as the maximum KL factor values increase and the oxidation rates decrease with increasing load (increasing fuel quantity and decreasing oxygen concentration). It should be noted that there is a critical air-fuel ratio above which changes in the air-fuel ratio have a relatively small influence on the particle emissions. If the air-fuel ratio falls below this critical value, the particle emissions begin to increase dra-

matically. The critical global air-fuel ratio decreases with increasing injection pressure, as the increased fuel injection generated turbulence enhances the in-cylinder mixing, thus promoting oxidation. The influence of improved mixing allowing lower air-fuel ratios to be used was also noted by [93].

Fuel Composition

In the preceding discussion the influences of engine operating parameters on the soot emissions are discussed, though it should be noted that the fuel itself also plays a strong role. In particular, the sulfur and aromatic content of the fuel have a considerable influence on the particle emissions.

Sulfur has only a small influence on the soot emissions, but plays a strong role in the particulate mass emissions[3]. An increase in the fuel sulfur content results in increased number of sulfate and sulfuric acid particles, caused by the condensation and nucleation of the sulfates when the exhaust gas cools [49]. Additionally, the sulfates can condense onto the already formed soot particles, thereby increasing their size and mass if they are measured gravimetrically.

Aromatic compounds within the fuel directly influence the soot emissions as they provide the precursors needed for soot particle inception. As mentioned in 2.2.1, the soot formation rate is limited by the rate at which the first PAHs are formed. If aromatic compounds are already present in the fuel, this step is not needed, and the soot formation is accelerated considerably.

2.4.2 Particle Emissions During Transient Operation

From the measurement of vehicle soot emissions during driving cycles such as the New European Driving Cycle (NEDC), it has been seen that the soot emitted during transient operation has a substantial influence on the total emission over the entire cycle. To gain a detailed understanding of the soot emissions during transient engine operation, soot instrumentation capable of measuring the soot emissions with a high temporal resolution is necessary. Commercially available instruments capable of transient exhaust stream measurements are based on the differential mobility spectrometer [82], cascade impactor principle [45] [61], and photo-acoustic soot sensor (PASS) [87] principles. The latter provides only the mass concentration of the soot, while the former three can also be used to obtain particle size information.

---

[3]Recall that the term soot refers to only particles composed of elementary carbon, while particulate matter refers to all particles, regardless of their composition.

In [36], a Dekati Mass Monitor (cascade impactor operating principle) was used to measure the soot mass during tip-in transients[4] of different durations. The change in the soot emissions due to the transient operation was characterized using a Quasi Steady State (QSS) approximation, with which the corresponding steady state soot emissions are estimated based on the measured engine speed and load during the transient. In general, faster transients resulted in short term spikes in the NO_x and soot emissions. The increase in NO_x emissions was attributed to an instantaneous increase in the fuelling rate, coupled with a slower increase in air quantity resulting in higher in-cylinder temperatures, thereby accelerating the NO_x formation. Similarly, the soot emissions are increased due to an oxygen deficit caused by the turbo-lag and slow closing of the EGR valve (though only a slow NDIR analyzer was used for the EGR rate determination). The influence of the slow EGR valve closing was also noted in [107] where a considerable decrease in the transient soot emissions was noted when the EGR valve was maintained in a closed position throughout the duration of the transient. In [36] it was also noted that as the injection pressure is rapidly increased while the charge pressure is only slowly increased, thus resulting in a deeper spray penetration and increased wall impingement, leading to increased particle emissions..

[108] used a two-color pyrometer to measure the in-cylinder soot concentration in a diesel engine operating under transient conditions. By using a representative "soot concentration weighting function" it was possible to characterize the cycle-specific soot emissions during tip-in transients. Again an increase in the soot emissions was seen and attributed to the slow response of the turbocharger and EGR valve. Furthermore, it was found that the increase in the soot emissions was fundamentally caused by a reduction in the oxidation, characterized by a strong light signal after the end of injection.

2.5   Soot Modelling

While the preceding discussion has focussed on the general mechanisms of soot formation and oxidation in diesel engines, as well as the effects of the engine operating parameters on the engine out soot emissions, there exist several methods by which the soot emissions can be modelled. Although the fundamental chemical and physical processes governing the formation and oxidation of soot are not completely understood, researchers have nonetheless success-

---

[4]A tip-in transient refers to a load increased at a constant engine speed and is further discussed in 4.2.1

fully coupled single and multi-zone, as well as CFD simulations with detailed soot formation and oxidation models. Due to the computational requirements of these approaches, however, there is considerable interest in phenomenological models which only consider the most relevant processes and still allow the prediction of the soot emissions with significantly lower computational costs, albeit it with a lesser fidelity. If the ultimate in calculation speed is required, there is also the option of using empirical soot models, which are limited largely to an engine and fuel combination operating in the regime for which they were calibrated. In the following discussion, several examples of phenomenological and empirical soot models are presented. As detailed models are not within the scope of this work, they will not be discussed, though interested readers are referred to [54], [40], or [96].

2.5.1 Phenomenological Models

The Hiroyasu Model and its Derivatives

Potentially the most popular phenomenological soot model is that proposed by [39], which describes the net rate of change of the soot mass as the difference between the soot formation and oxidation processes:

$$\frac{dm_s}{dt} = \frac{dm_{s,form}}{dt} - \frac{dm_{s,ox}}{dt} \tag{2.12}$$

where the soot oxidation rates were defined as:

$$\frac{dm_{s,form}}{dt} = A_f \cdot m_{f,v} \cdot p^{0.5} \cdot \exp\left(\frac{-E_{a,form}}{RT}\right) \tag{2.13}$$

$$\frac{dm_{s,ox}}{dt} = A_{ox} \cdot m_s \frac{p_{O_2}}{p} \cdot p^{1.8} \exp\left(\frac{-E_{a,ox}}{RT}\right) \tag{2.14}$$

A_f and A_{ox} are scaling factors determined based on comparison with measured soot emissions, $m_{f,v}$ is the fuel vapor mass, p is the pressure, $E_{a,form}$ and $E_{a,ox}$ are the activation energies of the formation and oxidation processes, respectively, and m_s is the soot mass. The empirical nature of equations 2.13 and 2.14 should be noted, as is evident by their dimensional inhomogeneity.

The soot formation is considered through a first order reaction of the fuel vapor, while the soot oxidation represents a second order reaction between the generated soot and oxygen available. [39] implemented this model in a multizone combustion model, where local temperature and oxygen concentrations were considered, though this model has also been implemented in zero

dimensional investigations. For both formation and oxidation processes, the temperature dependencies are described using an Arrhenius function.

[77] implemented the Hiroyasu model in a 3D-CFD simulation to determine the spatially and temporally resolved in-cylinder soot distribution, though the oxidation process was described using that presented by [74], in which two types of active sites are considered for oxidation on the surface of the particle. In particular, "more" reactive and "less" reactive sites are considered, as is the shift from more to less reactive sites in order to reproduce the effects of particle aging. In their investigation, [77] noted that the soot model was likely hindered by limitations in the combustion, spray and turbulence models not providing accurate state information to the soot model.

In a subsequent work from the same group, [22] improved the spray model and additionally considered the influence of the soot radiation on the fuel evaporation. More importantly however, the soot oxidation submodel of [68] was used, which considers the effects of turbulent mixing and the competition of unburned fuel and soot for the oxygen:

$$R_{s,ox} = A \left(\frac{c_{O_2}}{r_s} \right) \left(\frac{\epsilon}{k} \right) \left(\frac{c_s r_s}{c_s r_s + c_f r_f} \right) \tag{2.15}$$

where c_s, c_f, r_s, and r_f are the concentrations and stoichiometric oxygen ratios for soot and fuel oxidation, respectively. This representation of the soot oxidation, coupled with the introduction of a soot oxidation cut-off temperature of 1800K [64] enabled [22] to reproduce the effects of EGR and multiple injection events.

In [88], the base Hiroyasu model [39] was coupled with a two-zone thermodynamic model and further refined to represent the formation and oxidation rates in a dimensionally homogeneous fashion, as well as to consider the influences of turbulence. In particular the following was suggested:

$$\frac{dm_{s,form}}{dt} = A_f \cdot \frac{dm_{f,v}}{dt}\bigg|_{diff} \cdot \left(\frac{p_{cyl}}{p_{ref}} \right)^{n_1} \cdot \exp \left(\frac{T_{a,form}}{T_{mean}} \right) \tag{2.16}$$

$$\frac{dm_{s,ox}}{dt} = A_{ox} \cdot m_s^{n_2} \cdot \frac{1}{\tau_{char}} \left(\frac{p_{O_2}}{p_{O_2,ref}} \right)^{n_3} \cdot \exp \left(\frac{T_{a,ox}}{T_{mean}} \right) \tag{2.17}$$

where $\frac{dm_{s,form}}{dt}$ is the fuel conversion rate during mixing controlled (diffusion) combustion and τ_{char} is the inverse of a characteristic mixing timescale (see section 4.6.1 and is influenced primarily by turbulence generated by fuel injection and piston motion. The model scaling factors (A_f and A_{ox}), exponents (n_1 - n_3), and activation temperatures ($T_{a,form}$ and $T_{a,ox}$) were determined

through comparison of the calculated and measured in-cylinder soot histories obtained using multi-color pyrometry for 10 operating points. After the determination of the model parameters, it was possible to reproduce the qualitative and in part quantitative soot emissions of 70 different operating points.

A subsequent extension of this model was carried out in [102] and [103], where the dominant modifications were to consider the chemical kinetics of the soot formation using a $\Phi - T$ soot map [3] (see Figure 2.6) rather than an Arrhenius function and to consider the process-relevant global temperatures (while still in the framework of a two-zone thermodynamic model). The resulting soot formation rate is given by:

$$\frac{dm_{s,form}}{dt} = A_f \cdot \left. \frac{dm_{f,v}}{dt} \right|_{diff} \cdot \left(\frac{p_{cyl}}{p_{ref}} \right)^{n_1} \cdot f_s \left(T_{form}, \Phi_{form} \right) \qquad (2.18)$$

where f_s approximates the soot formation map [3] according to:

$$f_s \left(T_{form}, \lambda_{form} \right) = \left(\frac{0.75 - \lambda_{form}}{0.65} \right)^{1.5} \cdot \exp \left(- \frac{\left(T_{form} - \mu_{0,form} \right)^2}{2 \cdot \sigma_0^2} \right)$$
$$(2.19)$$

$$\mu_0 = 2160 - 400 \cdot \lambda_{form} \qquad (2.20)$$

$$\sigma_0 = 210 - 100 \cdot \lambda_{form} \qquad (2.21)$$

Rather than using the mean gas temperature within the combustion chamber, a temperature representative of the formation and oxidation processes was used. The formation temperature was determined using a two-zone thermodynamic model assuming that the mixing controlled combustion takes place at a relative air-fuel ratio of unity. The oxidation was assumed to take place at the bulk gas temperature assuming $\lambda > 1$. In a later work, [104] used a two-zone model to determine the respective temperature histories using arbitrarily defined λ values. It was found that for formation, $\lambda \approx 0.6$ provided good estimates of the soot emissions. Interestingly, this corresponds with pyrometry investigations where similar λ values were required to match the calculated burned gas temperature with the measured (via pyrometry) temperature [88], [52].

[53] also considered the temperature of a rich zone for the soot formation and a representative bulk gas temperature for the oxidation. Additionally, it was also considered that the soot is formed only in the rich fraction of the flame f, which was estimated using:

$$f = c_f \frac{m_{f,v}}{u_{turb} N_{nozz}} \qquad 0 \leq f \leq 1 \qquad (2.22)$$

where u_{turb} is the turbulence intensity and N_{nozz} is the number of holes on the injector. As the turbulence intensity increases, through an increase in the injection pressure, the rich flame fraction decreases resulting in lower soot emissions. [53] consider this in the soot formation using:

$$\frac{dm_{s,f}}{dt} = A_f \frac{dm_f}{dt} f \exp\left(\frac{T_{a,s,f}}{T_f\,(\lambda = 0.6)}\right) \qquad (2.23)$$

To consider the effect of unburned mixture being transported in the burned gas zone, a g function was used:

$$g = c_1 \rho_{ub} u_{turb} V_b^{2/3} N_{nozz} + c_2 \frac{dm_f}{dt} 6n \qquad (2.24)$$

where ρ_{ub} is the density of the unburned mixture and V_b is the volume of the burned mixture zone. Using the g function the oxygen fraction, $x_{O_2,b}$ in the burned mixture zone was determined and used to determine the soot oxidation rate:

$$\frac{dm_{s,ox}}{dt} = A_{ox} m_s^{n_{ms}} \left(m_b x_{O_2,b}\right)^{n_{O_2}} \exp\left(\frac{T_{a,ox}}{T_b}\right) \qquad (2.25)$$

The influence of air entrainment into the soot formation zone was also considered by [8]. There, it was reasoned that the lift off length of the flame can be shown to have an influence on the soot formation, as the longer the lift-off-length, the more air will be entrained into the spray, and the leaner (or less rich) the soot formation zone will be. This effect was quantified using a measure of the equivalence ratio at the point of initial reaction:

$$\phi = \frac{100}{\frac{10}{3}\left(\sqrt{1 + \left(\frac{LOL}{x^+}\right)^2} - 1\right)} \qquad (2.26)$$

where LOL is the lift off length (see [91], for example) and x^+ is the length scale. In general, the determination of the lift-off-length requires detailed knowledge of the injector geometry and the time resolved injection rates and cylinder pressure histories. ϕ is considered in the standard Hiroyasu soot formation rate using:

$$\frac{dm_{s,form}}{dt} = A_f \cdot \phi m_{f,v} \cdot p^{0.5} \cdot \exp\left(\frac{-E_{a,form}}{RT}\right) \qquad (2.27)$$

The soot oxidation rate remained unchanged from the the original Hiroyasu formulation, with the exception that oxidation temperature is assumed to be

that after a stoichiometric combustion of the diesel. The oxidation is assumed
to stop after the mean bulk gas temperature falls below 1000K.

Several formulations of the Hiroyasu model have been presented, each with
attempts at improving its performance. In general, this has included the con-
sideration of the following parameters:

- The effects of turbulence caused primarily through changes in the injec-
  tion process. To this end, representative mixing time scales ([88], [103]),
  the spray lift-off length [8], or mixing functions have been implemented
  [53].

- Representative formation and oxidation temperatures. In general, soot
  formation is assumed to take place in the rich region of the flame and as
  such the temperature has been calculated by two zone models consider-
  ing a relative air fuel ratio equal to or less than unity. The soot oxidation
  is assumed to take place either in the immediate vicinity of the flame
  [8] resulting in the stoichiometric temperature being considered, or else
  in the bulk mixture, which includes consideration of the burned or mean
  gas temperatures.

- The simplified second order description of the soot oxidation can be
  replaced by that of [74].

- Though only done by one group [102], the Arrhenius dependance of the
  formation can also be replaced by a $\phi - T$ map to include chemical kinetic
  considerations in the formation rate.

All of the discussed implementations of the Hiroyasu model require at least
the cylinder pressure history as an input, while several also require histories of
the heat release rate, injection velocity or mass, and formation and oxidation
temperatures (regardless of their definition). The Hiroyasu model has been
coupled with multizone and CFD simulations but also with zero-dimensional
calculations, though in both cases several researchers have commented on
the sensitivity of the various soot models on the mixture state description.
All versions of the soot model must be parameterized against measured soot
emissions. Finally, it should also be explicitly noted that the Hiroyasu model
only provides the soot mass and no information with regard to the particle
sizes, numbers, or composition. While these parameters are not within the
scope of this work, they will gain importance in the near future, as legislation
will start to consider also the number of particles emitted.

Multi-Step Models

A more detailed description of the soot formation and oxidation is possible using multi-step models, though this comes at a much higher computational cost. The goal of such models is to phenomenologically describe the relevant soot formation and oxidation processes of: fuel pyrolysis, precursor and PAH formation, particle inception, surface growth, coagulation, and oxidation of the particles, precursors, and growth species.

Of the multi-step phenomenological models, the most popular are those based on the works of [33] and [10]. In [33] 8 step steps are considered

1. Pyrolysis of fuel to soot precursor radicals

2. Pyrolysis of fuel to growth species, most notably acetylene

3. Particle inception from the soot precursors (nucleation)

4. Particle surface growth

5. Coagulation of the soot particles

6. Oxidation of the soot precursor radicals

7. Oxidation of the growth species

8. Oxidation of the soot particles

[44] slightly modified the coagulation and surface growth submodels and were able to reproduce the overall trends of soot emissions, especially the soot volume fraction, f_v. Difficulty was seen when trying to compare in-cylinder measurements of the size and particle number, primarily due to the heterogeneous nature of measurements. This model was further developed by [97] where fuel was considered to pyrolyse to acetylene and then to form soot precursors, take part in surface growth, or be oxidized. This step was introduced to remove any competition between the formation of precursor and acetylene formation. In [10], the pyrolysis of the fuel to form acetylene is also considered separately followed by consumption of the acetylene through either particle growth, nucleation, or oxidation. Finally, carbon oxidation and particle agglomeration are also considered.

Rather than considering 8 steps, [62] consider only four: nucleation, surface growth, particle coagulation and particle oxidation, which were defined as follows:

$$C_2H_2 \rightarrow 2C_{(s)} + H_2 \qquad \text{Nucleation} \qquad (2.28)$$

$$C_2H_2 + nC_{(s)} \rightarrow (n+2)C_{(s)} + H_2 \qquad \text{Surface Growth} \qquad (2.29)$$

$$C_{(s)} + \frac{1}{2}O_2 \rightarrow CO \qquad \text{Oxidation} \qquad (2.30)$$

$$nC_{(s)} \rightarrow C_{n(s)} \qquad \text{Agglomeration} \qquad (2.31)$$
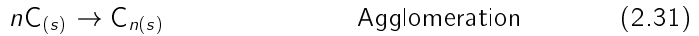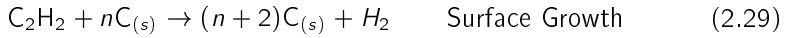
The rate of the nucleation reaction is assumed to be purely Arrhenius, while for the surface growth it is necessary to consider the influence of surface aging through the square root of the total particle surface area, $A_{p,t}$:

$$R_2 = k_2\left(T\right)[C_2H_2]\sqrt{A_{p,t}} \qquad (2.32)$$

The oxidation rate considers the local (particle individual) surface area so that its influence on the particle size can also be determined:

$$R_3 = k_3\left(T\right)A_p\left[O_2\right] \qquad (2.33)$$

The agglomeration rate follows the conventional particle number squared dependency.
[64] developed a phenomenological soot model for implementation in a multizone model. In particular, four zones are considered for the soot model: 1) A zone in which the air/fuel ratio is above the lean flammability limit; 2) a zone which contains a combustible mixture of fuel and air; 3) a zone in which the air/fuel ratio is below the rich flammability limit; and 4) a zone in which the combustion rate is defined by the mixing processes. Zone 4 is considered to be that which is relevant for the soot and soot precursor formation, as is zone 2, given that there is an oxygen deficit. The soot formation itself is described based on [63] in which a global reaction is used to describe the formation of solid carbon from the gas phase fuel and air mixture. It is assumed that the formed soot is composed of spherules with a diameter of approximately 30 nm. The number density of the particles, is determined considering the coagulation and surface oxidation. The latter is described using the [74] model including consideration of oxidants other than oxygen, such as OH.

2.5.2 Empirical Methods

For the ultimate in simplicity and minimal calculation times, it is possible to estimate the soot emissions based solely on empirical relationships gained from

measurements. In [106] a multiplicative relationship is used to describe the
soot emissions:

$$FSN = K_1 \cdot \tau_{ign}^{e_1} \cdot \alpha_1^{e_2} \cdot \left(\frac{dp}{dt} \right)_{max}^{e_3} \cdot \alpha_2^{e_4} \cdot [O_2]^{e_5} \cdot \left(\frac{m_{air}}{m_{tot}} \right)^{e_6} \qquad (2.34)$$

where K_1 is a scaling factor, e_1 through e_6 are engine dependent exponents,
τ_{ign} is the ignition delay, and α_1 and α_2 are effective positive and negative
slopes of the heat release rate, respectively. After using 400 data points to
determine the 7 model parameters (scaling factor and exponents) the model
was able to reproduce the soot emissions with a correlation coefficient of
$R^2 = 0.85$. When the model is validated against 28 operating points which
were not considered during the model parameterization, but are still within
the parameterization operating regime, the model is capable of reproducing
the soot emissions for almost all operating points. It should be noted, that
for each of the operating points, the heat release rate and cylinder pressure
history are required either from measurements or detailed simulations.

As a combination of empirical and phenomenological modelling, [16] use a
neural network to parameterize the variation of the Hiroyasu model [39] pre-
sented by [8] by introducing a total of 23 model weights, w_i which required
determination. The system describing the soot formation, oxidation, and net
soot mass is given by the following:

$$x = C_{s,form} \left(w_3 \phi + w_4 \right)^{w_{19}} \cdot m_f^{w_{20}} \cdot p^{0.5 w_5} \cdot \exp \left(\frac{-E_{a,form}}{RT_f} w_6 + w_7 \right) \quad (2.35)$$

$$y = C_{s,ox} \left(w_{10} m_s + w_{11} m_s^2 \right)^{w_{22}} \cdot Y_{O_2} \cdot p^{1.8 w_{14}} \exp \left(\frac{-E_{a,ox}}{RT_{ox}} w_{15} + w_{16} \right) \tag{2.36}$$

$$\frac{dm_s}{dt} = w_{17} \left[\left(\left(w_1 x + w_2 x^2 \right)^{w_{21}} \right) - \left(\left(w_8 y + w_9 y^2 \right)^{w_{23}} \right) \right] + w_{18} \qquad (2.37)$$

where the equivalence ratio at ignition, ϕ, was introduced in equation 2.26.
After training the model, it was capable of predicting the soot emissions better
than either the "raw" soot model without the 23 weighting factors, or than
a standard neural network. This is attributed to the fact that the underlying
phenomenological model is better capable of describing the actual processes
of soot formation and oxidation than an arbitrary mathematical function. Fur-
thermore, the additional weighting parameters effectively correct any deficien-
cies of the phenomenological model. It should, however, be explicitly noted
that the cylinder pressure and available fuel mass are required as model inputs.

2.6 Summary

This chapter reviewed the current understanding of soot formation and oxidation with a particular focus on the influence of steady state and transient diesel engine operating parameters and their characterization. Soot particles emitted from a diesel engine are the result of the competition between formation and oxidation processes. The formation consists of the formation of the PAHs, their growth through the HACA mechanism, nucleation of the large PAHs into solid particles, followed by a continued surface growth of the particles by HACA, as well as coagulation and agglomeration. At all points during the formation process, oxidation through various species can take place, given that the temperature is sufficiently high. Thus the soot emissions from diesel engines are influenced by the available oxygen (defined by λ and EGR), the in-cylinder temperatures, and the in-cylinder turbulence which is dependant on the injection pressure. During transient engine operation, the increased particle emissions are predominantly attributed to an oxygen deficit, though there are only limited investigations of global engine parameters in this area.

Many different methodologies are available for the characterization of diesel exhaust stream particle emissions, though most commonly the particle mass, size and number are used. Through the use of multi-color pyrometry, the temporally resolved in-cylinder particle temperature and concentration can be determined and used to investigate the influence of engine operating parameters on the formation and oxidation processes directly, rather than inferring them from exhaust stream measurements. Models of the soot emissions from diesel engines can range from detailed kinetic mechanisms coupled with computational fluid dynamics solvers, to zero-dimensional phenomenological models, to empirical correlations. Naturally, as the complexity of the model is decreased, so too is the calculation time - at the cost of reduced extrapolative performance. The most commonly used phenomenological model is that presented by Hiroyasu [39], though it has been modified by many researchers. A phenomenological model can provide a satisfactory tradeoff between calculation time, performance, and extrapolative capability, though the effects of engine operation, including combustion, must be considered. Of the known models, none are capable of achieving all of the requirements of this investigation, namely: 1) calculation times *less than 20 ms*; 2) use only information available from standard ECUs and *not* consider any cylinder pressure based information); 3) be capable of calculating soot emissions *outside* of its parameterized region; and 4) have a demonstrated capability to reproduce the soot emissions during *steady-state and transient* operation.

Chapter 3

Development of a Mean Value Soot Model

3.1   Introduction

A mean value soot model (MVSM) capable of predicting the engine out soot emissions from a common rail diesel engine is to be developed. Such a model is intended to be used as a soot emissions predictor for control purposes, as well as to provide an estimate to the soot loading of a diesel particle filter. Based on these intended implementations, the developed MVSM must:

- be capable of realtime calculation of the cycle specific soot emissions. For an engine speed of 6000 rpm this corresponds to a calculation time of 20 ms.

- use only readily available engine parameters as model inputs. This includes parameters taken from the engine control unit or other realtime models, but excludes the use of cylinder pressure measurements and heat release histories, as they are not typically available in production engines.

- be capable of predicting the soot emissions during steady state and transient engine operation.

- be able to predict soot emissions outside of its calibrated operating regime (extrapolative ability). This constraint limits the model choice to phenomenologically based models, as these are believed to provide a better description of the underlying physical, chemical, and thermodynamic processes.

33

An existing, crank-angle-resolved soot model ([88], [102]) was selected as the basis for the new mean value soot model, as its feasibility for a wide range of engine sizes, types and fuels has already been demonstrated [103]. This model, however, requires that the in-cylinder pressure history, heat release rate, injection rate, and in-cylinder temperatures (in both the soot formation and oxidation zones) are known. Given that these histories are available from either measurements or simulations, the calculation times are approximately 1 s. To reduce the calculation times, the aforementioned histories were replaced with estimated, representative (scalar) values describing the relevant mixture states, thus considering the mean processes rather than the time-resolved processes requiring expensive numerical integration. In this chapter, the development of the MVSM is presented by first introducing the relevant mixture states considered by the MVSM, followed by a schematic overview of the model layout and finally a detailed description of each of the model terms. Subsequently the parameterization of the MVSM is discussed.

3.2   Overview of Existing CAD Resolved Soot Model

In the crank-angle resolved soot model [103], the engine-out soot emissions are described as the competition between the in-cylinder soot formation and oxidation processes:

$$\frac{dm_s}{dt} = \left.\frac{dm_s}{dt}\right|_{form} - \left.\frac{dm_s}{dt}\right|_{ox} \tag{2.12}$$

Where the soot formation rate is described as

$$\left.\frac{dm_s}{dt}\right|_{form} = A_{form}\left.\frac{dm_f}{dt}\right|_{diff}\left[\left(\frac{p_{cyl}(t)}{p_{ref}}\right)^{n_1} f\left(T_{form}(t), \lambda_{form}\right)\right] \tag{3.1}$$

and the soot oxidation rate is described as

$$\left.\frac{dm_s}{dt}\right|_{ox} = A_{ox}\frac{1}{\tau_{char}}m_s^{n_2}\left(\frac{p_{O_2}}{p_{O_2,ref}}\right)^{n_3} e^{\frac{T_{A,ox}}{T_{ox}(t,\lambda_{ox})}} \tag{3.2}$$

Recall that this is an extension of the base Hiroyasu model [39], which additionally considers the influences of turbulence (inherently included in $\left.\frac{dm_f}{dt}\right|_{diff}$) and soot chemistry ($\Phi - T$ map approximated using f).

3.3   Relevant Mixture States and MVSM Structure

The MVSM considers five thermodynamic states during the combustion cycle:

ivc The state of the mixture at intake valve closing

soi The state of the mixture after compression and immediately preceding the main fuel injection event

ign The mixture state during the ignition delay of the main injection event

$diff$ A representative mixture state during the diffusion combustion. This state is used as representative for the soot formation process.

ox A mixture state during the expansion process considered as representative for the oxidation process.

All mixture states are determined based on the state ivc and then subsequently used to describe the influences of combustion and engine operation on the soot formation and oxidation processes. Using the above defined states, the combustion process and the soot formation and oxidation are approximated according to the basic structure outlined in figure 3.1. From ivc to soi the mixture is affected only through isentropic compression. At soi, temperature and pressure increases due to the pilot combustion are considered through adiabatic heat addition, resulting in the state ign seen during the ignition delay of the main injection. The state ign is used to determine the duration of the ignition delay, as well as the fuel evaporation process, so that an estimate of the diffusion combustion fraction ξ_{diff} can be obtained. Through adiabatic heat addition the main combustion event is considered and used to evaluate the mixture state $diff$, which is used to determine the soot formation rate and hence formed soot mass. The mixture then undergoes isentropic expansion to the state ox, which, along with the formed soot mass, is used to determine the soot oxidation rate and oxidized soot mass. Finally, the difference between the formed and oxidized soot masses is the soot emission for the given combustion cycle.
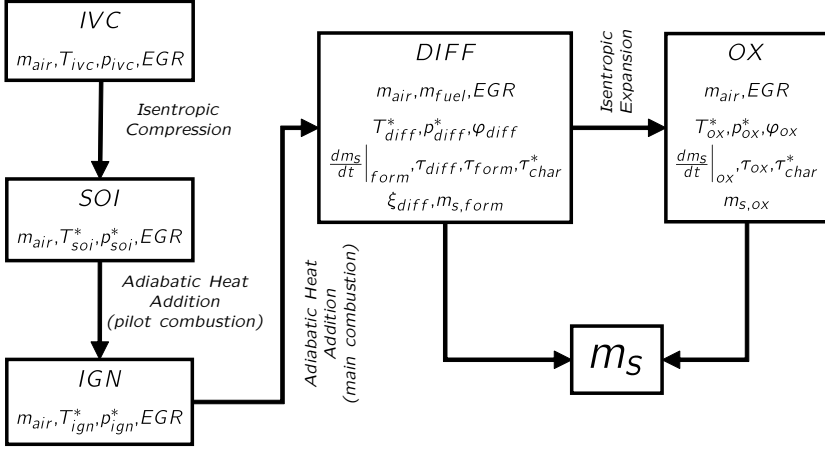
Figure 3.1: Overview of the MVSM structure using defined mixture states

3.4   Derivation of the MVSM

The crank angle resolved model presented in the preceding section is to be reduced, such that the calculation times are significantly reduced (ideally suitable for real-time applications). As a first measure the model reduction will be carried out by representing the existing time (or crank angle) resolved parameters with global and/or cycle resolved parameters. The basic structure of the existing model will be maintained.

In the following discussion, the five representative thermodynamic states are used to approximate the combustion cycle and thereby reduce the soot formation rate, followed by the soot oxidation rate to consider only mean values. Based on these two rates, the final, engine-out soot emissions will subsequently be defined.

3.4.1   Soot Formation Rate

To reduce the calculation times, the instantaneous terms of equation 3.1 are replaced with representative mean values (denoted by "*", see also figure 3.1):

$$\left.\frac{dm_s}{dt}\right|^*_{form} = A_{form}\left(m_f\xi_{diff}\frac{1}{\tau^*_{char}}\right)\left[\left(\frac{p^*_{form}(t)}{p_{ref}}\right)^{n_1}f\left(T^*_{form}(t),\lambda_{form}\right)\right]$$

$$(3.3)$$

where $f\left(T_{form}^{*}\left(t\right),\lambda_{form}\right)$ is a normalized soot yield function from [103] and given by (see section 2.5.1):

$$f\left(T_{form}^{*},\lambda_{form}\right) = \left(\frac{0.75 - \lambda_{form}}{0.65}\right)^{1.5} \cdot \exp\left(-\frac{\left(T_{form} - \mu_0\right)^2}{2 \cdot \sigma_0^2}\right) \quad (2.19)$$

$$\mu_0 = 2160 - 400 \cdot \lambda_{form} \quad (2.20)$$

$$\sigma_0 = 210 - 100 \cdot \lambda_{form} \quad (2.21)$$

T_{form}^{*} and λ_{form} are the representative soot formation zone temperature and relative air-fuel ratio, respectively. The latter being a model parameter which must be determined.

Fuel Conversion Rate

In equation 3.1, the rate of change of the fuel mass due to diffusion combustion must be determined either from measurements or an adequate combustion simulation. As both of these are too time consuming for realtime applications, the following approximation will be used:

$$\left.\frac{dm_f}{dt}\right|_{diff}^{*} = m_{f,main}\xi_{diff}\frac{1}{\tau_{char}^{*}} \quad (3.4)$$

where $m_{f,main}$ is the fuel mass injected during the main ignition, ξ_{diff} is the fraction of the fuel which is combusted during diffusion combustion, and τ_{char}^{*} is a representative characteristic mixing time used to quantify the in-cylinder turbulence.

Diffusion Combustion Fraction The amount of fuel converted during diffusion combustion is assumed to be all fuel which does not evaporate during the ignition delay τ_{ign}. The fuel which has evaporated during the ignition delay is assumed to be converted through premixed combustion and to have no contribution to the soot emissions. Thus the diffusion combustion fraction is approximated as:

$$\xi_{diff} = \left.\frac{m_{f,liq}}{m_{fuel}}\right|_{ign} \quad (3.5)$$

where $m_{f,liq}$ is the liquid fuel within the combustion chamber after the ignition delay *and* any subsequently injected fuel, in the event that the ignition delay is

shorter than the injection duration. The ignition delay itself can be estimated using an empirical correlation [38]:

$$\tau_{ign} = (0.36 + 0.22\bar{v}_p)\exp\left[E_A\left(\frac{1}{R_u T_{ign}^*} - \frac{1}{17190}\right)\left(\frac{21.2}{p_{ign}^* - 12.4}\right)^{0.63}\right]$$
(3.6)

$$E_A = \frac{618840}{CN + 25}$$
(3.7)

where $\bar{v}_p$ is the mean piston speed, E_A is the effective activation energy and the representative temperature T_{ign}^* and pressure p_{ign}^* are discussed in section 3.4.1.

The liquid fuel mass at the end of the ignition delay, is approximated using the d^2 law to describe the fuel droplet evaporation:

$$d_{drop}^2(t) = d_{0,drop}^2 - \beta \cdot t$$
(3.8)

where β is the fuel evaporation coefficient and $d_{0,drop}$ is the initial droplet diameter, assumed to be the same as the injector nozzle diameter.

Assuming a constant injection rate during the ignition delay, the liquid fuel mass remaining in the combustion chamber after the ignition delay is approximated by:

$$m_{f,liq} = \frac{m_{inj,ign}}{2} \cdot \frac{\left(d_{0,drop}^2 - \beta\tau_{ign}\right)^{3/2}}{d_{0,drop}^3}$$
(3.9)

where $m_{inj,ign}$ is the mass of fuel injected during the ignition delay.

Representative Characteristic Mixing Time   The instantaneous characteristic mixing time scale used in the existing soot model to determine the rate of fuel consumption, is described using [7]:

$$\tau_{char} = \frac{l}{u'} = \frac{\left(\frac{V_{cyl}}{\lambda_{diff}\, n_{nozzle}}\right)^{3/2}}{(\underbrace{C_{pm}\bar{v}_p^2}_{\substack{\text{Piston}\\\text{Motion}}} + \underbrace{c_{inj}k_{inj}(t)}_{\substack{\text{Fuel}\\\text{Injection}}})^{1/2}}$$
(3.10)

where the numerator estimates the length scale l from air volume required for the combustion of a single fuel spray and the denominator provides an estimate of the turbulence intensity.

As an approximation, only the contributions of the turbulence generated by the piston motion and the injection are considered in the reduced model. The instantaneous kinetic energy of the injection generated turbulence is defined as:

$$\frac{dk_{inj}}{dt} = \underbrace{-c_{inj,diss}\frac{1}{l_{diss}}k_{inj}^{3/2}(t)}_{\text{Dissipation}} + \underbrace{\frac{1}{2}c_{inj,kin}\dot{m}_{inj}u_{inj}^2\frac{1}{m_{cyl}}}_{\text{Generation}} \tag{3.11}$$

where the first term on the right hand side describes the turbulence dissipation and the second term the turbulence generated by the fuel injection process, each of which are scaled by the respective factors $c_{inj,diss}$ and $c_{inj,kin}$. The injection flow rate $\dot{m}_{inj}$ and the droplet velocity u_{inj} are defined as follows:

$$u_{inj} = \frac{\dot{m}_{inj}}{\rho_{f,liq}A_{nozzle}} \tag{3.12}$$

$$\dot{m}_{inj} = \frac{m_{fuel,inj}}{\tau_{inj}} \tag{3.13}$$

The effective turbulent kinetic energy of the injection generated turbulence, $k_{inj,gen}^*$, can be determined by integrating the generation term of equation 3.11 over the injection duration, τ_{inj}:

$$k_{inj,gen}^* = \frac{c_{inj,gen}u_{inj}^2}{2} \cdot \ln\left(\frac{m_{inj,main}}{m_{air}\left(1 + EGR\right)}\right) \tag{3.14}$$

Shown in figure 3.2 are the calculated generated, dissipated, and net turbulent kinetic energies for two different operating points from the solution of equation 3.11. A representative value of the net turbulent kinetic energy can be obtained by combining equations 3.11 and 3.14 and finding the mean value during the injection process as given in equation 3.16, approximating the dissipation term of equation 3.11 with

$$\int_0^{\tau_{inj}} \frac{c_{inj,diss}}{l_{diss}}k_{inj}^{3/2}(t)dt \approx \frac{c_{inj,diss}}{l_{diss}}\left(\frac{k_{inj,gen}^*}{2}\right)^\alpha \tau_{inj} \tag{3.15}$$

$$k_{inj}^* = \frac{k_{inj,gen}^* - \frac{c_{inj,diss}}{l_{diss}}\left(\frac{k_{inj,gen}^*}{2}\right)^\alpha \tau_{inj}}{2} \tag{3.16}$$

The exponent α was set to 1.46 as this provided representative values of k_{inj}^*, shown as horizontal lines in figure 3.2. Equation 3.15 and the empirically determined exponent α are used, as a realtime solution of equation 3.11 is not possible. An effective mixing timescale can then be approximated by combining
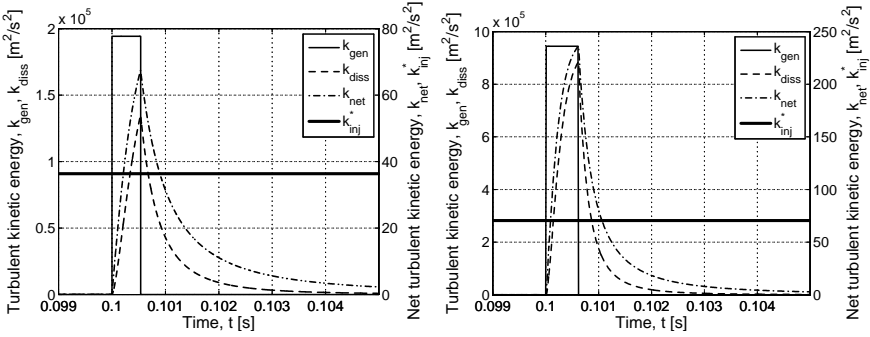
Figure 3.2: Comparison of the calculated and representative turbulent kinetic energies at 2000 rpm and 4 bar BMEP (left) 3000 rpm and 8 bar BMEP (right).

equations 3.10 and 3.16:

$$\tau^*_{char} = \frac{l}{u'} = \frac{\left(\frac{V^*_{tdc}}{\lambda_{diff}\, n_{nozzle}}\right)^{1/3}}{\left(C_{pm}\bar{v}_p^2 + C_{inj}k^*_{inj}\right)^{1/2}} \tag{3.17}$$

Where the representative cylinder volume, V^*_{tdc}, is that of the combustion chamber at top dead center.

Representative Temperature and Pressure During the Ignition Delay

To determine the ignition delay using equation 3.6, a temperature and pressure representative of that within the cylinder must be provided. The temperature and pressure after the pilot combustion event, if present, are taken as being representative for the main combustion event ignition delay. The temperature after the pilot combustion event is estimated by assuming isentropic compression of the fresh air from ivc to soi of the main injection, followed by adiabatic energy addition due to the pilot combustion:

$$T^*_{ign} = T^*_{soi,main} + \Delta T_{pilot} \tag{3.18}$$

$$\Delta T_{pilot} = \frac{LHV \cdot m_{pilot}}{c_p m_{cyl}} \tag{3.19}$$

where LHV is the lower heating value of the fuel, c_p is the specific heat capacity at a constant pressure and is determined using the NASA polynomials [19],

and $T^*_{SOI,main}$ is the representative temperature at the beginning of the main injection event determined assuming isentropic compression and no combustion:

$$T^*_{soi,main} = T_{ivc} \left(\frac{V_{ivc}}{V_{soi,main}} \right)^{\kappa - 1} \tag{3.20}$$

The representative pressure can be determined using the ideal gas law:

$$\boxed{p^*_{ign} = \frac{m_{air} \left(1 + EGR \right) R \cdot T^*_{ign}}{V_{SOI,main}}} \tag{3.21}$$

The respective volumes are determined using the crank-slider mechanism given in [38].

Representative Cylinder Pressure During Soot Formation

In equation 3.1 the instantaneous cylinder pressure is required to determine the soot formation rate. As the instantaneous cylinder pressure is not available on typical production engines, it is replaced with a representative cylinder pressure p^*_{form}, describing the cylinder pressure after the main combustion event. The representative cylinder pressure is influenced by the intake charge pressure p_{int}, the compression ratio of the engine ϵ, the timing of the main injection event SOI_{main}, and the energy added by combustion Q_{comb} relative to the mass of inert gas in the cylinder:

$$p^*_{form} = f \left(p_{int}, \epsilon, SOI, \frac{Q_{comb,main}}{c_v} \right) \tag{3.22}$$

In general, the representative cylinder pressure is described by summation the pressure prior to combustion (p^*_{ign}) and pressure increase due to combustion $\Delta p_{comb,main}$. The influences of the intake pressure p_{int} and compression ratio ϵ are included in p^*_{ign}, while deviations from reference injection timings and pressures are considered by scaling $\Delta p_{comb,main}$:

$$p^*_{form} = p^*_{ign} + \Delta p_{comb,main} \underbrace{\left(\frac{SOI - \varphi_{50}}{SOI_{ref} - \varphi_{50}} \right)^{n_2}}_{\substack{\text{Injection timing} \\ \text{correction}}} \underbrace{\left(\frac{p_{inj}}{p_{inj,ref}} \right)^{n_3}}_{\substack{\text{Injection pressure} \\ \text{correction}}} \tag{3.23}$$

where φ_{50} is the optimum crank angle for the 50% fuel conversion (assumed to be 375 CADaGETDC) and SOI_{ref} is the beginning of injection required such

that the 50% conversion occurs at φ_{50}. For a given φ_{50}, SOI_{ref} is dependant on the ignition delay and combustion rate:

$$SOI_{ref} = \varphi_{50} - \left(\tau_{ign} + \frac{1}{2} \frac{m_{inj}}{\frac{dm_f}{dt}\big|_{diff}} \right) 6\omega \tag{3.24}$$

The ignition delay τ_{ign} has been previously determined using equation 3.6 and the fuel conversion rate $\frac{dm_f}{dt}\big|_{diff}$ by equation 3.4.
Equation 3.23 still requires that the pressure increase due to combustion be specified. Analogous to equation 3.19, the temperature change due to the combustion is first determined assuming adiabatic heat addition, and used to determine the change in pressure using the ideal gas law:

$$\Delta T_{main} = \frac{LHV \cdot m_{fuel,m}}{c_p m_{cyl}} \tag{3.25}$$

$$\Delta p_{comb,main} = \frac{mR\Delta T_{main}}{V(\varphi_{diff})} \tag{3.26}$$

where $V(\varphi_{diff})$ is the representative cylinder volume during diffusion combustion. Through the implementation of the ideal gas law to determine the change in pressure due to the combustion process, the following assumptions are made:

- The mass of the cylinder contents remains constant

- The change in the real gas constant during the combustion process. For fresh air $R_{air} = 287\,J/kg/K$ and for the products of a stoichiometric combustion process $R_{ex} \approx 283\,J/kg/K$. As the global mixture becomes increasingly lean, R_{ex} will approach R_{air} due to the increasing oxygen and nitrogen fractions.

- The cylinder volume remains approximately constant during combustion. As this is not necessarily the case, a representative volume is used.

Soot Formation Temperature

As discussed in section 2.2, soot is formed in regions of the combustion chamber where there is a sufficiently high temperature (higher than 1500 K, [35]), soot precursors, and an oxygen deficit. If it is assumed that all soot is formed in the immediate vicinity of the flame, the local flame temperature is taken as being the representative soot formation temperature:

$$T_{form}^* = T_{ign}^* + \Delta T_{adb} \tag{3.27}$$

The temperature change due to adiabatic combustion is described using:

$$\Delta T_{adb} = \begin{cases} \frac{LHV}{c_p(1+\lambda_{form}m_{air,st})} & \text{if } \lambda_{form} \geq 1, \\\\ \frac{LHV}{c_p(1+\lambda_{form}m_{air,st})}\lambda_{form} & \text{if } \lambda_{form} < 1 \end{cases} \tag{3.28}$$

Where the relative air-fuel ratio of the formation zone λ_{form}, is generally less than unity and is a parameter which must be optimized.

3.4.2 Soot Oxidation Rate

The crank-angle resolved description of the soot oxidation rate (see equation 3.2) requires the instantaneous characteristic mixing time, while in the MVSM it is approximated using the representative characteristic mixing time defined for the formation in equation 3.17. In addition, instantaneous values of the partial pressure of oxygen, soot mass, and oxidation zone temperature are needed. The oxidation rate is considered in the MVSM using equation 3.29, where representative mean values must once again be defined.

$$\left.\frac{dm_{soot}}{dt}\right|_{oxid}^* = A_{oxid}\frac{1}{\tau_{char}^*}m_{soot}\left(\left(\frac{p_{O_2}^*}{p_{O_2,ref}}\right)^{n_4}e^{\frac{-T_{A,ox}}{T_{ox}^s}}\right) \tag{3.29}$$

Partial Pressure of Oxygen

The representative partial pressure of oxygen, $p_{O_2}^*$, should provide an indication of the in-cylinder oxygen content available for soot oxidation during and after the main combustion event. Utilizing the representative formation pressure defined in equation 3.23 and accounting for the pressure decrease due to expansion, the representative partial pressure of oxygen is defined by:

$$p_{O_2}^* = p_{ox}^* y_{O_2} \tag{3.30}$$

with

$$p_{ox}^* = p_{form}^* \left(\frac{V\left(\varphi_{diff}\right)}{V\left(\varphi_{ox}\right)}\right)^{\kappa} \tag{3.31}$$

$$y_{O_2} = \frac{n_{O_2}}{n_{tot,ox}} \tag{3.32}$$

where $V(\varphi_{ox})$ is the representative cylinder volume during the oxidation process, and φ_{ox} is a model parameter which must be determined.

The total number of moles in the cylinder during oxidation, $n_{tot,ox}$, is determined using the ideal gas law with the representative temperatures and pressures defined in equations 3.37 and 3.31, respectively:

$$n_{tot,ox} = \frac{p_{ox}^* V_{ox}}{R_u T_{ox}^*} \tag{3.33}$$

The number of moles of O_2 in the cylinder is defined by the air-fuel ratio and the EGR rate, as shown in equation 3.34. The use of EGR will influence the global relative air-fuel ratio in the combustion chamber during lean operation, as excess air from the preceding combustion event is recirculated into the combustion chamber.

$$n_{O_2} = n_{O_2}\big|_{fr} + n_{O_2}\big|_{egr} \tag{3.34}$$

Equation 3.34 can also be expressed in terms of the measured air mass (kg_{air}/cycle, from the ECU):

$$n_{O_2} = \frac{C_{O_2}}{4.76 \cdot M_{air}} \left[m_{air} \left(1 + EGR\right) - m_{air,st} EGR \right] \tag{3.35}$$

where C_{O_2} is a model constant which accounts for the fact that not all inducted oxygen will be available for soot oxidation and is expected to be smaller than unity.

By combining equations 3.30, 3.33, and 3.35, the representative partial pressure of oxygen is described as:

$$\boxed{p_{O_2}^* = \frac{C_{O_2} R_u T_{ox}^* \left[\left(1 + EGR\right) m_{air} - m_{air,st} EGR \right]}{4.76 \cdot M_{air} V_{ox}}} \tag{3.36}$$

Representative Oxidation Temperature

The temperature relevant to the oxidation of the soot particles is not the same as that relevant to the formation of the particles. Soot oxidation requires a sufficiently high temperature, as well as sufficient oxygen. Thus, the soot oxidation temperature is taken to be that of the bulk mixture during the oxidation phase (after combustion and during the expansion) and is estimated assuming an isentropic expansion process from the *diff* state:

$$T_{ox}^* = T_{diff}^* \left(\frac{V(\varphi_{diff})}{V(\varphi_{ox})} \right)^{\kappa - 1} \tag{3.37}$$

where $V(\varphi_{ox})$ is the cylinder volume representative for oxidation and is a model parameter.

3.4.3 Engine-Out Soot Mass

In the existing soot model, the soot formation and oxidation processes are considered simultaneously - as soon as soot is formed, it can be oxidized. This, however, requires the solution of two coupled differential equations (equations 3.1 and 3.2) which is not suitable for realtime applications. In the MVSM, the entire soot formation process is first considered, and then the oxidation of the formed soot:

$$m_s = m_{s,form} - m_{s,ox} \tag{3.38}$$

where the formed and oxidized soot masses are defined as follows:

$$m_{s,form} = \left.\frac{dm_s}{dt}\right|_{form}^* \tau_{form} \tag{3.39}$$

$$m_{s,ox} = \left.\frac{dm_s}{dt}\right|_{ox}^* \tau_{ox} \tag{3.40}$$

The definition of the respective process durations τ_{form} and τ_{ox} is outlined below.

Soot Formation Duration

The soot formation is assumed to only take place during the diffusion combustion phase. The diffusion combustion duration can, as an approximation, taken to be proportional to the main injection duration:

$$\tau_{form} = C_{diff}\tau_{inj,main} \tag{3.41}$$

Where the scaling factor C_{diff} is of the order 2, under the assumption that the diffusion combustion heat release rate is approximately symmetric about its maximum, which occurs near the end of injection.

Soot Oxidation Duration

Soot oxidation is assumed to take place from the beginning of the diffusion combustion (i.e. when the first soot particles are formed) to the point at which the mixture temperature within the soot oxidation zone drops below a critical

value $T_{min,ox}$, which is a model parameter. The time during which oxidation can take place is then:

$$\tau_{ox} = \frac{\Delta\varphi_{ox}}{6 \cdot \omega} \tag{3.42}$$

where

$$\Delta\varphi_{ox} = \varphi_{T_{min,ox}} - \varphi_{b,diff} \tag{3.43}$$

where $\varphi_{b,diff}$ and $\varphi_{T_{min,ox}}$ are the crank angle at which the diffusion combustion begins and the minimum oxidation temperature is reached, respectively. The beginning of the diffusion combustion is defined by the start of the main injection, and the ignition delay of the main injection event:

$$\varphi_{b,diff} = SOI_{main} + 6 \cdot \omega\tau_{ign} \tag{3.44}$$

where the ignition delay τ_{ign} is defined in equation 3.6.

The oxidation temperature decreases due to heat losses in to cylinder walls and the expanding volume of the combustion chamber, with the later being the dominant factor. Thus, assuming an isentropic expansion of the burned cylinder contents, the volume at which the minimum oxidation temperature is reached, is defined as:

$$V_{min,ox} = V\left(\varphi_{diff}\right) \left(\frac{T^*_{diff}}{T_{min,ox}}\right)^{\left(\frac{1}{\kappa-1}\right)} \tag{3.45}$$

where the initial state is taken as that after the main combustion event, as this state is well characterized. As the engine volume is known as a function of the crank angle ([38], for example), the crank angle at which $V_{min,ox}$ occurs can be determined using a zero finding algorithm (for example `fzero` in Matlab [71]).

3.5 Model Parameters, Inputs and Implementation

The MVSM described above contains 16 model parameters, which require determination for each engine and fuel combination. The parameters introduced in the above derivation are used to describe characteristics of the engine geometry, injection process, combustion process, fuel, and in-cylinder fluid motion

Parameter	Range	Step Size	Description
A_{form}	1e-4...1e5	1e-5	Formation scaling factor
A_{ox}	1...1e10	5	Oxidation rate scaling factor
β	1e-7...1e-5	1e-10	Fuel evaporation coefficient
λ_{diff}	0.8...1.2	0.05	Relative air-fuel ratio for diffusion combustion
λ_{form}	0.01...0.7	0.005	Relative air-fuel ratio in the soot formation zone
$T_{A,ox}$	1e3...1e5	5	Oxidation activation temperature
$T_{ox,min}$	1560...1600	1	Minimum oxidation temperature
c_{pm}	0.1...5	1e-3	Piston motion generated turbulence scaling factor
c_{inj}	1e-6...5	1e-7	Injection generated turbulence scaling factor
c_{diff}	0.5...5	0.005	Soot formation duration scaling factor
c_{O_2}	0.1...5	0.05	Oxygen availability scaling factor
φ_{diff}	360...380	1	Representative crank angle for diffusion combustion
φ_{ox}	360...450	1	Representative crank angle for soot oxidation
n_1	0.5...10	0.01	Soot formation pressure exponent
n_3	-15...0	0.1	Injection pressure correction exponent
n_4	0.01...5	1e-3	Soot oxidation pressure exponent

Table 3.1: Summary of model parameters which require determination for each engine and fuel combination

and are outlined in table 3.1. An evolutionary algorithm implemented by [103] was used to determine the optimal parameter set providing the best agreement between calculated and measured soot emissions.

One of the requirements of the MVSM is that it only uses inputs available from a standard engine control unit. Table 3.2 lists the model inputs and how they were determined for this investigation. Of particular concern is the EGR rate as this is generally not available directly from the ECU and must either be determined by measurement or from a model. In addition, the intake temperature is taken from the ECU value which, while suitable for steady state operation, requires correction for transient conditions due to slow sensor response, though this is discussed in detail in chapter 6. The cylinder pressure at intake valve closing (IVC) is estimated based on the mean manifold pressure under the assumption that at IVC, the cylinder and manifold pressure are approximately equal. If available, a measured or calculated estimate of this pressure would be preferential.

Parameter	Description	Units	Source
φ_{IVC}	Intake valve closing angle	[CAD]	Engine geometry
d_{inj}	Injector hole diameter	[m]	Engine geometry
n_{nozz}	Number of holes per injector	[-]	Engine geometry
n_e	Engine speed	[rpm]	ECU
φ_{SOI}	Start of main injection	[CAD]	ECU
$\tau_{inj,m}$	Duration of main injection	[s]	ECU
p_{rail}	Injection rail pressure	[Pa]	ECU
EGR	EGR rate	[-]	ECU, measurement, model
LHV	Lower heating value of fuel	[MJ/kg]	Fuel property
CN	Fuel cetane number	[-]	Fuel property
M_{fuel}	Molar mass of fuel	[g/mol]	Fuel property
$(A/F)_{stoich}$	Stoichiometric air fuel ratio	[-]	Fuel property
ρ_{fuel}	Fuel density	[kg/m^3]	Fuel property
T_{int}	Intake charge temperature	[K]	ECU, model
$m_{inj,p}$	Pilot injection mass	[g]	ECU
$m_{inj,m}$	Main injection mass	[g]	ECU
m_{air}	Air mass per cycle	[g]	ECU
p_{ivc}	Cylinder pressure at IVC	[Pa]	ECU (manifold pressure)

Table 3.2: Input parameters for the mean value soot model and their respective sources (ECU: Engine Control Unit)

The MVSM was implemented in a Matlab m-function using only simple arithmetic operations to ensure portability, though a built-in zero finding algorithm was used to determine $T_{min,ox}$ (equation 3.45). This implementation on a Pentium 4, 3.0 GHz, 1.0 GB RAM, Windows XP PC resulted in calculation times of 10 ms per cycle. This is in contrast to the existing crank angle resolved model, which had calculation times of 5 s, given that measured cylinder pressure and injection histories are available.

3.6   Model Parameterization using Evolutionary Algorithms

The parameters of the MVSM were determined for three different fuel and engine combinations based on measured soot emissions using evolutionary algorithms [103] [81].
Shown in figure 3.3 is the basic schematic describing how evolutionary algorithms were used to determine the optimum model parameters. The initial
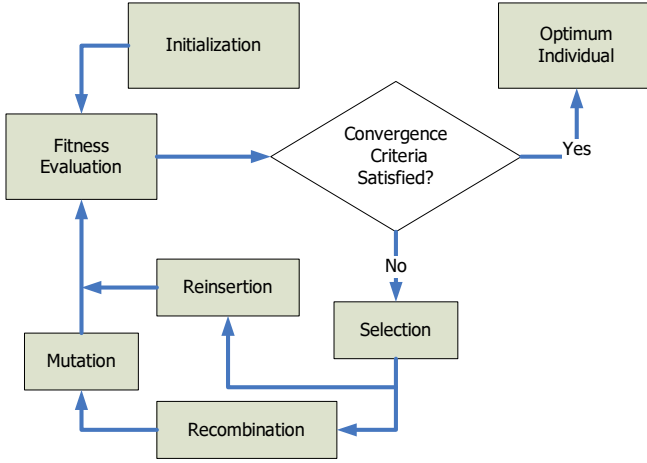
Figure 3.3: General process for determination of the optimum parameter set using evolutionary algorithms. Adapted from [81]

individuals[1] were selected stochastically within specified search regions for each parameter. The fitness[2] of each of the individuals is then determined based on its objective function. For this investigation, the objective function was defined as

$$objective = 1 - R^2 \tag{3.46}$$

where R is the correlation coefficient defined by:

$$R = \frac{\sum_{i=1}^{n_{op}} \left(m_{s,calc,i} m_{s,meas,i} - n_{op} \bar{m}_{s,calc} \bar{m}_{s,meas} \right)}{\left(n_{op} - 1 \right) \sigma_{m_{s,calc}} \sigma_{m_{s,meas}}} \tag{3.47}$$

where $m_{s,meas,i}$ and $m_{s,calc,i}$ are the measured and calculated soot emissions for the ith point, respectively, and n_{op} is the total number of operating points. The correlation coefficient is used for the objective function, as the goal of the parameterization is to maximize the correlation between the measured and calculated soot emissions.

It is also common to use the minimization of mean of the relative squared

---

[1] An individual refers to a set of model parameters
[2] The fitness of an individual is a means of measuring its goodness.

error, $\bar{\delta}^2$ as the fitness function,

$$\bar{\delta}^2 = \frac{\sum \sqrt{\left(\frac{m_{s,calc,i} - m_{s,meas,i}}{m_{s,meas,i}}\right)^2}}{n_{op}} \tag{3.48}$$

though it was found that for the MVSM this can lead to the optimum parameter set not reproducing the extreme operating points.

Based on each of the individual's fitness values, n individuals are selected to be used as the *parents*[3] for forming the *offspring*[4] of the following *generation*[5]. The objective function of the newly formed offspring are determined and used to determine if the convergence criteria has been reached. If the convergence criteria has not been fulfilled, the n best individuals from the offspring are selected and used as the parents to form the next generation of offspring. It is also possible to keep the best parents from each generation unchanged so the the best individual is propagated through all generations, a process termed *reinsertion*. The parameters of the implemented evolutionary algorithm can be found in table A.7.

3.7   Summary

Through the reduction of an existing crank-angle-resolved soot model, a mean value soot model (MVSM) was developed. This reduction was carried out through the consideration of five representative mixture states used to describe various aspects of the combustion and soot formation and oxidation processes. In addition, the time resolved processes were instead considered using representative mean values which resulted in a total of 16 model parameters used to describe each engine and fuel combination. To ensure suitability for production applications, the MVSM considers only parameters available from the ECU as inputs, though some parameters such as EGR are more accurately taken from measurements or other fast models. Using the configuration of the MVSM presented in this chapter resulted in calculation times of 10 ms per operating point, thus fulfilling the calculation time requirements. After chapters 4 and 5 present the experimental methodology and experimental results, respectively, the performance of the MVSM will be evaluated in chapter 6.

---

[3]The parents are the individuals used as a basis for forming new individuals in the next generation.

[4]The offspring are the result of the mutation and recombination of the parents.

[5]A generation is the loop formed by generating offspring from parents from a previous generation, and using these offspring to as parents for the next generation.

Chapter 4

Experimental Methodology

4.1   Introduction

The validation of the MVSM required the measurement of the exhaust stream soot concentration along with the engine operating parameters during steady state and transient engine operation. To further investigate the fundamental influences of the engine operating parameters and fuel properties on the soot emissions, in-cylinder soot concentration measurements and a combustion analysis were implemented. This chapter outlines the engines, fuels, instrumentation and methodologies used for the measurements, with particular focus on the transient measurements. The latter required novel methods for the determination of the EGR rate and intake charge temperature. Whenever possible, each of the implemented methodologies is validated against a suitable reference to ensure its suitability.

4.2   Engines and Fuels

Steady state soot emission measurements from two different engines operating with three different fuels were used for the validation of the MVSM. Additionally, measurements of the soot emissions during transient engine operation from one engine were used for validation of the MVSM. These two engines, the implemented fuels, and the considered operating points are briefly outlined below.

4.2.1   DaimlerChrysler OM611

Steady-state and transient measurements were carried out on a Daimler-Chrysler OM611 common rail diesel engine equipped with a variable turbine geometry turbocharger and high pressure EGR system [50], [79]. The general specifications of the engine can be found in table 4.1, while a detailed description of the testbench is given in [4], [86], and[5].

Parameter	DC OM611	Engine Two
Number of cylinders	4	4
Swept volume	2.15 [l]	1.97 [l]
Compression ratio	19:1 [-]	16:1 [-]
Stroke	88.4 [mm]	95.5 [mm]
Bore	88 [mm]	81 [mm]
Number of valves	4	3 (2 Intake, 1 Exhaust)
Engine control	EDC 15	EDC 16
Aspiration	VTG	VTG
EGR	Yes	Yes
Max. injection pressure	1350 [bar]	1800 [bar]
Soot instrumentation	AVL Micro Soot Sensor	Filter Smoke Number
Application	Steady State / Transient	Steady State

Table 4.1: Comparison of main specifications of the two engines used for the MVSM parameterization

The steady state measurements on the OM611 were carried out using two different fuels, which are summarized in table 4.2. The reference fuel is representative of a current diesel fuel available for consumer use in Switzerland. Fuel two was selected due to its markedly different properties, particularly from a soot emissions standpoint. A larger pre-mixed fraction is expected due to the lower evaporation temperature, coupled with a lower cetane number (longer ignition delays). Furthermore, the low aromatic content of fuel two was expected to decrease the soot formation rate, as it is necessary to generate the PAH directly from the fuel molecules[1][94]. Also listed in table 4.2 is fuel three which is similar to the reference fuel and was used for steady-state measurements on engine two.

---

[1]Note that the formation of the first PAH is the rate-limiting step for soot formation, see section 2.2.1.

Parameter	Reference	Fuel Two	Fuel Three	Units
Density	829	776	833	kg/m3
Evaporation Temperature	336	226	347	°C
Cetane Number	51	43	54	-
Sulfur Content	9.5	< 10.0	8.0	mg/kg
Aromatic Content (Masse)	18.6	1.9	18.5	%
Viscosity (at 40°C)	2.33	1.07	2.60	mm2/s
Engine	OM611	OM611	Engine Two	-
Application	stat./trans.	stat.	stat.	-

Table 4.2: Comparison of main specifications of the three fuels used for the MVSM parameterization

Steady-State Measurements

The steady state soot emissions from the OM611 were measured using both the reference fuel and fuel two (see table 4.2) over a wide range of the operating map. Each operating point was defined through the prescription of the engine speed (held constant by the engine dynamometer) and brake mean effective pressure (defined through a variation of the ECU gas pedal position), while all remaining engine parameters were defined by the production engine control unit. A detailed listing of the considered operating points are given the appendix (see section A.1). It should be noted that while high load and high speed operating points ($BMEP > 11$ bar, $n > 3250$ rpm) where not considered, the investigated region of the operating map did nonetheless include operation with and without pilot-injection and EGR.

To ensure a high measurement repeatability, a steady state reference operating point (3000 rpm, and $BMEP = 8$ bar) was measured prior and following every measurement campaign, as well as on several occasions during the campaign. This operating point was considered instead of the typical mid-speed, low-load point (2000 rpm, $BMEP = 3$ bar), as the higher exhaust gas velocities are thought remove particulate deposits in the exhaust system, which may otherwise dislodge during measurements thereby introducing error.

To ensure that the engine has reached a steady state operation prior to the measurement, the engine was allowed to run at each operating point until the exhaust manifold gas temperature had a variation of less than 1 K in 10 s.

Transient Operating Points

The soot emissions from the OM611 were also measured during transient engine operation, not only to validate the performance of the MVSM during transient operation, but also to gain insight as to the influence of transient engine operation on the soot emissions. The following two types of transients considered to be representative of those seen by an engine in a passenger vehicle were selected:

Acceleration During an acceleration transient, the engine speed is linearly increased while the engine load is held constant. The duration of an acceleration transient is defined by the dynamics of the vehicle.

Tip-in During a tip-in transient, the engine load (gas pedal position) is linearly increased while the engine speed is held constant. The duration of the tip-in transient can be arbitrarily defined but is usually considered to be in the region of 0 to 10 s [36].

The acceleration durations were determined through the consideration of the vehicle dynamics described using:

$$\frac{du_v}{dt} = \frac{\frac{-1}{2}C_d\rho_a A - C_r m_v g + M_e R_{trans,i} R_{diff} r_w}{m_v} \tag{4.1}$$

$$\omega(t) = \frac{30 u_v(t) R_{diff} R_{trans,i}}{\pi r_w m_v} \tag{4.2}$$

where u_v is the vehicle speed, C_d is the aerodynamic drag coefficient, A is the frontal surface area of the vehicle, C_r is the rolling resistance coefficient, ω is the engine speed, $R_{trans,i}$ and R_{diff} are the transmission ratios of the ith gear and the differential respectively, and r_w is the radius of the wheel. The remaining parameters of the vehicle dynamics model described by equations 4.1 and 4.2 are given in the appendix. From this model the durations for an acceleration from 1250 rpm to 3000 rpm at $BMEP = 8$ bar were determined and are listed in table 4.3. The acceleration transients were implemented on the transient dynamometer by maintaining a constant gas pedal position, while linearly increasing the engine speed according to the durations specified in table 4.3.

The rotational moment of inertia $\Theta_{d,e}$ of the coupled engine and dynamometer system was accounted for using

$$M_e = \dot{\omega}_{d,e}\Theta_{d,e} + M_d \tag{4.3}$$

	Engine Speed [rpm]	*BMEP* [bar]	Transient duration [s]
Acceleration	1250→3000	8	2.29 (1st gear)
	1250→3000	8	7.60 (2nd gear)
	1250→3000	8	21.9 (3rd gear)
Tip-In	1250	2→8	0.5, 1.0, 2.0, 5.0
	2000	2→8	0.5, 1.0, 2.0, 5.0

Table 4.3: Specifications of the investigated acceleration and tip-in transients.

where M_d is the braking moment measured by the dynamometer. A rotational moment of inertia of 0.29 kg/m^2 was used, as this was found to provide an accurate reproduction of a constant braking moment during engine speed transients.

In addition to the same steady state reference point already discussed the engine was also conditioned prior to all transient measurements. This included running the engine at the reference point until the exhaust temperature was stable, followed by five repetitions of the fastest acceleration transient to dislodge any additional soot deposits in the exhaust system.

4.2.2 Engine Two

To investigate the ability of the MVSM to reproduce the soot emissions from another engine, measurements from a four cylinder research engine (Engine two in table 4.1) were delivered from and external project partner. The primary differences between the two engines lies in the newer control system (EDC 16 vs. EDC 15 for the OM611) and its associated higher injection pressure, the different cylinder geometry and the implemented soot instrumentation. The soot emissions from engine two were determined using a Filter Smoke Number (FSN) system and the empirical correlation from [23] (see equation 2.1) to determine the elementary carbon concentration. Not only do the measurements from the engine two provide the opportunity to validate the MVSM against measurements from another engine, but also against measurements obtained using a different soot measurement technique.

Considered Operating Conditions

Two sets of soot measurements were considered for engine two: 1) standard engine speed/load operating map points (with the remaining engine parameters being set by the ECU) and; 2) prescribed variations of the engine speed, load, pilot and main injection timing, injection pressure, pilot injection fuel mass, and EGR rate. All measurements were carried out using fuel 3 (see table 4.2) under steady-state operation.

It should be noted that for the standard engine speed/load operating points, the EGR rate was not directly measured and was estimated according to:

$$EGR \approx 1 - \frac{120 \cdot \dot{m}_a \cdot R_a \cdot T_{ivc}}{p_{cyl,ivc} \cdot V_{ivc} \cdot n} \tag{4.4}$$

To validate the applicability of equation 4.4, it was used to determine the EGR rate for the parameter variations and compared to the measured EGR values[2], as shown in figure 4.1. While the general trend of the EGR was reproduced by equation 4.4, there are considerable errors in the EGR rate, particularly for lower measured values. This correction was only used for the engine speed/load points measured on engine two as measured values of the EGR rate were not available. As will be discussed in chapter 6, accurate knowledge of the EGR is a necessity for the calculation of the soot emissions and the model performance suffers without it.

4.3   Instrumentation

As dictated by the goals of this investigation, whenever possible, measurements of the engine operating parameters were taken using the ECU. Additional sensors, however, were added to provide complementary information regarding the engine operation. The additional, non-ECU instrumentation is outlined in figure 4.2, while an overview of the ECU instrumentation is available in [84]. Of particular importance to this investigation was the measurement of the EGR rate, the intake charge temperature and the relative oxygen-fuel ratio, during both steady-state and transient operation. The methodologies used for the measurement of these three parameters are discussed in detail below.

---

[2]The EGR rate was determined on the basis of measured CO_2 concentrations in the intake and exhaust gas streams.
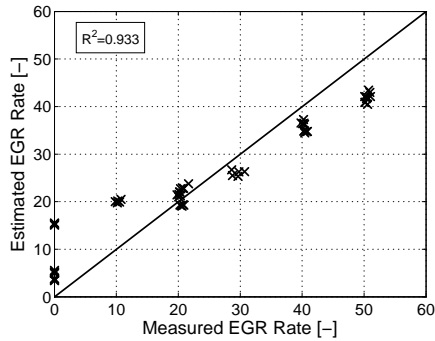
Figure 4.1: Comparison of the estimated (equation 4.4) and measured EGR rates for parameter variations on engine two.

4.3.1 EGR Measurement

The fraction of the recirculated exhaust gases in the intake charge, EGR, was defined as:

$$X_{EGR} = \frac{n_{EGR}}{n_{total}} \tag{4.5}$$

and was quantified on the basis of the measured CO_2 concentrations in the exhaust and intake gas streams. During steady state operation, the CO_2 concentrations were measured directly using NDIR analyzers, whereby low sample flow rates were used for the intake stream measurements to ensure minimal impact on the charge pressure. For the transient measurements it was necessary to develop another means of determining the CO_2 concentrations as the NDIR samplers did not have a sufficiently fast response time. Additionally, the calculation of the EGR rate required consideration of the water vapor which is removed from the exhaust stream prior to CO_2 measurement. The details of the steady state and transient EGR determination are outlined below.

EGR Measurement: Steady-State

To determine the EGR rate during steady state operation, the CO_2 concentrations in the intake and exhaust streams were determined using NDIR analyzers. As the CO_2 concentrations are measured after the water vapor has been removed through condensation [3], a correction of the measured CO_2 concen-

---

[3]The water vapor is removed to prevent condensation within analyzer, which may damage or contaminate the measurement cell.
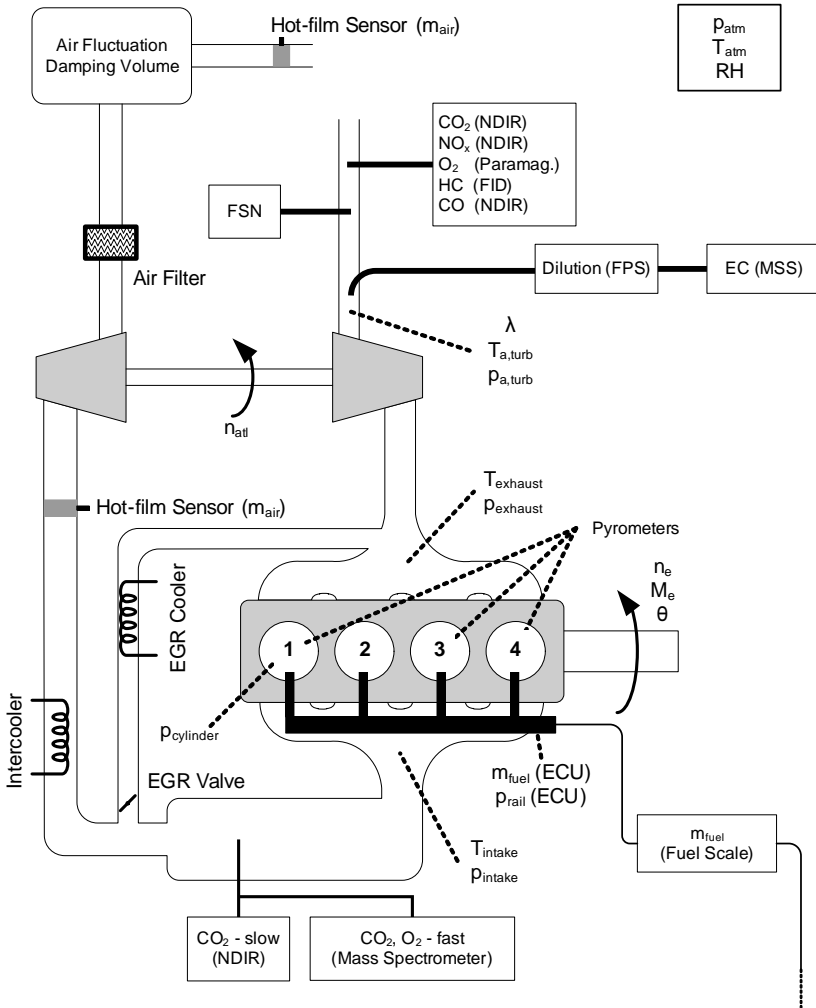
Figure 4.2: Overview of non-ECU instrumentation on the OM611.

trations is required. The amount of water vapor in the exhaust stream can be estimated from the combustion stoichiometry with knowledge of the air fuel ratio and EGR rate. Because of the coupling of the EGR rate and the water vapor fraction, the EGR rate is determined in an iterative fashion.

The actual intake stream CO_2 concentration $X_{CO_2,mix}^w$ can be determined from the measured (dry) CO_2 concentration $X_{CO_2,mix}^d$ using

$$X_{CO_2,mix}^w = X_{CO_2,mix}^d \left[1 - \frac{\frac{1-X_{EGR}}{X_{EGR}} \cdot X_{H_2O,fr}^w + X_{H_2O,ex}}{\frac{1-X_{EGR}}{X_{EGR}}+1} \right] \qquad (4.6)$$

where w and d refer to wet and dry measurements, mix is the mixture of fresh air and EGR measured in the intake manifold, fr is the fresh air (prior to EGR mixing), and ex is the exhaust stream. The mole fraction of the water in the intake air $X_{H_2O,fr}^w$ is determined from a measurement of the relative humidity. The mole fraction of water in the exhaust stream, $X_{H_2O,ex}^w$ can be determined using:

$$X_{H_2O,ex}^w = \frac{\zeta - X_{CO_2,ex}^d \left(-\frac{y}{x} + \zeta + \frac{\zeta y}{2x} \right)}{1 - X_{CO_2,ex}^d \left(-\frac{y}{x} + \zeta + \frac{\zeta y}{2x} \right)} \qquad (4.7)$$

$$\zeta = \frac{\lambda \left(X_{H_2O,f}^w - X_{CO_2,f}^w \right)}{4.76 \cdot \lambda - 1} \qquad (4.8)$$

where λ is the relative air fuel ratio determined from the excess oxygen in the exhaust stream and y/x is the fuel's hydrogen-carbon ratio.

The exhaust stream CO_2 mole fraction is given by:

$$X_{CO_2,ex}^w = X_{CO_2,ex}^d \left(1 - X_{H_2O,ex}^w \right) \qquad (4.9)$$

Finally, the EGR mole fraction can then be determined using:

$$X_{EGR} = \frac{X_{CO_2,fr}^w - X_{CO_2,mix}^w}{X_{CO_2,mix}^w - X_{CO_2,ex}^w} \cdot \frac{1}{1 + \frac{X_{CO_2,fr}^w - X_{CO_2,mix}^w}{X_{CO_2,mix}^w - X_{CO_2,ex}^w}} \qquad (4.10)$$

EGR Measurement: Transient

Due to the slow response and long gas transport time associated with the implemented NDIR analyzers, the intake CO_2 concentration was measured using a fast mass spectrometer and the exhaust stream CO_2 concentration was estimated based on the measured relative air fuel ratio, for the transient

measurements. The mole fraction of the recirculated exhaust gases in the intake stream is then:

$$X_{EGR} = \frac{n_{ex,int} \left(n'_C + n'_H + \lambda \alpha_{st} \cdot 3.76 + (\lambda - 1) \alpha_{st} \right)}{\lambda \alpha_{st} \cdot 4.76 + n_{ex,int} \left(n'_C + n'_H + \lambda \alpha_{st} \cdot 3.76 + (\lambda - 1) \alpha_{st} \right)} \quad (4.11)$$

where $n_{ex,int}$ is the number of moles of exhaust gas in the intake stream per mole of injected fuel, α_{st} is the stoichiometric number of moles of oxygen per mole of fuel and:

$$n'_C = X_c \cdot \frac{M_f}{M_C} \quad (4.12)$$

$$n'_H = X_H \cdot \frac{M_f}{M_H} \quad (4.13)$$

where M_f, M_C, and M_H are the molar masses of the fuel[4], carbon and hydrogen, respectively. The number of moles of exhaust in the intake stream can be determined using:

$$n_{ex,int} = \frac{X^w_{CO_2,int} \cdot \lambda \alpha_{st} \cdot 4.76}{1 - X_{CO_2,int} \cdot \left(n'_C + n'_H + \lambda \alpha_{st} \cdot 3.76 + (\lambda - 1) \alpha_{st} \right)} \quad (4.14)$$

where the mole fraction of CO_2 in the intake $X^w_{CO_2,int}$ is measured directly by the mass spectrometer.

Shown in figure 4.3 is an operating point specific comparison of the EGR rates measured using the two different methods (i.e. 2 NDIRs; and λ-sensor and mass spectrometer) during steady state operation with reference fuel on the OM611. While a good correlation between the methods can be seen, it should be noted that there is still a relative error of approximately 15% for high EGR rates. As the mass spectrometer and λ-sensor can be used to measure the EGR rate during steady-state operation, it is assumed that this method is also valid for transient measurements, given that the dynamic response of the sensors and gas transport times are accounted for (see section 4.4.4).

4.3.2 Mean Cylinder Temperature Estimation

It was found that the measurement of the intake charge temperature was too slow for transient measurements and that the performance of the MVSM could be improved by using an estimate of the mean charge temperature at intake

---

[4]The molar mass of the fuel is assumed to be 170 g/mol [38].
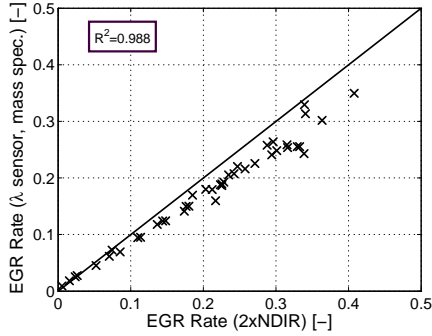
Figure 4.3: Comparison of the two methods for EGR rate determination. OM611, steady state operation, reference fuel.

valve closing (see section 6.4.1). Additionally, this temperature proved to be useful in the analysis of the measured transient soot emissions. To estimate this temperature, the ideal gas law and an engine specific correction function were used:

$$T_{ivc,est} = \frac{p_{ivc}V_{ivc}}{R_{mix}m_{air}\left(1 + \frac{EGR}{1+EGR}\right)} \cdot f_{corr}\left(p_{ivc}, EGR, T_{egr}, n\right) \qquad (4.15)$$

where the correction function f_{corr} accounts primarily for the influences of heat transfer and other inaccuracies that are present to the simplistic nature of this estimate. The correction function is of the form:

$$f_{corr} = C_1 \cdot p_{ivc}^{n_1} \cdot T_{EGR}^{n_2} \cdot EGR^{n_3} \cdot n^{n_4} + C_2 \qquad (4.16)$$

where the constants (C) and exponents (n) were heuristically determined based on the measured temperatures in the intake port during steady state operation. The agreement between the measured and estimated intake charge temperature charges are shown in figure 4.4. The goal of equation 4.15 is not to provide a quantitatively exact estimate of the charge temperature, rather to provide a basis for comparison of the charge temperatures during transient and steady operation.

4.3.3 Relative Oxygen-Fuel Ratio

As the in-cylinder oxygen availability has a strong influence on the soot emissions (see for example figure 2.6), the molar relative oxygen-fuel ratio was
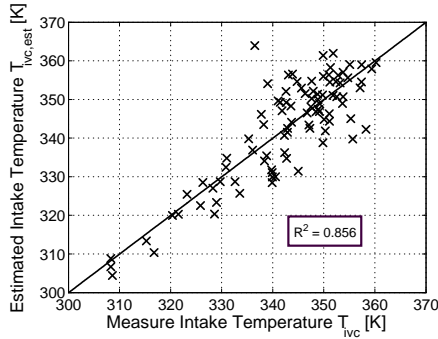
Figure 4.4: Comparison of the measured and estimated (see equation 4.15) intake temperature during steady state operation.

determined for all measurements according to:

$$\lambda_{O_2} = \frac{\left(\frac{n_{O_2}}{n_f}\right)_{actual}}{\left(\frac{n_{O_2}}{n_f}\right)_{stoich}} \tag{4.17}$$

where n_{O_2} is the number of mole of oxygen in the combustion chamber and considers oxygen in the fresh air as well as in the recirculated exhaust gases, as this becomes relevant during lean operation. As the oxygen concentration is typically measured, the following form of equation 4.17 after consideration of the ideal gas law is used:

$$\lambda_{O_2} = \frac{X_{O_2} \cdot p_{ivc} \cdot V_{ivc} \cdot M_{O_2}}{0.2331 \cdot R_u \cdot T_{ivc} \cdot m_f \cdot m_{a,st}} \tag{4.18}$$

where M_{O_2} is the molar mass of oxygen and the mole fraction of oxygen, X_{O_2} can be determined based on the relative air-fuel ratio and the EGR rate (from equation 4.11):

$$X_{O_2} = \frac{\lambda + (\lambda - 1) \cdot EGR}{4.73 \cdot \lambda \cdot \left(1 + \frac{EGR}{1-EGR}\right)} \tag{4.19}$$

Shown in figure 4.5 is a comparison of the oxygen fractions estimated using equation 4.19 against the oxygen fraction directly measured in the intake manifold using a mass spectrometer. It should be noted that while an acceptable qualitative agreement is possible, as indicated by the relatively high correlation coefficient ($R^2 = 0.89$), the quantitative agreement is somewhat lacking.
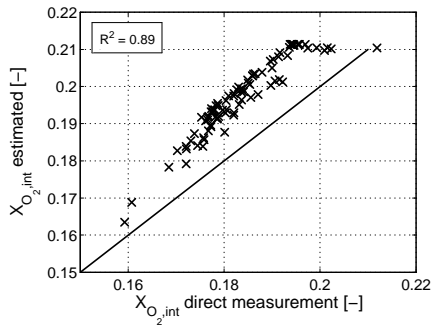
Figure 4.5: Validation of the intake oxygen fraction estimate (equation 4.19) against measured values (mass spectrometer). OM611, steady-state operation, reference fuel.

This poor quantitative agreement is likely due to the high drift of the mass spectrometer observed for measuring oxygen in high concentrations[5].
The use of the relative oxygen-fuel ratio provides a measure of the total oxygen availability in the combustion chamber. The main advantage of this, is that the net effect of the inducted air-fuel ratio, EGR rate, charge pressure, fuel quantity, and intake charge temperature - with regard to the oxygen concentration - can be described with one parameter. It is, of course still necessary to consider each of these and their effects on the soot emissions individually.

4.4 Exhaust Stream Soot Measurement

The goal of this investigation is the calculation of the engine out soot mass emission of a modern diesel engine steady-state and transient operation, which places several constraints on the implemented soot instrumentation to be used for the MVSM validation measurements:

- The soot mass should be measured as directly as possible, avoiding the use of any correlations or conversions from other types of soot measurements (such as size or number distributions).

---

[5]During the course of the intake oxygen concentration measurements a re-calibration of the mass spectrometer was carried out every 10-15 operating points due to an observable drift. This drift was *not* evident when the mass spectrometer was used to measure the CO_2 concentration.

- The response time of the system should be such that it can be used for the measurement of transient soot emissions.

- The detection limit of the system should be sufficiently low so that the soot emissions from modern diesel engines can be accurately quantified.

- Ideally the system should be sensitive to only elementary carbon, as this is what the MVSM predicts. There is no consideration of volatile particles or adsorbed species on the particles.

Through consideration of these constraints, a soot measurement system composed of a Photo-Acoustic Soot Sensor (PASS, commercially available as the AVL Micro Soot Sensor) and a combination of a porous tube and ejector diluter dilution system (Dekati Fine Particle Sampler) was selected. For steady state comparison measurements an AVL 415 Smoke Meter (FSN) was used. Each of the components of the exhaust stream soot instrumentation are briefly discussed below.

4.4.1   Filter Smoke Number

The filter smoke number method for soot emission measurement is commonly used due to its simple implementation and robust configuration. It provides a standardized measure of the blackening of a reference paper after soot-laden exhaust gas has been drawn through the paper. The paper blackening number is measured by comparing the reflectance of the paper before and after sampling. If a standardized volume[6] of exhaust gas is drawn through the paper, the paper blackening is the same as the Filter Smoke Number. FSN is an absolute measure of the particulate emissions from the engine, while the paper blackening is also a measure of the amount of exhaust drawn through the sample [23]. As already given in equation 2.1, FSN can be converted to the elementary carbon concentration. The soot emissions from both engines were characterized using FSN. In the case of engine 2, this was the primary means of soot measurement, while for the OM611, FSN was measured for means of comparison with MSS measurements.

4.4.2   Photo-Acoustic Soot Sensor

The photo-acoustic soot sensor (PASS) provides a time resolved measurement of the elementary carbon concentration, $[EC]$ [87], [21], [9]. As the name

---

[6]The standardized exhaust volume is defined as $405 mm \cdot A$, where A is the sample area of the filter paper [42].
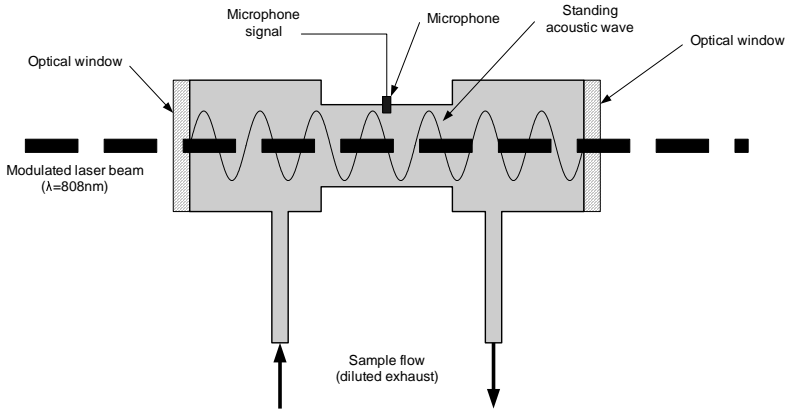
Figure 4.6: General schematic of the PASS operating principle (used by the AVL MSS). Adapted from [87]

implies, the operating principle of the PASS is based on the photo-acoustic effect first noted by [11] and can be seen in figure 4.6. Diluted exhaust gas is passed through a chamber, which on both ends has optical accesses through which a modulated laser beam passes. Particles absorb energy from the laser beam and are heated, resulting in an expansion of the surrounding gas. As the laser beam is modulated, the heating process is periodic leading to and expansion and contraction cycle of the gas. If the laser modulation frequency is the same as the resonant frequency of the measurement chamber ($\sim$ 4.2 kHz), the amplitude of the resulting standing wave can be quantified using a microphone. The amplitude of the microphone signal has been seen to be proportional to the elementary carbon concentration [9], [80].

The sensitivity of the PASS to only elementary carbon is the result of several considerations. In general, elementary carbon is the primary absorber of light in the near infrared and visible spectrum [14]. [23] found that absorption coefficient of elementary carbon remained approximately constant (within 10%) regardless of adsorbed species such as hydrocarbons or even sulfate particles, given that the organic fraction is less than 90%. Absorption of the laser light by other species, such as CO_2 or H_2O can be prevented through selection of the laser wavelength in the near infrared[7]. This investigation used the AVL Micro Soot Sensor (MSS) implementation of the PASS principle.

---

[7]The implemented AVL Micro Soot Sensor operated at a laser wavelength 808 nm.
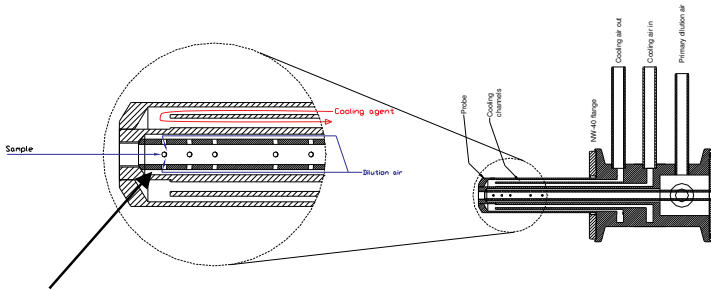
Figure 4.7: Schematic representation of the porous tube diluter used in the Dekati FPS [25].

4.4.3   Dilution System

To match the measurement range of the MSS and to prevent premature window contamination the exhaust gas was extracted and diluted using a Dekati Fine Particle Sampler (FPS), as shown in figure 4.2. The FPS is a two stage sampling and dilution system composed of a porous tube and ejector diluter [65], as shown in figures 4.7 and 4.8, respectively.
As the raw exhaust gas is drawn through the porous tube diluter, it is mixed with dilution air introduced through the walls of the tube. The dilution ratio of this first stage is influenced by the flow rates of the raw exhaust sample and the dilution air. The dilution air flow rate is controlled using a mass flow controller, while the flow rate of the diluted mixture leaving the porous tube diluter, and hence the flow rate of the raw exhaust entering the diluter is a defined by the ejector diluter. By introduction of dilution air into the ejector diluter, a low pressure region is formed, drawing exhaust from the porous tube diluter into the ejector diluter. The volumetric flow rate of exhaust gas entering from the porous tube diluter can be determined from the volumetric flow rate of the dilution air and pressure drop across the ejector diluter [51]. By varying the mass flow rates of the dilution air into the two diluters it is possible to control the dilution ratio over a range from 5:1 to approximately 200:1. For all measurements presented in this investigation, the dilution was in the range of 10:1 to 30:1 depending on the operating point of the engine. The dilution ratio is provided as an output from the FPS with a 1 Hz resolution.
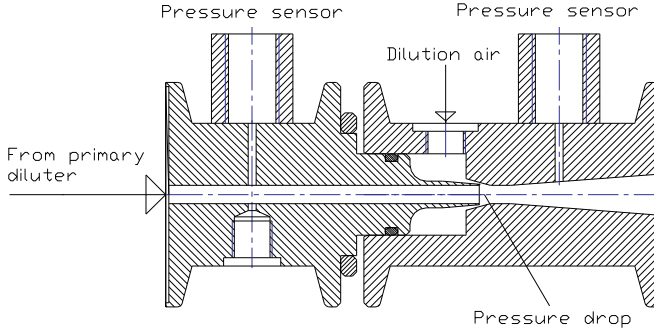
Figure 4.8: Schematic representation of the ejector diluter used in the Dekati FPS [25].

Calculation of Soot Emission Mass

As mentioned above, the MSS provides a measure of the elementary carbon concentration of the diluted exhaust gas in the measurement chamber, though of interest is the mass of emitted elementary carbon emitted from the engine. The raw elementary carbon concentration in the exhaust stream, $[EC]_{raw}$, can be determined from the measured diluted elementary carbon concentration, $[EC]_{raw}$, and the dilution ratio, DR:

$$[EC]_{raw} = DR \cdot [EC]_{dil} \cdot \left(\frac{T_{cell}}{T_{ex}} \right) \tag{4.20}$$

where T_{cell} is the temperature of the diluted exhaust gas in the measurement cell[8] and T_{ex} is the exhaust gas temperature at the sampling point. The mass flow rate of elementary carbon $\dot{m}_{EC}$ can be determined through consideration of the exhaust mass flow rate, which is approximated as the sum of the air and fuel mass flow rates[9], $\dot{m}_{air}$ and $\dot{m}_f$, respectively.

$$\dot{m}_{EC} = (\dot{m}_{air} + \dot{m}_f) \cdot \frac{R_{ex} \cdot T_{ex}}{p_{ex}} \cdot [EC]_{raw} \tag{4.21}$$

---

[8]The measurement cell temperature is held constant at 52° in agreement with the current sampling guidelines for gravimetric measurements [29].

[9]This assumes conservation of mass across the engine from the intake system to the exhaust system and that any mass lost due to blow-by is negligible.
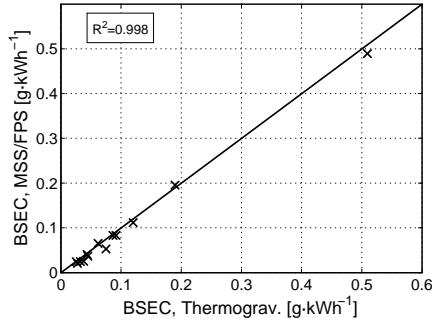
Figure 4.9: Comparison of the brake specific elementary carbon emissions measured using the MSS/FPS system and a thermogravimetric analysis [99].

where p_{ex} is the exhaust pressure at the sampling point. From the mass flow rate of elementary carbon, the brake specific elementary carbon emissions is determined using:

$$BSEC = \dot{m}_{EC} \cdot M_e \cdot \omega \cdot (12 \cdot \pi) \qquad (4.22)$$

where M_e is the measured braking moment.

Steady-State Validation

To validate the accuracy of the complete soot measurement system (MSS and FPS) as well as the soot mass calculation methodology, the measured soot masses were compared to those measured using a gravimetric analysis. The soot emissions were measured at 13 operating points on a heavy duty diesel engine (see table A.4 for details) using the MSS/FPS system as well as a thermogravimetric analysis [99], which provides the total particle mass, as well as the fraction of organic and elementary carbon. The brake specific soot emissions measured using the MSS/FPS were in excellent agreement with those measured using the thermogravimetric analysis, as shown in figure 4.9. It should be noted that this agreement was achieved despite elementary carbon fraction ranging from 28% to 89%.

An additional validation of the MSS/FPS method was carried out through a comparison with the FSN method (see section 4.4.1). In particular, the soot emissions were measured at approximately 130 steady state operating points for operation with two different fuels. When the measured raw soot concentration (at STP) is compared with the FSN values, as well as the
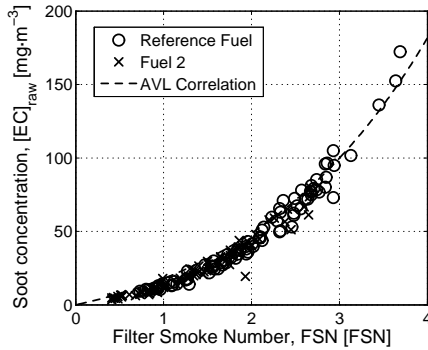
Figure 4.10: Comparison of the soot emissions measured using the MSS/FPS system and FSN. The correlation between FSN and soot concentration (equation 2.1 [23]) is provided as a reference

correlation between FSN and soot concentration (equation 2.1, [23]) a good agreement is seen between the two methods, for both of the considered fuels, as shown in figure 4.10.

4.4.4 Instrumentation Dynamic Response Characterization

So that the soot emission measurements during transient operation can be used to elucidate the influences of engine operation on the soot emissions, the measured soot emissions must *temporally* correspond to the engine parameter measurements. In particular, it is necessary to consider the gas transport times of the exhaust samples from the engine, through the dilution system, to the measurement cell in the MSS. Additionally, the response time of the MSS and any effects of gas mixing which should also be considered. The method presented by [2] and [1] was roughly[10] followed for the correction of the raw signal.

The gas transport time can be corrected using

$$y(t) = u(t - \Delta t) \tag{4.23}$$

---

[10]In [1] a second order system is considered, though here only a first order system is considered to avoid a subsequent differentiation of the raw signal. It was found that a second differentiation required such a significant smoothing of the raw signal to prevent noise amplification (from the differentiation), that it resulted in a loss of signal information.
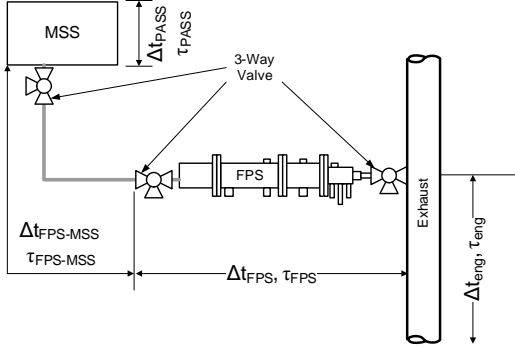
Figure 4.11: Installation of the three-way valve to generate step-changes in the soot concentration for dynamic response characterization.

where $y(t)$ is the measured soot concentration at time t, $u(t)$ is the actual soot concentration at time t, and Δt is the time required for the exhaust gas to travel from the exhaust system to the MSS measurement cell. Both the sensor response and mixing times are considered using a first order approximation:

$$\dot{y}(t) \cdot \tau + y(t) = u(t) \tag{4.24}$$

To determine the gas transport and response times, a three-way valve was installed in various locations in the soot sampling train shown in figure 4.11 and used to generate step changes in the soot concentration. With the engine under steady-state operation, the three-valve was used to switch between sampling of exhaust and fresh air. By installing the three-way valve immediately prior to the inlet of the MSS, it was possible to determine its internal gas transport and response time from the resulting measured soot concentration history. Similarly the valve was mounted immediately after the outlet and prior to the inlet the FPS to determine the gas transport time from the FPS to the MSS, as well as a characteristic mixing timescale of the FPS itself.
If each of the parameters listed in figure 4.11 are determined using the method outlined above, the actual EC concentration can be determined from the measured signal, $[EC]_{meas}$ as follows:

$$[EC]_{act} = [\ddot{EC}]_{meas} \cdot \tau_{fps} \cdot \tau_{mss} + [\dot{EC}]_{meas} \cdot (\tau_{fps} + \tau_{mss}) + [EC]_{meas} \tag{4.25}$$

where each of the delay and response times are listed in table 4.4. These parameters were empirically determined such that the step change in soot

τ_{fps}	0.3 s
τ_{mss}	0.5 s
Δt_{fps}	1.5 s
Δt_{mss}	0.4 s
$\Delta t_{fps-mss}$	0.6 s

Table 4.4: Response (τ) and gas transport (Δt)times of the soot measurement train (see equation 4.25)
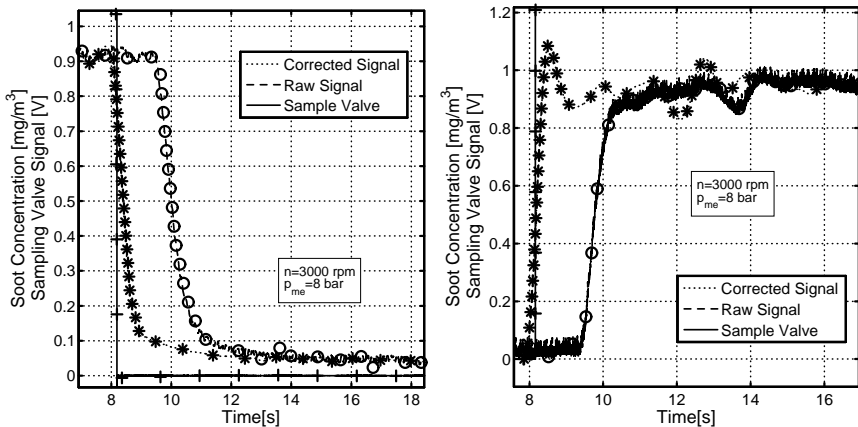
Figure 4.12: Comparison of the raw and corrected dynamic responses of the soot measurements system to a step decrease (left) and decrease (right) in the soot emissions. OM611, reference fuel.

concentration generated by the three-way valve was reproduced, without incurring excessive overshooting. A comparison of the raw measured signal and corrected signals is shown in figure 4.12 for step increase and decrease in the soot concentration (generated using the three-way valve).

4.5 In-Cylinder Soot Measurement

In addition to the exhaust stream measurements, the in-cylinder soot concentration (KL factor) and temperature were measured using miniature three color pyrometers. As shown in figure 4.2, pyrometers were installed in cylin-

ders one, three and four. Cylinder two was omitted due to an interference between the pyrometer and the fuel rail. The pyrometers were installed using glowplug adapters, thereby not requiring any additional accesses in the engine, though this also prevented the simultaneous pyrometry and cylinder pressure measurements (see section 4.6.

4.5.1   Implemented Pyrometers

The implemented pyrometers are the result of continuing joint project between Kistler AG Winterthur, the ETH Zurich, and Sensoptic AG [59]. The most notable features of the pyrometers are listed below and shown in figure 4.13.

- The small size ($\phi 6\,\text{mm}$) of the pyrometers facilitates their installation in production passenger car engines through the use of glow plug adapters, or in minimally invasive dedicated accesses in applications where a glow plug is not used.

- The window of the pyrometer can be maintained at temperatures up to 600°C using a regulated heater, thereby minimizing contamination of the pyrometer window through deposited particulate matter.

- Through the use of a lens, the sensor has a 140° field of view, which enables the sensor to record a large portion of soot in the combustion chamber.

- Though not exclusive to the pyrometers used in this investigation (see [110], for example), the light intensity is recorded at three wavelengths rather than the usual two. This allows the validity of the pyrometer calibration and the influences of the pyrometer installation or window contamination to be considered.

Recall that for a two-color pyrometer, the particle temperature is determined from an iterative solution of

$$\left(1 - \frac{\exp\left(\frac{C_2}{\lambda_1 T}\right) - 1}{\exp\left(\frac{C_2}{\lambda_1 T_{app,1}}\right) - 1}\right)^{\lambda_1^\alpha} = \left(1 - \frac{\exp\left(\frac{C_2}{\lambda_2 T}\right) - 1}{\exp\left(\frac{C_2}{\lambda_2 T_{app,2}}\right) - 1}\right)^{\lambda_2^\alpha} \tag{2.6}$$

where the apparent temperatures $T_{app,1}$ and $T_{app,2}$ are defined by the measured light intensities at λ_1 and λ_2. If the light intensity is instead recorded at three wavelengths, three particle temperatures can be determined - one from each wavelength combination (T_{λ_1,λ_2}, T_{λ_2,λ_3}, and T_{λ_1,λ_3}). Assuming the approximation for the emissivity of a soot cloud ϵ from [41] is valid, each of the
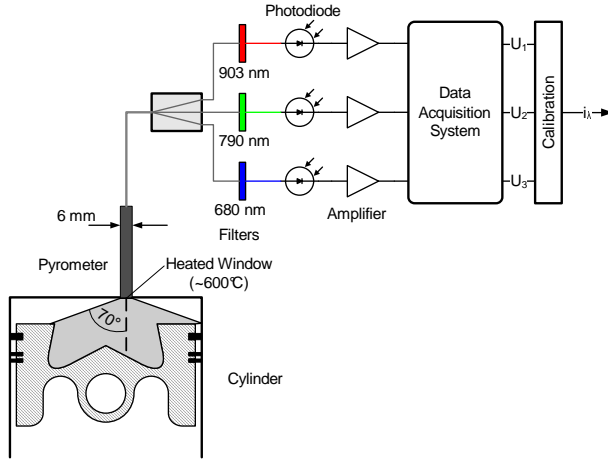
Figure 4.13: Overview of the implemented three color pyrometers. Adapted from [58].

three temperatures calculated using equation 2.6 should be the same. If this condition is not met, it is assumed that the calibration of the pyrometer (for the conversion of the recorded signal voltage to light intensity) is not valid, either due to contamination of the window, or because the field of view of the sensor is not the same as it was during the calibration.

An algorithm to correct the calibration was developed such that the difference between the three calculated particle temperatures T was minimized. In particular, the radiation intensity of the particle is proportional to the measured voltage as defined by the calibration[11]:

$$i_{\lambda_i} = \delta_{corr} \cdot a_1 U_{\lambda_i} + a_0 \qquad \delta_{corr} \in [0.95, 1.05] \qquad (4.26)$$

where a_1 is the proportional calibration constant and a_0 is the offset constant determined when the pyrometer has no incident radiation. The calibration correction is carried out by varying δ_{corr} such that all of the calculated particle temperatures (T_{λ_1,λ_2}, T_{λ_2,λ_3}, and T_{λ_1,λ_3}) agree, for as much of the recorded history as possible. As the raw signal intensity and hence the signal to noise ratio for a given wavelength is defined by T^4, only temperatures above 2000 K

---

[11]The calibration of the pyrometer follows using a calibrated integrating sphere, whose spectral radiation intensity is know. For each of the three considered wavelengths, the voltage output of the pyrometer is determined when exposed to the integrating sphere.

were considered during the calibration correction. The range of δ_{corr} was held relatively small, as the goal of the correction was to correct for minor differences in the temperatures, but not to change the base calibration. Finally, only the calibration of shortest wavelength (680 nm) was corrected, is has the lowest signal strength[12] and hence lowest signal to noise ratio.

From the three calculated temperatures, it is possible to calculate a total of six KL factors - two for each temperature, using each of the two wavelength considered for temperature determination (see equations 2.5 and 2.6).

4.5.2   Useful Parameters from Multi-Colour Pyrometry

As the pyrometers measure the in-cylinder particle concentration they provide several benefits over conventional exhaust stream measurements. Most notably, the provide the possibility to determine the cycle and cylinder-specific particulate emissions. Furthermore, it is possible to characterize the particulate formation and oxidation processes, rather than just the engine out soot emission. Using the representative KL factor history shown in figure, several relevant parameters are outlined below.

Estimation of Cycle Specific PM Emission

For the characterization of the soot emissions during transient operation, the ability to quantify the cylinder and cycle-specific soot emission is desirable. From previous investigations, it has been seen that the KL factor after the oxidation has finished $(KL)_{end}$ correlates well with the exhaust stream soot emissions characterized using FSN [58], [46], [47]. In figure 4.14 the relatively flat regime after approximately 400° CA represents the region in which the soot concentration is no longer changing as the temperature is too low for oxidation, yet the temperature is still high enough to produce sufficient radiation for detection with a pyrometer. The KL factor value in this region is defined as the $(KL)_{end}$ value.

The calculation of the KL factor history is stopped after the blackbody temperature falls below a prescribed value (~ 1300 K), as it was found that the signal quality with implemented pyrometers is no longer satisfactory below this temperature. Using this point as a basis, the $(KL)_{end}$ was determined as the KL factor value averaged over the 2° CA preceding this point [73]. This procedure allows the cylinder and cycle specific, cylinder-out emissions to be determined.

---

[12]For diesel relevant temperatures $i_{\lambda=680\,nm} < i_{\lambda=790\,nm} < i_{\lambda=903\,nm}$, from Planck's Law.
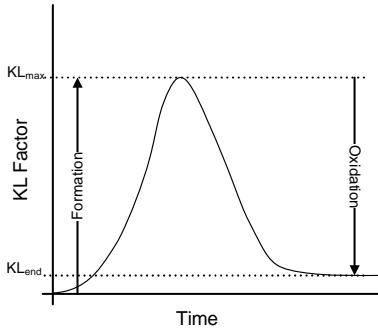
Figure 4.14: Representative KL factor history for a direct injection diesel engine

.

Characterizing the Particle Formation and Oxidation

In addition to cylinder-out soot emissions, the pyrometers were used to characterize the soot particle formation and oxidation processes. The soot formation was quantified using the maximum KL factor value, $(KL)_{max}$ while oxidized soot fraction, γ_{ox} was quantified as the ratio between the maximum and final KL factor values:

$$\gamma_{ox} = \frac{(KL)_{max}}{(KL)_{end}} \tag{4.27}$$

These values are only used to characterize the soot formation and oxidation qualitatively and not quantitatively as $(KL)_{max}$ represents the point at which the formation and oxidation are in equilibrium, as oxidation is already taking place before $(KL)_{max}$.

4.6 Rate of Heat Release Analysis

Though not available for the MVSM according to the goals of this investigation, a rate of heat release (ROHR) analysis was used for interpretation of the measurements. In particular the two zone thermodynamic analysis implemented in the software package WEG [76] was used. Given the engine geometry and configuration, operating conditions, and a measured cylinder pressure history, WEG provides among other things the rate of heat release

and fresh gas, burned gas, and mean gas temperatures, based on a classic two-zone analysis (see [38], for example).

For the ROHR the temporally resolved in-cylinder pressure is required. This was measured using an un-cooled, piezo-electric transducer (Kistler 6056A1) mounted in a glowplug adapter. So that the uncooled sensor is not affected by thermo shock induced by the flame ([85], [20]) it was set back from the combustion chamber wall. This introduces an additional volume a between the combustion chamber wall and the sensor, in which organ-pipe type fluctuations are generated and are superimposed onto the pressure signal [17]. When the measurements are averaged over several cycles for steady-state measurements, the effect of the fluctuations is minimized. During transient measurements, it is not possible to average multiple cycles and the fluctuations can influence the accuracy of the ROHR analysis. The use of the uncooled sensor, in a sub-optimal location was necessitated by the lack of a suitable instrumentation bore in the cylinder head.

4.6.1 Characteristic Mixing Time

In addition to the classic heat release analysis, a characteristic mixing time was also considered. The rate of the diffusion combustion process in a diesel engine is assumed to be limited by the mixing of the injected fuel with the available oxygen. Thus the diffusion combustion rate can be defined as [75]:

$$\frac{dm_f}{d\varphi}\bigg|_{diff} = \frac{1}{\tau_{char,exp}} \cdot m_{f,v} \tag{4.28}$$

where $\tau_{char,exp}$ is a mixing timescale characteristic for the diffusion combustion and $m_{f,v}$ is the fuel vapor mass available for diffusion combustion and is determined using the d^2 law (see equation 3.8). As $\frac{dm_f}{d\varphi}\big|_{diff}$ is known from the heat release analysis, and the available fuel mass is the fuel vapor which has not yet been consumed, the inverse characteristic mixing time $1/\tau_{char,exp}$ is defined as

$$\frac{1}{\tau_{char,exp}} = \frac{\frac{dm_f}{d\varphi}\big|_{diff}}{m_{f,v}} \tag{4.29}$$

It should be noted that $\tau_{char,ex}$ is measure of the effective, diffusion combustion relevant, mixing timescale inferred from a measured cylinder pressure history. This is in contrast to τ_{char}^* defined in equation 3.17, which estimates the mixing timescale based on the injection generated turbulence and piston motion.

4.7 Summary

Two engines operating with three different fuels were used to obtain steady state soot emission measurements for the validation of the MVSM. The soot emissions were measured using a Photo-Acoustic Soot Sensor (PASS) on the OM611, which enabled steady-state and transient measurements, though the dynamic behavior of the PASS required characterization. The steady-state soot emissions from engine two where determined using an FSN system and empirical correlation. For the transient measurements on the OM611, novel methods were devised to determine the EGR rate, intake charge temperature, and effective relative oxygen-fuel ratio. The EGR rate was determined using a fast mass spectrometer to measure the CO_2 concentration in the intake stream, and a lambda-sensor to estimate the CO_2 concentration in the exhaust stream. The intake charge temperature was determined using the ideal gas law and an empirical engine specific correction function. The relative oxygen-fuel ratio provides a measure of the total oxygen availability, including the influences of EGR, fuel quantity, and intake charge pressure.

Additionally, the in-cylinder soot concentration was measured in three of the four cylinders on the OM611 using miniature three-color pyrometers. By considering the radiation intensity at three wavelengths, rather than just two as is typically done, it is possible to evaluate the validity of the pyrometer's calibration. The pyrometry measurements were used to characterize the cylinder and cycle specific soot emissions ($(KL)_{end}$) , as well as to provide representative values for the soot formation ($(KL)_{max}$) and oxidation (γ_{ox}, equation 4.27). The measurements obtained using these techniques are presented along with a detailed analysis in the following chapter. The exhaust stream soot emissions are once again presented in chapter 6, where they are used for the parameterization and validation of the MVSM.

Chapter 5

Experimental Results and Analysis

5.1   Introduction

The measurements obtained using the methods outlined in chapter 4 are presented in this chapter, with the goal of elucidating the causes for the observed soot emission trends during steady-state and transient operation. In particular, the measurements from the OM611 are used to investigate the influence of:

- engine operating parameters during steady state operation;
- the fuel properties during steady state operation, and;
- transient engine operation on the soot emissions.

This requires the consideration of the standard engine operating parameters taken from the ECU, the measured exhaust-stream and in-cylinder soot concentrations, as well as the intake charge temperatures, EGR rates, relative oxygen-fuel ratio, and a thermodynamic analysis. Furthermore, the suitability of in-cylinder three-color pyrometry to measure the cylinder and cycle specific particle emissions is investigated. As a first step, the exhaust-stream soot concentrations and $(KL)_{end}$ values are compared. The resulting correlation is then subsequently used to described soot emission tendencies during steady state and transient operation. Finally, an evaluation of the repeatability of the soot measurements is presented.

R^2		Reference Fuel $(KL)_{end}$				Fuel Two $(KL)_{end}$			
		Cyl. 1	Cyl. 3	Cyl. 4	Total	Cyl. 1	Cyl. 3	Cyl. 4	Total
$(KL)_{end}$	Cyl. 1	–	0.63	0.76	0.98	–	–	–	–
	Cyl. 3	–	–	0.72	0.72	0.77	–	–	–
	Cyl. 4	–	–	–	0.86	0.66	0.63	–	–
	Total	–	–	–	–	0.97	0.80	0.81	–
	FSN	0.51	**0.89**	0.64	0.59	0.76	**0.87**	0.53	0.76
	MSS	0.46	0.87	0.58	0.54	0.73	0.83	0.51	0.73

Table 5.1: Summary of the correlations R^2 between pyrometry measurements ($(KL)_{end}$), FSN, and soot concentration measured using the MSS for operation with the reference fuel (left) and fuel two (right).

5.2 Correlation of Exhaust Stream and In-Cylinder Measurements

As it is desired, among other things, to use the in-cylinder pyrometry measurements for characterization of the cylinder and cycle specific soot emission, the correlation of the pyrometry measurements with the exhaust stream measurements was investigated under steady state operation. Of particular interest for the correlation with the exhaust stream measurements was $(KL)_{end}$ as already discussed in section 4.5.2.

For each of the steady-state operating points, the cylinder-specific $(KL)_{end}$ values were determined for operation with both fuels. Given in table 5.1 is a summary of the correlation coefficients between the $(KL)_{end}$ measurements from each of the three instrumented cylinders and the exhaust stream measurements (FSN and MSS). In addition, the cylinder-specific $(KL)_{end}$ values were also correlated with one another and the total $(KL)_{end}$ factor, which is defined as the sum of the $(KL)_{end}$ values from each cylinder. The total $(KL)_{end}$ factor is presented as this should consider the different contributions from each cylinder to the engine-out emission (as measured in the exhaust stream).

For both of the fuels, the best correlation with an exhaust stream measurement was seen between the $(KL)_{end}$ values from cylinder three and the FSN measurements and a slightly lesser correlation with the MSS measurements. That there is a better agreement between FSN and pyrometry can be explained
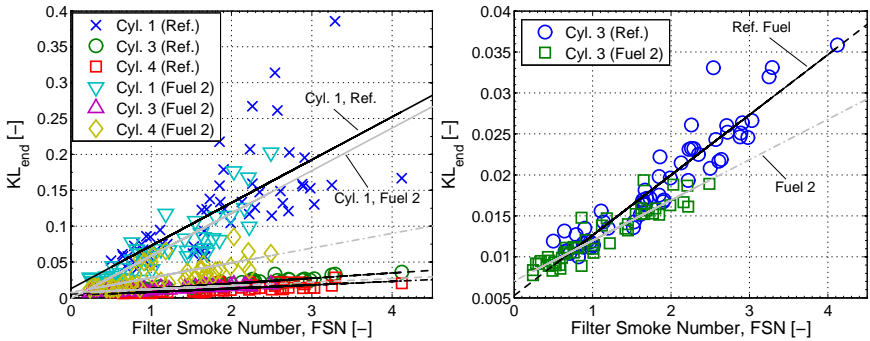
Figure 5.1: Comparison of the operating point and cylinder specific $(KL)_{end}$ factor values and exhaust stream FSN values for steady state operation with both fuels. The right hand figure shows only cylinder 3 and 4. OM611.
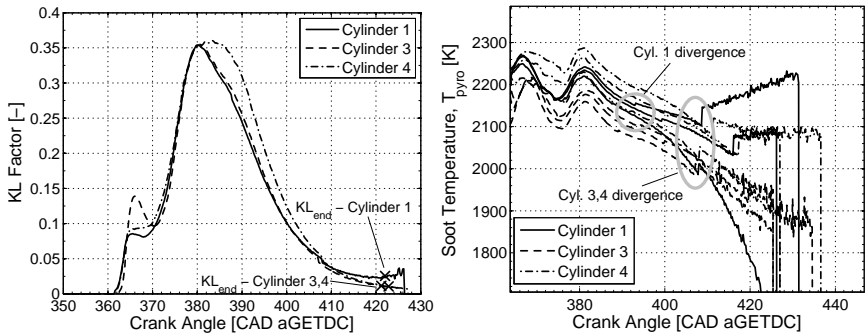
Figure 5.2: Comparison of the KL factor (left) and soot temperatures (right) in each cylinder to indicate the influence of temperature divergence on $(KL)_{end}$ determination. 3000 rpm, $BMEP = 8.0$ bar.

by the fact that both pyrometry ($(KL)_{end}$) and FSN are not elementary carbon specific, while the MSS is. A low signal-to-noise ratio has a considerable impact on the $(KL)_{end}$ determination and is thus explored in greater detail below.

For both fuels, a strong correlation exists between the total $(KL)_{end}$ values and those from cylinder one, while at the same time there is a relatively weak correlation with the exhaust stream measurements. This indicates that

the $(KL)_{end}$ values from cylinder one are considerably larger than those from cylinders three and four, as shown in the left hand side of figure 5.1. If only cylinders three and four are considered, as in the right hand side of figure 5.1, it is apparent that the magnitudes of the $(KL)_{end}$ values are similar, as is the correlation between $(KL)_{end}$ and FSN for both cylinders, with both fuels.
The higher $(KL)_{end}$ values in cylinder one are likely an artifact of an inadequate calibration, rather than an increased particulate emission. The left hand side of figure 5.2 shows a comparison of the KL histories for each cylinder, where it is apparent that KL in cylinder one increases towards the end of oxidation (after $\sim 415°$ CA), which is not expected. This increase in KL is described by the divergence of the three particle temperatures used to calculate KL , as shown in the right hand side of figure 5.2. The divergence of the temperature is believed to be caused by an invalid calibration[1] or low signal-to-noise ratios. As the temperatures diverge, so too does KL and can no longer be considered as being accurate. Thus, for cylinder one the $(KL)_{end}$ values are defined not by the end of oxidation, but rather by the point at which the measured temperatures diverge. As this happens prior to the end of oxidation, the $(KL)_{end}$ values for cylinder one are too high.
In general, cylinder three was seen to have the lowest divergence across all measurements and will be the only one considered for the remainder of this analysis. Based on the acceptable correlation between $(KL)_{end}$ and the exhaust stream measurements, $(KL)_{end}$ can be used as a parameter to characterize the cycle-specific particle emissions,

5.3   Steady State Operation

The soot emissions during steady operation were measured according to the procedure outlined in section 4.2.1 using the reference fuel and fuel two. Shown in figure 5.3 are the steady state soot emissions maps measured using the FPS/MSS system for both fuels. While the primary purpose of these measurements is to validate the MVSM, a discussion as to the causes of the general trends in the soot emissions follows.
Both fuels show a tendency to produce high soot emissions at approximately 2000 rpm and 7-8 bar $BMEP$. Through consideration of the reference fuel operating conditions maps, which are also representative of those for fuel two, this can be explained by a low oxygen availability in the combustion chamber.

---

[1]The validity of the calibration can be influenced by contamination of the window, or through an obstructed field of view.
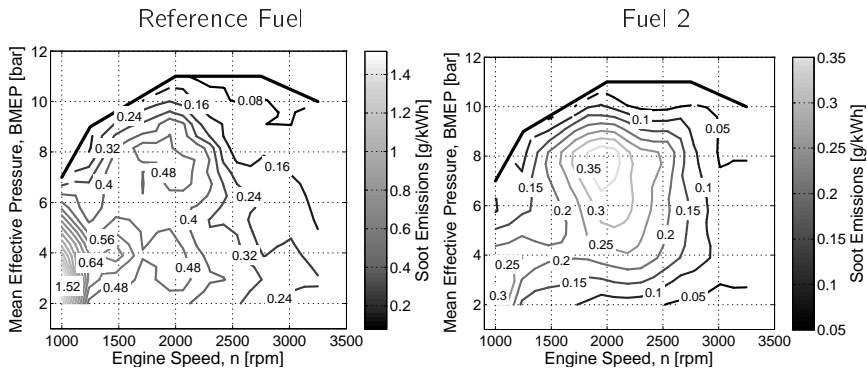
Figure 5.3: Measured steady state soot emissions maps for OM611 with reference fuel (left) and fuel 2 (right)
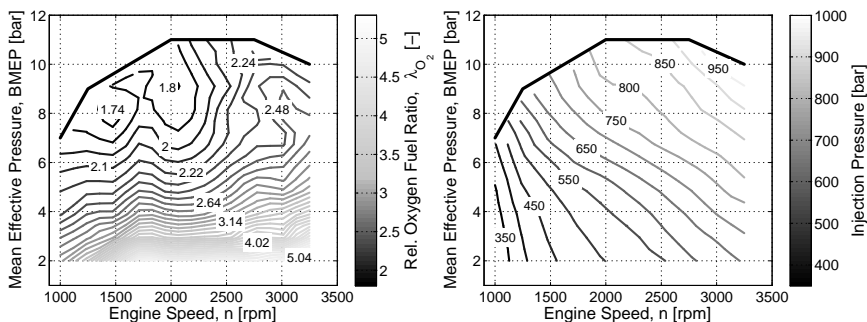
Figure 5.4: Relative oxygen-fuel ratio (left) and injection pressure (right) maps for OM611 steady state operation with reference fuel.

This is characterized by the low λ_{O_2} in this region, as shown in the left hand side of figure 5.4. The low oxygen availability is caused by high EGR rates and inhibits soot oxidation. Furthermore, for operation with the reference fuel, high soot emissions are seen in at low engine speeds ($\sim 1000\,\text{rpm}$) and loads ($< 5\,\text{bar } BMEP$). This is attributed to low injection pressures and hence low turbulent mixing in this region, as indicated in the right hand side of figure 5.4. In general, as the engine speed increases, the in-cylinder turbulence increases as a result of the higher mean piston speed and more importantly due to the higher injection pressures. The higher in-cylinder turbulence results
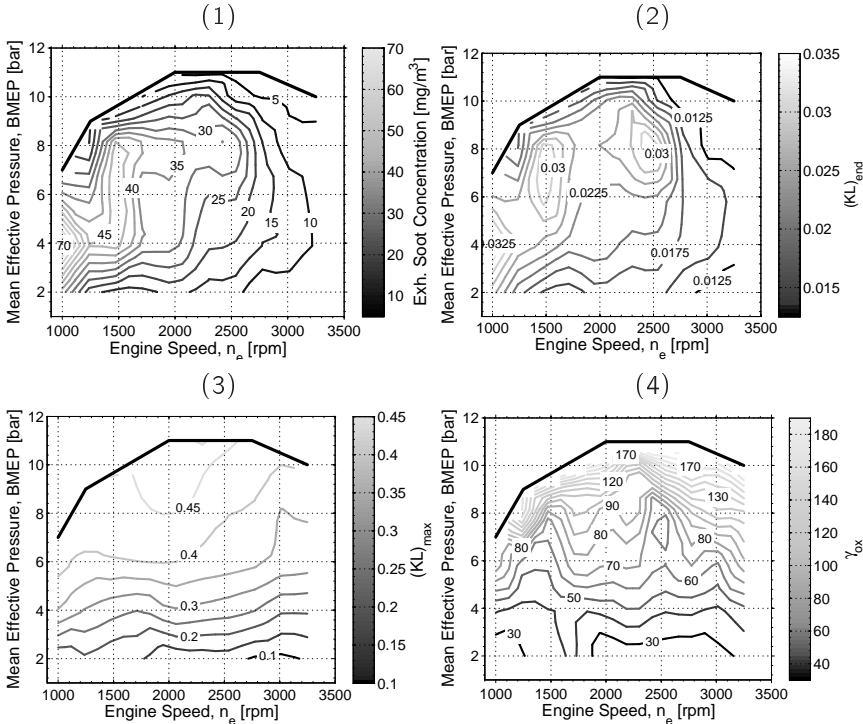
Figure 5.5: Exhaust stream soot concentration (1), cylinder out particle emissions (2), maximum in-cylinder KL factor(3), and particle oxidation factor γ_{ox} (4, see equation 4.27). OM611; reference fuel; KL parameters from cylinder three.

in enhanced oxidation rates and subsequently lower engine-out soot emissions. The above was only a brief consideration of the most relevant engine *global* engine operating parameters to describe the observed soot emissions tendencies. Further insight and support to these global observations can be obtained by considering the in-cylinder KL measurements. Shown in figure 5.5 are the exhaust-stream soot concentration (measured using the MSS) and the $(KL)_{end}$ maps, where a qualitative agreement between the two methods can be seen. Also shown are the $(KL)_{max}$ and γ_{ox} maps which can be used to characterize the particle formation and oxidation processes, respectively (see section 4.5.2). From the $(KL)_{max}$ map, it can be seen that the maximum

in-cylinder concentration is, as a first approximation, proportional to the engine load. This trend has also been observed on other engines as well [47]. In contrast, the γ_{ox} map indicates that the oxidation process is influenced much more by the engine operating parameters. Indeed, many of the regions of higher soot emissions (low speed and load; mid-speed, mid-load) coincide with regions of reduced soot oxidation. For example, in the region which λ_{O_2} was seen to be low, a reduced oxidation is evident, while there is no considerable change in the formation process. Similarly, in the low load and low speed region, a weak oxidation is noted but no significant feature can be seen in the formation in this region.

It should be noted that the KL parameters shown in figure 5.5 are based only on the cylinder three pyrometry measurements, and that there may be relevant contributions from the other cylinders.

5.3.1 Fuel Comparison

As can be noted from figure 5.3, the soot emissions are lower for operation with the second fuel, than with the reference fuel. If the soot emissions are directly compared for each operating point, as shown in figure 5.6, it can be seen that the soot emissions with fuel two were lower for all considered operating points. Depending on the operating point being considered, the soot emissions were significantly lower using fuel two. In regions of higher EGR rates (mid-load, mid-speed), the reduction in soot emissions afforded by fuel two is lower. From the fuel properties, it is expected that the lower soot emissions from fuel 2 may be caused by a more homogeneous combustion due the low cetane number and evaporation temperature, and its reduced aromatic content [94].

During the measurements with both of the fuels, the standard ECU was used and no adaptations were made for either of the fuels. Thus, with exception of intake air flow rate, the global engine operating parameters for the two fuels are not significantly different. Because of the lower density of fuel two, it was required to inject more fuel during operation with fuel two, than with the reference fuel. This was achieved by increasing the gas pedal position setting until the desired load was achieved, resulting in an increase in the intake air flow rate, by an average of 1.5%, as the ECU was operating under the assumption of a higher desired torque (dictated by the higher gas pedal position).

To understand the cause for the different soot emission levels from the two fuels, the in-cylinder processes were considered. In figures 5.7 through 5.10 a comparison of the heat release rate, in-cylinder temperatures, characteristic
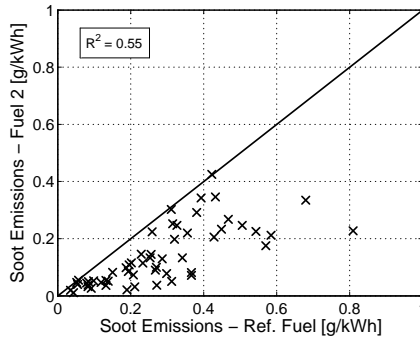
Figure 5.6: Operating point specific comparison of soot emissions for operation with the reference fuel and fuel 2 on the OM611.

mixing time, and KL factor histories for both fuels at four[2] different operating points is given. Also shown is the approximate timing of the fuel injection[3]. The difference in the soot emission for each operating point is quantified using:

$$\Delta m_s = \frac{m_{s,2} - m_{s,ref}}{m_{s,ref}} \tag{5.1}$$

From each of the parameters in figures 5.7 through 5.10 the following can be noted:

- The heat release rate for fuel two is marginally higher than for the reference fuel, a trend which has been seen more markedly elsewhere [95]. There, the increased heat release rate was attributed to the lower evaporation temperature of fuel two, resulting in more fuel being available for combustion sooner. Only in one of the four points (3000 rpm, 2 bar BMEP) is an increased premixed combustion fraction evident.

- The mixture temperature T_{mix}, determined using a thermodynamic analysis, was the same for both fuels prior to combustion. After combustion, T_{mix} is approximately 35 K lower with fuel two. This can be

---

[2]The four operating points were selected to include the reference point, one point in the center of the considered operating map, and two other points at the corresponding engine speeds and loads.

[3]The actual injection timing was estimated from the electrical signals from the ECU assuming a trapezoidal injection profile. The opening and closing times of the injector were assumed to be 0.3 ms and 0.2 ms, respectively, based on measurements of an injector of the same type.
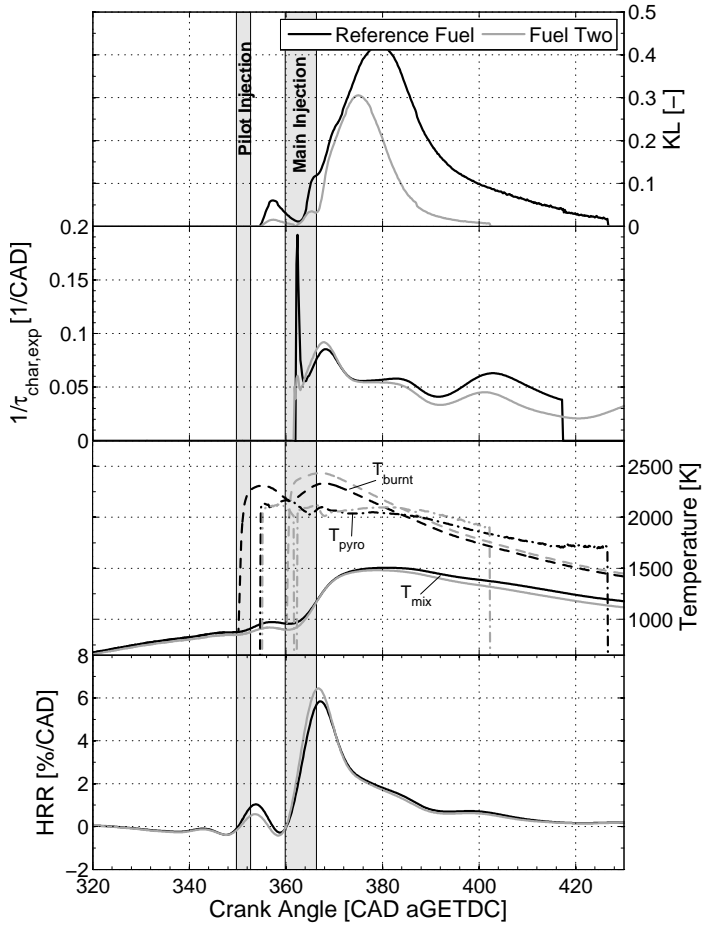
Figure 5.7: Comparison of the in-cylinder parameters for operation with the reference fuel and fuel two. T_{burnt} based on $\lambda = 1.0$; KL and T_{pyro} based on 790 nm and 903 nm radiation intensities; fuel injection timing estimated from ECU signals; average of 144 cycles. **1000 rpm, 6 bar BMEP, $\Delta m_s = -0.79$.**
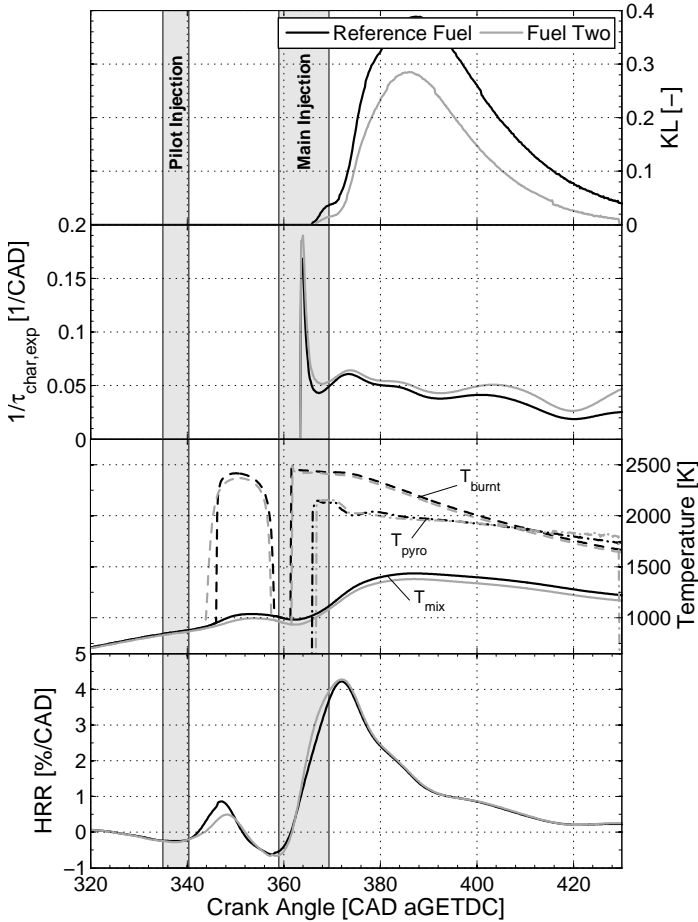
Figure 5.8: Comparison of the in-cylinder parameters for operation with the reference fuel and fuel two. T_{burnt} based on $\lambda = 1.0$; KL and T_{pyro} based on 790 nm and 903 nm radiation intensities; fuel injection timing estimated from ECU signals; average of 144 cycles. **2250 rpm, 6 bar BMEP,** $\Delta m_s = -0.34$.
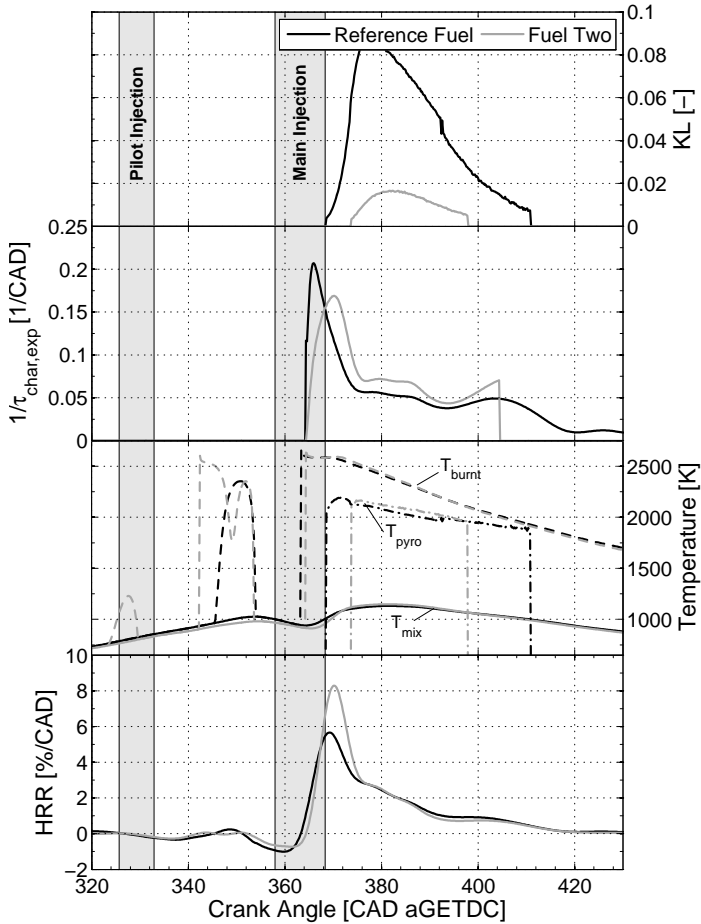
Figure 5.9: Comparison of the in-cylinder parameters for operation with the reference fuel and fuel two. T_{burnt} based on $\lambda = 1.0$; KL and T_{pyro} based on 790 nm and 903 nm radiation intensities; fuel injection timing estimated from ECU signals; average of 144 cycles. **3000 rpm, 2 bar BMEP** $\Delta m_s = -0.73$.
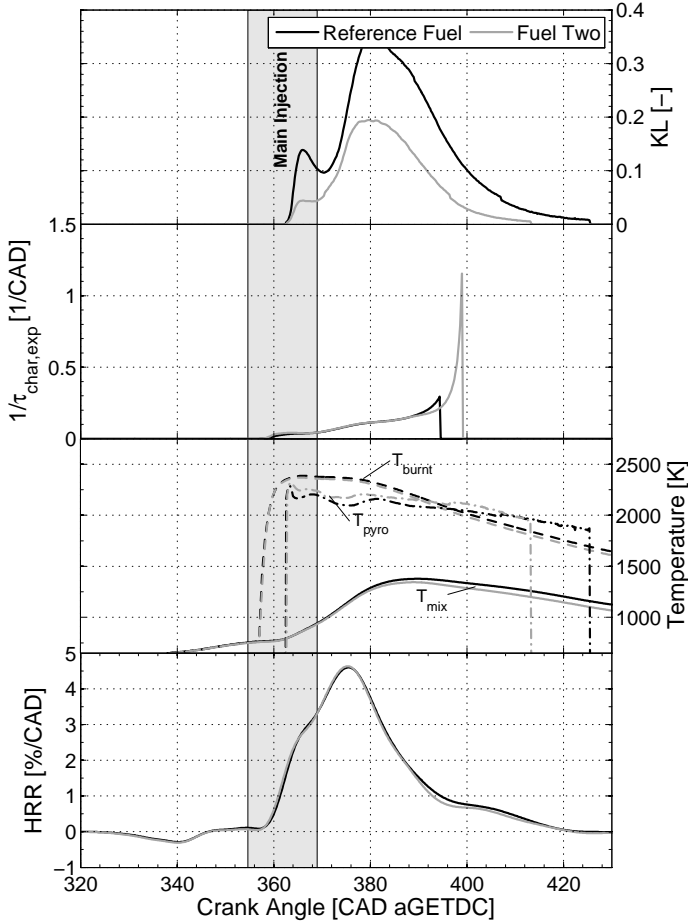
Figure 5.10: Comparison of the in-cylinder parameters for operation with the reference fuel and fuel two. T_{burnt} based on $\lambda = 1.0$; KL and T_{pyro} based on 790 nm and 903 nm radiation intensities; fuel injection timing estimated from ECU signals; average of 144 cycles. **3000 rpm, 8 bar BMEP, $\Delta m_s = -0.48$.**

attributed to the higher air, and hence diluent, mass in the combustion chamber for operation with fuel two.

- The burned zone temperature T_{burnt}, also determined using a thermo-dynamic analysis, was not significantly different for the two fuels. This is to be expected as the lower heating values of the fuels are not significantly different, and for the calculation of the burned gas zone, a relative air-fuel ratio of $\lambda = 1.0$ was assumed for both fuels.

- The particle temperature measured using pyrometery[4] T_{pyro} is similar to T_{burnt}, which is expected as the particles are assumed to formed in the direct vicinity of the flame. Again there does not appear to be a significant difference between the two fuels.

- Similar to the heat release rates, the inverse characteristic mixing times $1/\tau_{char,exp}$ are very similar between the two fuels, with fuel two perhaps having a slightly higher mixing rate. This would again be attributed to the lower evaporation temperature resulting in fuel being available for combustion faster. It should be noted that the uncertainty in τ_{char} is relatively high when there are low fuel conversion rates, or low fuel masses - i.e. at the beginning and end of combustion (see equation 4.29).

- In contrast to the combustion relevant parameters, the KL histories for the two fuels were seen to be considerably different, with that of fuel two being consistently lower. This indicates that the lower soot emissions with fuel two are not a result of an altered combustion process, but rather differing soot formation and oxidation processes. This is explored in further detail below.

That the KL factor for operation with fuel two was consistently lower, indicates fuel two's lower propensity to soot formation. Additionally, it should be noted that the net soot formation and oxidation rates[5] are approximately similar for both fuels. If it is assumed that after the first PAH are formed, the formation rate is largely defined by the HACA rate, which is approximately constant for different fuels [60], this is to be expected. It should be noted that while the net formation rate is the same for both fuels, the lower peak KL factor

---

[4]Recall that the pyrometry measurements are taken from a different measurement campaign than the pressure based parameters, as it was not possible to install both a pressure transducer and pyrometer in the same cylinder simultaneously.

[5]The net formation rate can be taken as the slope of the increase of the KL factor, while the oxidation rate as the slope of the decrease after the maximum.
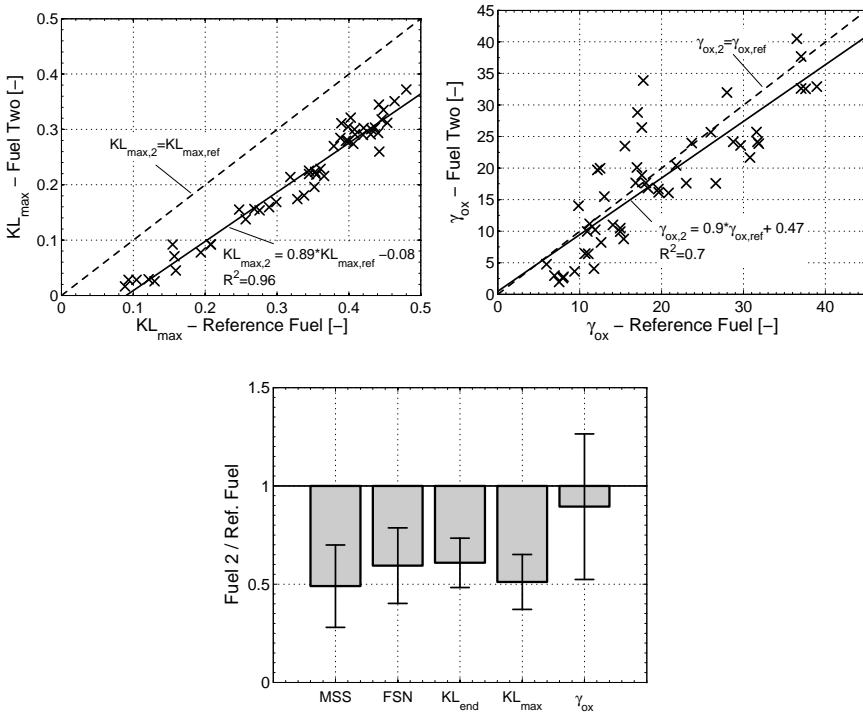
Figure 5.11: Direct comparison of operating point specific $(KL)_{max}$ (upper left) and γ_{ox} (upper right) values for steady-state operation with both fuels. Relative change in exhaust stream and in-cylinder emissions caused by using fuel two (bottom) - solid bars indicate the mean ratio over the entire map; error bars indicate the standard deviation. $(KL)_{max}$ values are taken from cylinder three and the 790 nm and 903 nm radiation signals.

seen with fuel two can be attributed to the lower aromatic fraction of the fuel. Because fuel two has a lower aromatic content, the first PAHs must be formed directly from the fuel molecules, illustrated by the lower KL factor values at approximately 370°CA. After the first PAHs are formed the surface growth by HACA is responsible for the increase in KL. The short term drop in KL immediately after the end of injection is attributed to a short term increase in the oxygen availability in the reaction zone and has been noted by others [89]. While a decrease in soot formation was seen to cause the soot emissions

reduction at the reference point for operation with fuel two, it is necessary to investigate whether this holds true for all measured operating points. Thus $(KL)_{max}$ and γ_{ox} were considered for all operating points, as shown in figure 5.11. In the left hand figure, it is evident that $(KL)_{max}$ is generally lower with fuel two, than with the reference fuel, indicating that less soot is formed. When the oxidation process is quantified using γ_{ox} it is seen that there is no concrete difference in the oxidation behavior between the two fuels. In the lower portion of figure 5.11 is a comparison of the exhaust stream (MSS and FSN) and in-cylinder soot measurements. The solid bars indicate the mean change in soot emissions ($\frac{m_{s,2}}{m_{s,ref}}$) over all considered operating points for each measurement system, while the error bars indicate the standard deviation. The MSS, FSN, $(KL)_{end}$, and $(KL)_{max}$ all show similar reductions in the soot emissions, while no consistent reduction can be seen in the oxidation (γ_{ox}). This supports the hypotheses that the lower soot emissions result from a reduced formation.

5.4 Engine Two

Additional steady state measurements from engine two were delivered from a project partner for additional validation of the MVSM. As already discussed, two sets of measurements were available: standard operation in which the engine parameters were defined according to the ECU; and parameter variations, during which the engine parameters were prescribed.

Shown in the left side of figure 5.12 is the steady state soot emissions map. Similar to the OM611 measurements, a region of higher soot emissions seen around 2250 rpm and $BMEP = 8$ bar. In addition to this region, at lower engine speeds (<2000 rpm) along the full load limit, the soot emissions are also elevated. This is likely due to an oxygen deficit ($\lambda \approx 1.1$) and relatively low in-cylinder turbulence caused by low piston velocities and injection pressures.

The soot emissions during the parameter variations, outlined in section 4.2.2, are shown in the right side of figure 5.12. Five operating points with extremely high soot emissions (>1 g/kWh) are apparent, all at 2000 rpm and $BMEP = 6$ bar, and with 40% EGR. All other operating points at this engine speed and load have between 0 and 30% EGR, with the increase in EGR to 40% causing the increase in soot emissions. In order to achieve 40% EGR, the intake charge pressure was decreased approximately 3% through throttling. The decrease in oxygen availability in the combustion chamber through the decreased intake charge pressure and increased EGR fraction result in the drastic increase in soot emissions. It should be noted that this region (~ 2000 rpm and $BMEP \approx$
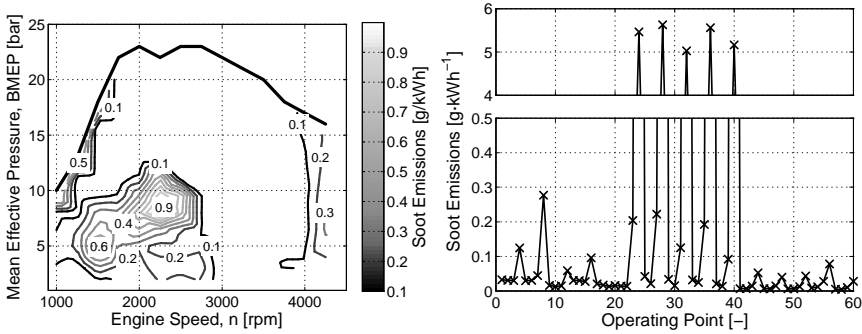
Figure 5.12: Measured steady state soot emissions map (left) and soot emissions for prescribed parameter variations (right). Engine two, fuel three.

6 bar) was noted to have elevated soot emission for both of the considered engines during standard ECU operation[6]. The operating points with extremely high soot emissions were included in this investigation for the primary purpose of investigating the ability of the MVSM to reproduce soot emissions under extreme operation.

5.5   Transient Operation

As with all the measurements presented in this work, the primary purpose of the transient measurements is for the validation of the MVSM. However, not much is known with regard to the influence of transient operation on soot emissions, in particular what happens within the combustion chamber. Thus, not only are the soot emissions during transient operation discussed, but also a detailed discussion of two relevant parameters is presented: the mean charge temperature and the relative oxygen-fuel ratio. Furthermore, the soot emissions during the transients are discussed not only in terms of exhaust stream measurements, but also in-cylinder measurements.

To quantify the influence of transient operation on the soot emissions and engine operating parameters, a Quasi-Steady-State (QSS) approximation is

---

[6]Standard ECU operation refers to operation of the engine using a production ECU. Naturally, this region of elevated soot emissions could be removed by decreasing the EGR rate or increasing the injection pressure, which would result in an increase in the NOx emissions.

used. Based on the engine speed and load measured during the transient, the QSS approximation interpolates a corresponding steady state value from the steady state parameter map [36]. For example, to compare the measured transient soot emissions with the corresponding steady-state soot emissions, the soot emissions are interpolated from the steady state measurements (see figure 5.3) based on the measured engine speed and load, at each time step during the transient. This implies then, that

$$m_{s,QSS} = f(\omega, BMEP) \tag{5.2}$$

where $m_{s,qss}$ is the estimated quasi steady state soot emission. The QSS approximation only considers the influences of the speed and load on the soot emissions but not other relevant parameters such as mean charge temperature or oxygen availability. The QSS approximation is naturally also applicable to other parameters and not just the soot emissions.

5.5.1 Exhaust Stream Soot Emissions

The soot emission behavior during transient operation is strongly dependent on the type of the transient being considered. The measured transient and steady state soot emissions during first and third gear acceleration transients are shown in figure 5.13. So that the different duration transients can be directly compared, they are shown using abscissa in engine speed rather than time. While there is no substantial difference between the steady state soot emissions (QSS) and the transient emissions, it should be noted that there is a high variability from one repetition of the transient measurement to the next (as denoted by the large shaded areas). The second gear acceleration is not considered as no repeatable results were obtainable, largely due to EGR valve fluctuations.

When the tip-in transients shown in figure 5.14 are considered, a substantial increase in the soot emissions is seen compared to steady state operation. This is particularly evident for the 1250 rpm measurements, where the soot emissions can be seen to increase approximately fourfold in the case of the 0.5 s transient. In general, the increase in soot emissions was seen to increase with decreasing transient duration, and was less evident at the higher engine speed. Similar to the acceleration transients, a large variability of up to $\pm50\%$ in the soot emissions was seen from one repetition of the transient to the next. To understand the cause for the increase in the soot emissions, in particular during fast transients at low engine speeds, the intake charge temperature and
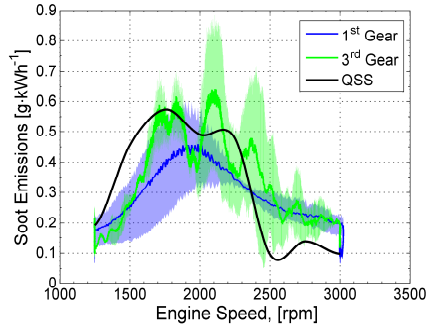
Figure 5.13: Comparison of the exhaust stream soot emissions measured during **acceleration** transients of different durations. Lines indicate the mean of the five measurement repetitions for each duration, while the shaded areas are bounded by the maximum and minimum measured soot emissions. OM611 with reference fuel.
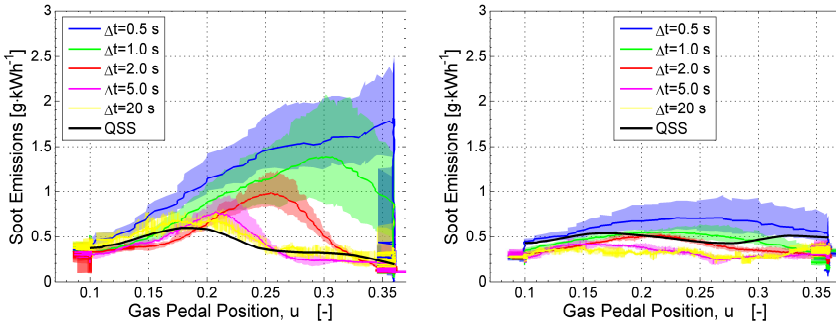
Figure 5.14: Measured exhaust stream soot emissions during **tip-in** transients of different durations at 1250 rpm (left) and 2000 rpm (right). Lines indicate the mean of the five measurement repetitions for each duration, while the shaded areas are bounded by the maximum and minimum measured soot emissions. OM611 with reference fuel.
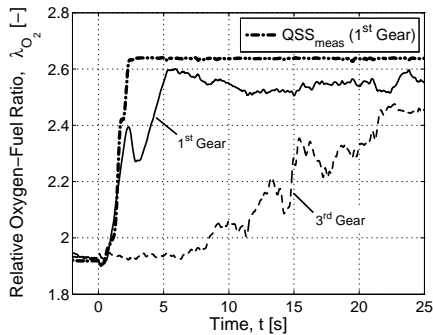
Figure 5.15: Relative oxygen fuel ratio for **acceleration** transients of different durations. OM611 with reference fuel.

oxygen availability are discussed below, followed by an investigation of the heat release rates and in-cylinder KL factors.

5.5.2 Relative Oxygen-Fuel Ratio

As introduced in section 4.3.3, the relative oxygen-fuel ratio was used to quantify the oxygen mass in the combustion chamber - through consideration of both the EGR rate and inducted fresh air. Shown in figure 5.15 is a comparison of λ_{O_2} during the acceleration transients and steady state operation (QSS) as a function of time. The QSS approximation for λ_{O_2} is only shown for the fastest transient, as this is assumed to be the most critical. During both transients, λ_{O_2} is seen to increase to the final steady state value, albeit with a delay compared to the QSS approximation. This delay is caused primarily by a slow increase in charge pressure (see section A.5 for charge pressure histories). The local λ_{O_2} maximum at 2 s during the first gear acceleration is attributed to an adjustment in the turbine geometry by the ECU. Although the transient values of λ_{O_2} are consistently lower than the QSS values, the soot emissions are not influenced, as λ_{O_2} does not drop into its critical region, which is discussed in detail below.

When the tip-in transients are considered however, λ_{O_2} was seen to drop below the QSS value for a short period of time, as is seen figure 5.16. This drop below the QSS value is attributed to a rapid increase in the injected fuel mass (no difference compared to QSS) while the charge pressure is still low and the
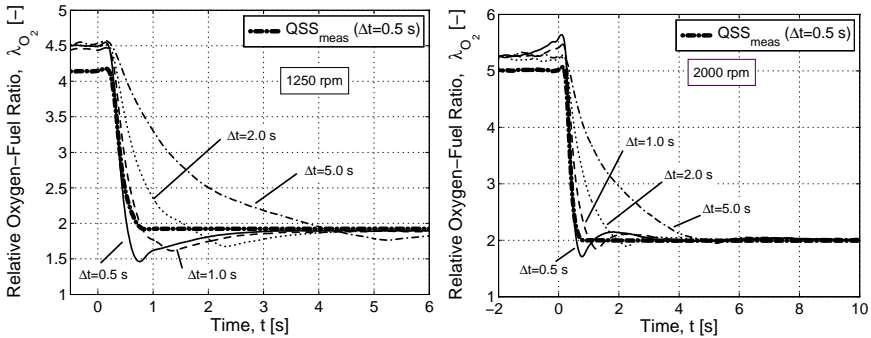
Figure 5.16: Relative oxygen-fuel ratio λ_{O_2} for **tip-in** transients of different durations at 1250 rpm (left) and 2000 rpm (right). OM611 with reference fuel.

EGR is still high. Once the charge pressure and EGR rates approach their steady state values, so too does λ_{O_2}. In an ideal system[7] soot is only of concern when the λ_{O_2} drops below unity. As the highly heterogenous nature of diesel combustion cannot be considered ideal, the limit for soot formation and incomplete combustion is not necessarily defined by $\lambda_{O_2} = 1.0$, but rather some higher value. This can be clearly seen in modern engines, where even at full load $\lambda > 1.0$ though there are still significant soot emissions. The critical limit for soot production is not only a function of the engine design, but also its operation. At 1250 rpm, it is seen that when λ_{O_2} drops below ~ 1.5 the soot emissions increase drastically. At 2000 rpm λ_{O_2} does not drop as low primarily due to the overall higher charge pressures and faster response of the turbocharger. Additionally, the higher in-cylinder turbulence caused by the higher mean piston velocity and injection pressures will further lower the critical value of λ_{O_2} [93]. Thus the increase in the soot emissions, particularly during the 1250 rpm tip-in transients is attributed to a short term oxygen deficit, characterized by λ_{O_2} undershooting its QSS value and entering into its critical range.

---

[7]An ideal system would be one in which all oxygen would be available for combustion, and a stoichiometric amount of oxygen would imply complete oxidation of the fuel to CO_2 and H_2O.
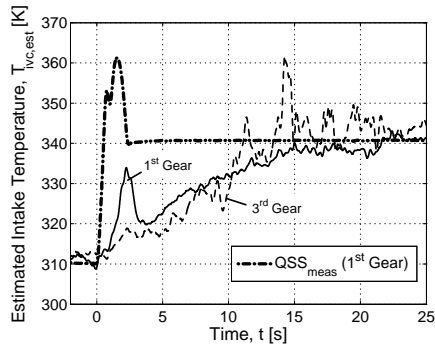
Figure 5.17: Estimated charge temperature at IVC for **acceleration** transients of different durations. OM611 with reference fuel.

5.5.3 Mean Cylinder Temperature at IVC

From the $\Phi - T$ map presented by [3] (see figure 2.6), it becomes obvious that the temperature also plays a strong role in the soot emissions. As introduced in section 4.3.2, $T_{ivc,est}$ is used to describe the mean gas temperature in the intake runner at intake valve closing. In general, for soot formation temperatures below $\sim 1900\,K$, a reduction in the temperature results in a decrease in the soot emissions, while at temperatures above $\sim 1900\,K$ a decrease in temperature results in an increase in the soot emissions. As the majority of the operating points under consideration are at part load, it is assumed that the former holds true, and that a decrease in the temperature results in a decrease in the soot emissions. This assumption is revisited below.

During the acceleration transients, $T_{ivc,est}$ remains below its corresponding QSS values for both transient durations, as shown in figure 5.17. After approximately 15 s $T_{ivc,est}$ reaches the steady state value, *independent* of the transient duration. This indicates that the rate at which the temperature increases is limited not by the transient duration but may rather be defined by the thermal behavior of the engine. The local maximum at approximately 2 s during the first gear transient is caused by the engine passing through a region, where a higher temperature is also observed during steady state operation (in the region of 2000-2500 rpm and $BMEP = 8.0$ bar, see figure 5.4) due to high EGR temperatures (see section A.4).

The charge temperatures during the tip-in transients were seen to decrease, as shown in figure 5.18. For both engine speeds, the decrease in temperature
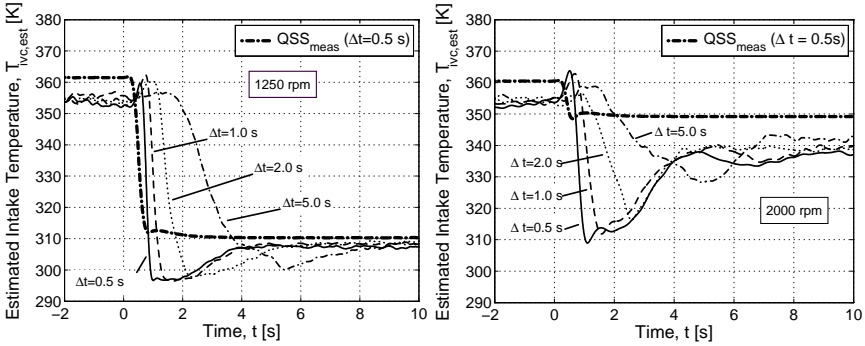
Figure 5.18: Estimated charge temperature at IVC for **tip-in** transients of different durations at 1250 rpm (left) and 2000 rpm (right). OM611 with reference fuel.

is nearly instantaneous and primarily caused by the reduction of EGR. Immediately after the transient $T_{ivc,est}$ is below the QSS value and slowly increases to its steady state value at a rate of *roughly* 4 K/s, regardless of the engine speed or transient duration. This once again indicates that the rate at which the temperature increases may well be defined by the thermal characteristics of the engine (e.g. effective heat capacity of the engine) and vary for different engines, and engine types. A thorough investigation of this, however, is outside the scope of this work.

From the assumption stated above, that a decrease in the temperature would result in a decrease in the soot emissions, it is expected that the soot emissions after the transient should be lower than in the steady-state case. As figure 5.19 shows for a representative tip-in transient at 2000 rpm, this is indeed the case. The lower soot emissions following the transient are attributed to the lower temperature which may influence the soot emissions through two mechanisms:

1. As shown in the $\Phi - T$ map [3] a decrease in the temperature results in a lower soot yield as a result of a decreased soot formation rate. As the $\Phi - T$ map was generated using a zero-dimensional chemical kinetic simulation, it only describes the chemical kinetic aspects of the soot formation, and does not account for the complexities of diesel combustion(see 2.4.1). In particular, the influences of fuel evaporation, turbulence and mixture inhomogeneity cannot be captured or described by such a map.
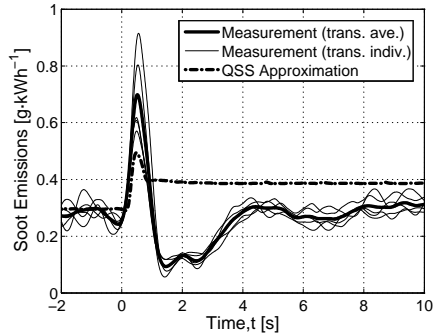
Figure 5.19: Comparison of the measured transient soot emissions with the QSS approximation. Tip-in transient, 2000 rpm, $\Delta t = 0.5$ s, OM611, reference fuel.

2. A change in the intake charge temperature influences the combustion process through changes in the gas temperatures, ignition delay, premixed combustion fraction, and naturally the soot formation and oxidation rates.

To further consider the latter point, a combustion analysis was carried out for the fastest tip-in transients at each of the investigated engine speeds.

5.5.4   Fuel Conversion Rate

To understand the influence of the transient operation on the combustion process, an analysis of the fuel conversion rates was carried out. As an overview, figures 5.20 and 5.21 show the fuel conversion rate iso-contours as a function of crank angle (y-axis) for each combustion cycle (x-axis) before, during, and after the transients at 1250 rpm and 2000 rpm, respectively. As expected, the fuel conversion rate histories are do not fluctuate much before and after the transient. During the transient, however, some changes in the fuel conversion rate are evident. In particular, there is a short-term increase in the maximum fuel conversion rate (at approximately 370 and 372 CAD for the 1250 rpm and 2000 rpm transients, respectively). In the final quarter and immediately following the transient, the maximum fuel conversion rate decreases and only recovers approximately 10 cycles after the transient. This phenomena is observed for both engine speeds, though not as prevalent
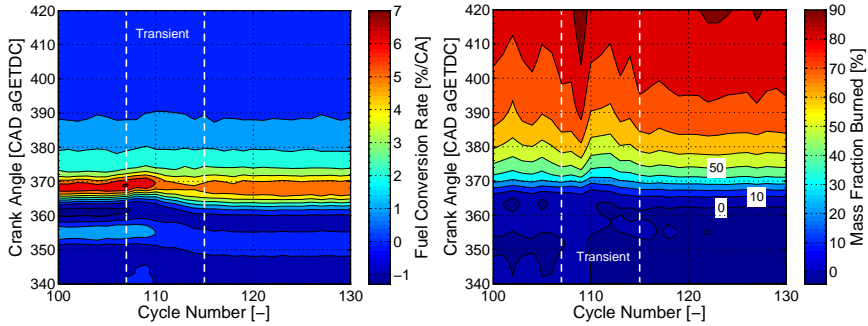
Figure 5.20: Fuel conversion rate (left) and mass fraction burned (right) during a 0.5 s tip-in transient at **1250 rpm**. OM611, reference fuel.

at 2000 rpm. The reduction in the maximum fuel conversion rate is approximately concurrent with the oxygen deficit characterized by λ_{O_2} (see figure 5.16), whereby it should be noted that λ_{O_2} is a measure of the global oxygen concentration and not necessarily the local concentration relevant for the combustion. Should the local air-fuel ratio become rich, the fuel conversion rate will decrease as more time is required for oxygen to become available for combustion through diffusion. Thus, the reduced fuel conversion rates observed at the end of the transients are attributed to a localized oxygen deficits inhibiting the combustion.

The reduced combustion rate can be further observed in the right hand sides of figures 5.20 and 5.21, where the mass fraction burned profiles are shown. In particular for the tip-in at 1250 rpm, a delay in the fuel conversion is noted. That this influence is more obvious at the lower engine speed, can be explained by the lower charge pressures and hence relative air-fuel ratios. At 2000 rpm, there is more oxygen available and the local oxygen availability does not enter a critical regime as during the 1250 rpm transient.

To gain a deeper understanding of the influences of transient operation on the combustion process, the transient fuel conversion rates are compared with the corresponding steady state histories below.

Comparison with Steady State Operation

Shown in figures 5.22 through 5.25 are comparisons of the heat release rates and mass fraction burned histories during transient and steady state operation,
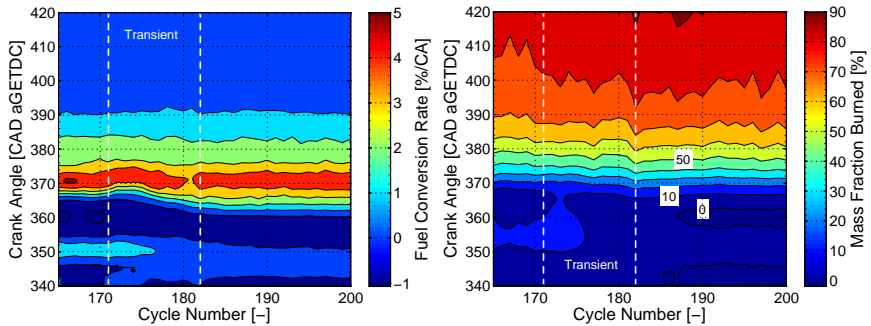
Figure 5.21: Fuel conversion rate (left) and mass fraction burned (right) during a 0.5 s tip-in transient at **2000 rpm**. OM611, reference fuel.

for 0.5 s tip-in transients at 1250 rpm and 2000 rpm. For both transients, two general phenomena can be identified:

1. At the beginning of the transient, there is an increase in the maximum fuel conversion rate, compared to steady-state operation. During transient operation, the injection pressure can be increased very rapidly, while the charge pressure (and hence cylinder pressure during injection) increases more slowly. This increased injection-cylinder pressure ratio results in increased injection velocities and turbulence in the combustion chamber and, thus, higher fuel conversion rates[8].

2. Towards the end of the transient there is a reduction in the maximum fuel conversion rate. As mentioned above, this decrease in the maximum heat release rate is attributed to an oxygen deficit limiting the combustion rate. The reduction in the maximum heat release rate is 18% and 14% for the 1250 rpm and 2000 rpm transients, respectively. After the charge pressure and EGR rate have reached their respective post-transient values, the maximum fuel conversion rate is not significantly different from the steady-state case.

---

[8]It should be noted that other researchers have also noted that this rapid increase in fuel injection pressure, without a corresponding increase in cylinder pressure, can result in longer spray penetration lengths and increased wall impingement.

1250 rpm, 2 bar BMEP, cycle 105

1250 rpm, 3 bar BMEP, cycle 108

1250 rpm, 4 bar BMEP, cycle 110

1250 rpm, 5 bar BMEP, cycle 111

1250 rpm, 6 bar BMEP, cycle 112

1250 rpm, 7 bar BMEP, cycle 114

1250 rpm, 8 bar BMEP, cycles 115, 117, 120, 130
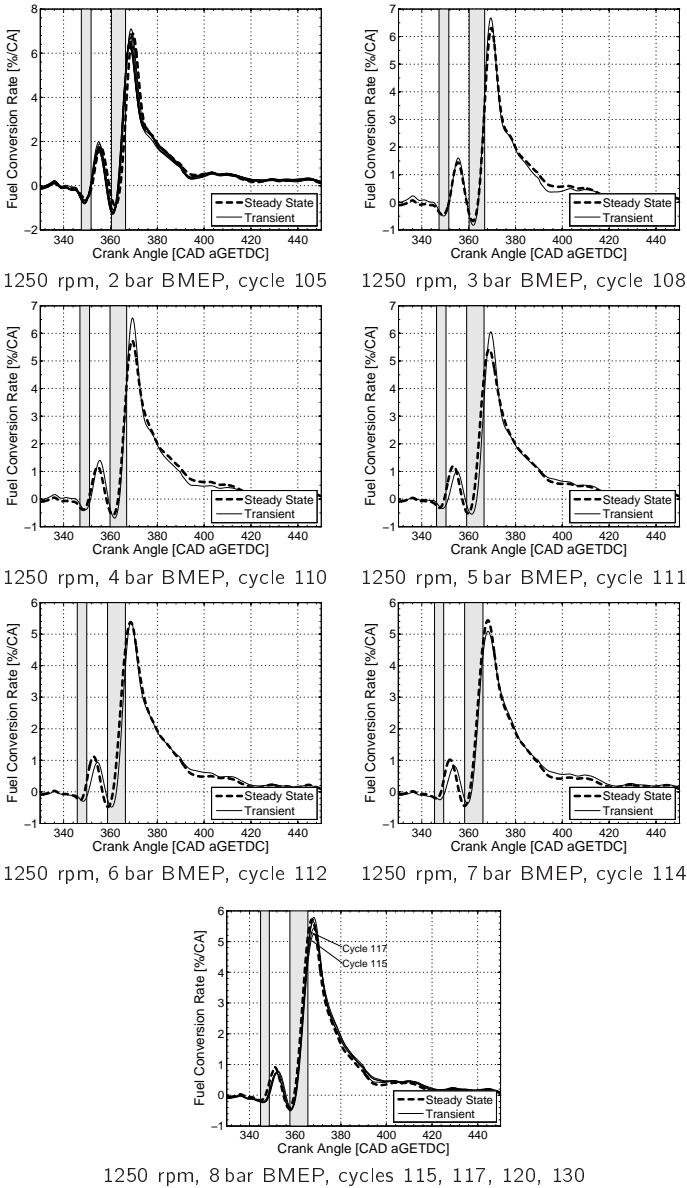
Figure 5.22: Comparison of steady state and transient fuel conversion rates during a 0.5 s tip-in transient at **1250 rpm**. Shaded regions correspond to injection events. OM611, reference fuel.
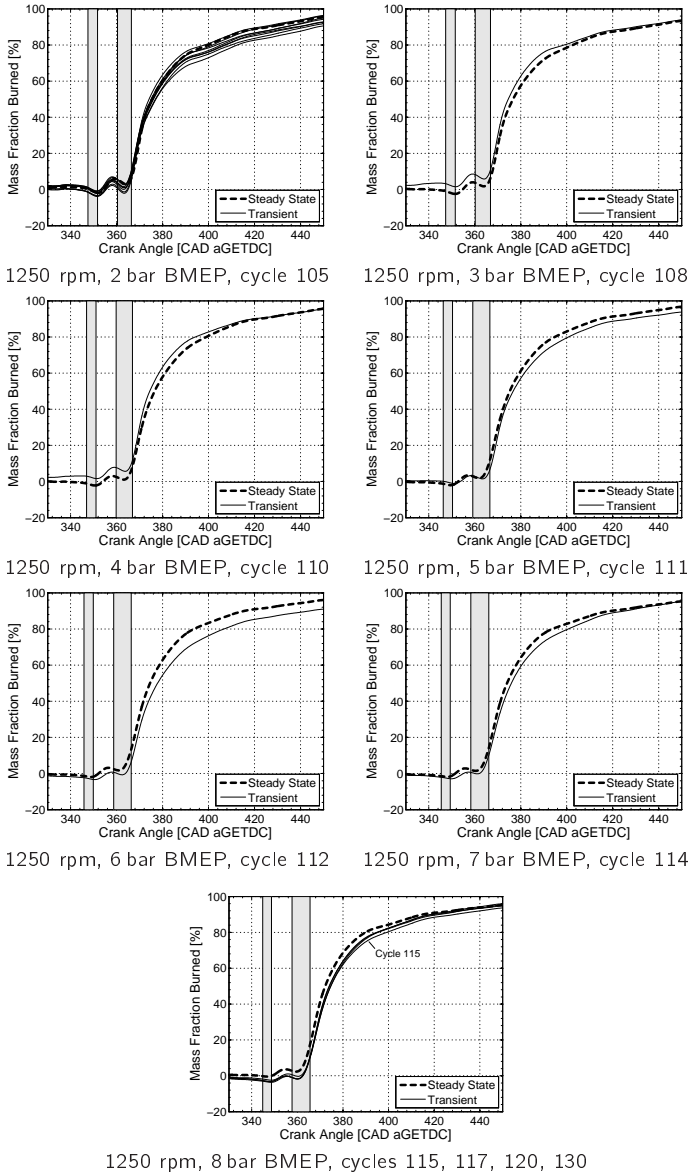
Figure 5.23: Comparison of steady state and transient mass fraction burned histories during a 0.5 s tip-in transient at **1250 rpm**. Shaded regions correspond to injection events. OM611, reference fuel

2000 rpm, 2 bar BMEP, cycles 165-170

2000 rpm, 3 bar BMEP, cycle 172

2000 rpm, 4 bar BMEP, cycle 174

2000 rpm, 5 bar BMEP, cycle 176

2000 rpm, 6 bar BMEP, cycle 177

2000 rpm, 7 bar BMEP, cycle 179

2000 rpm, 8 bar BMEP, cycles 181, 185, 190, 200, 215, 230
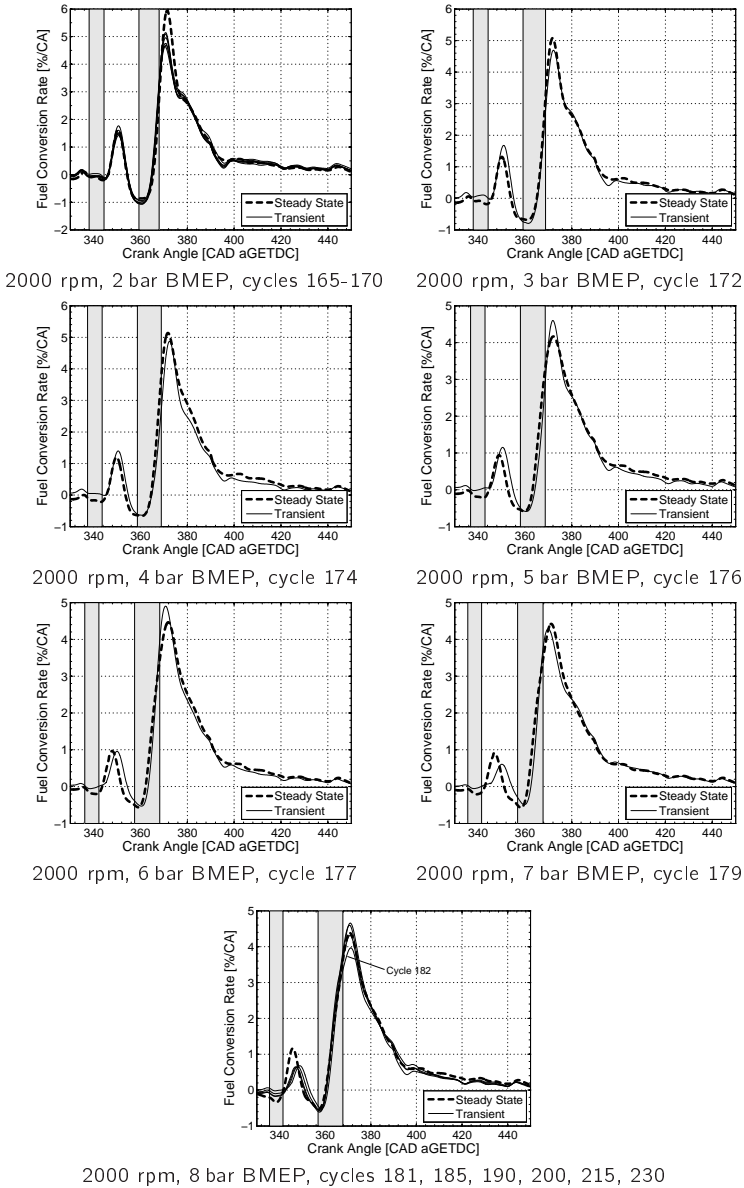
Figure 5.24: Comparison of steady state and transient fuel conversion rates during a 0.5 s tip-in transient at **2000 rpm**. Shaded regions correspond to injection events. OM611, reference fuel.
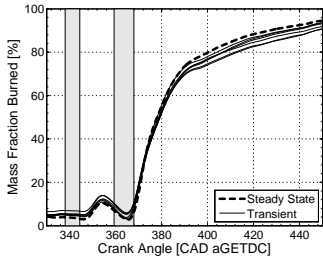
2000 rpm, 2 bar BMEP, cycles 165-170
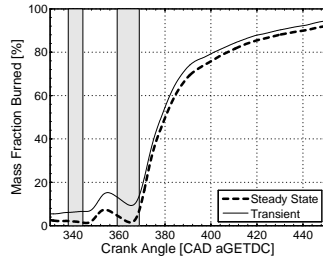
2000 rpm, 3 bar BMEP, cycle 172
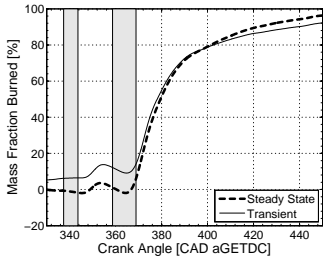
2000 rpm, 4 bar BMEP, cycle 174
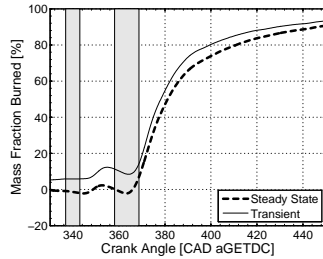
2000 rpm, 5 bar BMEP, cycle 176
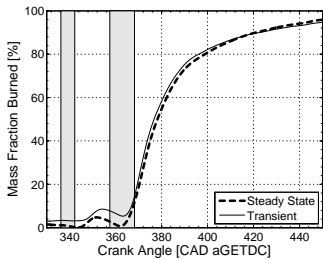
2000 rpm, 6 bar BMEP, cycle 177
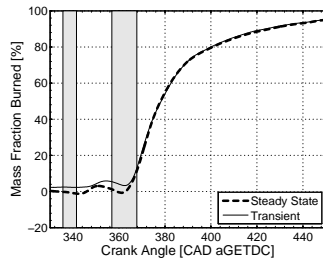
2000 rpm, 7 bar BMEP, cycle 179
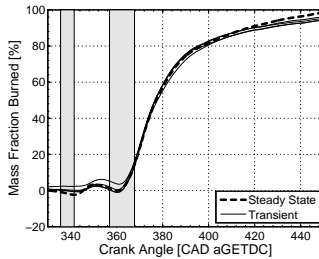
2000 rpm, 8 bar BMEP, cycles 181, 185, 190, 200, 215, 230

Figure 5.25: Comparison of steady state and transient mass fraction burned histories during a 0.5 s tip-in transient at **2000 rpm**. Shaded regions correspond to injection events. OM611, reference fuel.

It should be noted that the most significant challenge for investigating the combustion processes during transient operation, is the estimation of the thermodynamic state at IVC (in particular the mass of the cylinder contents and EGR rate) and obtaining a signal with a satisfactory signal-to-noise ratio. To minimize errors in the estimation, the air mass flow rate was estimated based on the measured relative air fuel ratio (from the λ-sensor) and injected fuel mass (from the ECU).

5.5.5   In Cylinder Pyrometry

From the global engine parameters (T_{ivc} and λ_{ox}) it was postulated above that the increase seen in the soot emissions during the tip-in transients is predominantly caused by a short term lack of oxygen, resulting in a reduced oxidation. To validate this hypothesis, the in-cylinder KL measurements were used to characterize the cycle-specific particle formation ($(KL)_{max}$) and oxidation (γ_{ox}) processes in cylinder three during the 0.5 s tip-in transients at both engine speeds.

Figure 5.26 provides an overview of the cylinder-out soot emission (characterized using $(KL)_{end}$), the formation ($(KL)_{max}$) and the oxidation (γ_{ox}) during the transients. These three parameters are shown normalized relative to their values prior to the transient. As a reference, the injected fuel mass is also shown. As expected, $(KL)_{end}$ is seen to increase, in agreement with the exhaust-stream measurements. During the transient, the injected fuel quantity and injection pressure are increased, which results in an increase in $(KL)_{max}$. The tendency for $(KL)_{max}$ to increase with increasing fuel quantity and injection pressure has also been noted in other steady-state pyrometry investigations [89]. During steady operation the increase in formation ($(KL)_{max}$) is associated with a corresponding increase in the oxidation (γ_{ox}). This is evident in the initial portions of the transient, though towards the end of the transient, particularly in the 1250 rpm case, the oxidation was seen to lag behind the increase in formation. Thus the increase in the cylinder-out soot is attributed to a poor oxidation. The reduction in oxidation towards the end of the transient is much more evident at 1250 rpm than at 2000 rpm, again due to the higher overall charge pressures and oxygen concentrations at the higher engine speed.

In the lower portion of figure 5.26 the KL parameters for the tip-in at 2000 rpm are shown and can be used to describe the short term reduction in soot emissions seen after the transient. After the short term spike in $(KL)_{end}$ caused
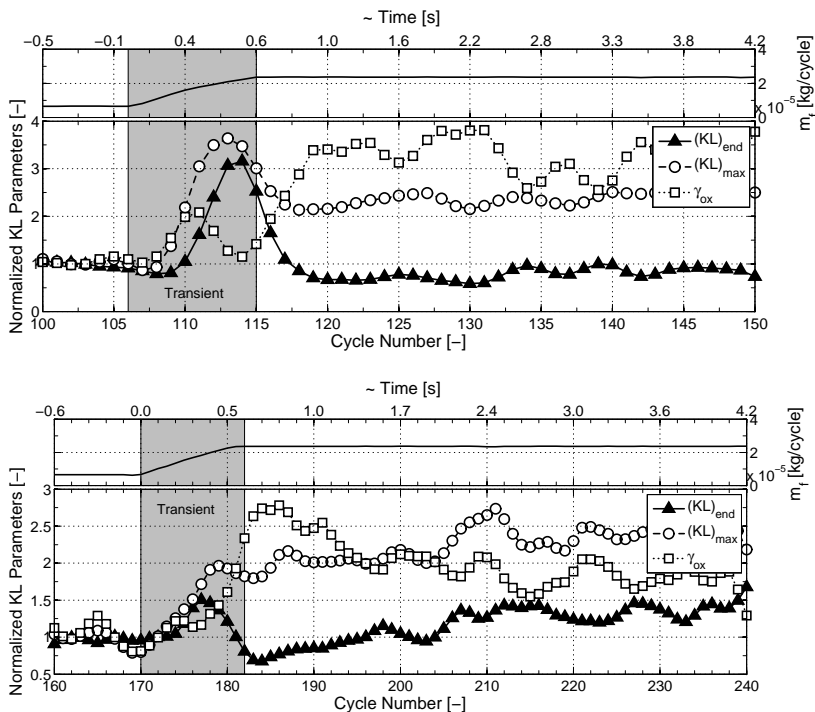
Figure 5.26: Cycle specific soot formation and oxidation characteristics dur-
ing $\Delta t = 0.5\,\text{s}$ tip-in transients at $1250\,\text{rpm}$ (top) and $2000\,\text{rpm}$ (bottom).
OM611, reference fuel, cylinder 3.

by the delayed increase in the oxidation, $(KL)_{max}$ reaches a plateau (approxi-
mately cycles 185 to 210) and then slowly begins to increase as γ_{ox} decreases
and hence $(KL)_{end}$ increases. The short-term reduction in the soot emissions
(compared to steady-state operation) after the transient are therefore caused
by a reduced formation. A potential cause of the reduced formation may be
the reduced charge temperatures (see figure 5.18) resulting in decreased soot
formation rates.

1250 rpm, 2 bar BMEP, cycles 105 - 107

1250 rpm, 3 bar BMEP, cycle 108

1250 rpm, 4 bar BMEP, cycle 109

1250 rpm, 5 bar BMEP, cycle 110

1250 rpm, 6 bar BMEP, cycle 111

1250 rpm, 7 bar BMEP, cycle 113

1250 rpm, 8 bar BMEP, cycles 115, 117, 120, 130 *
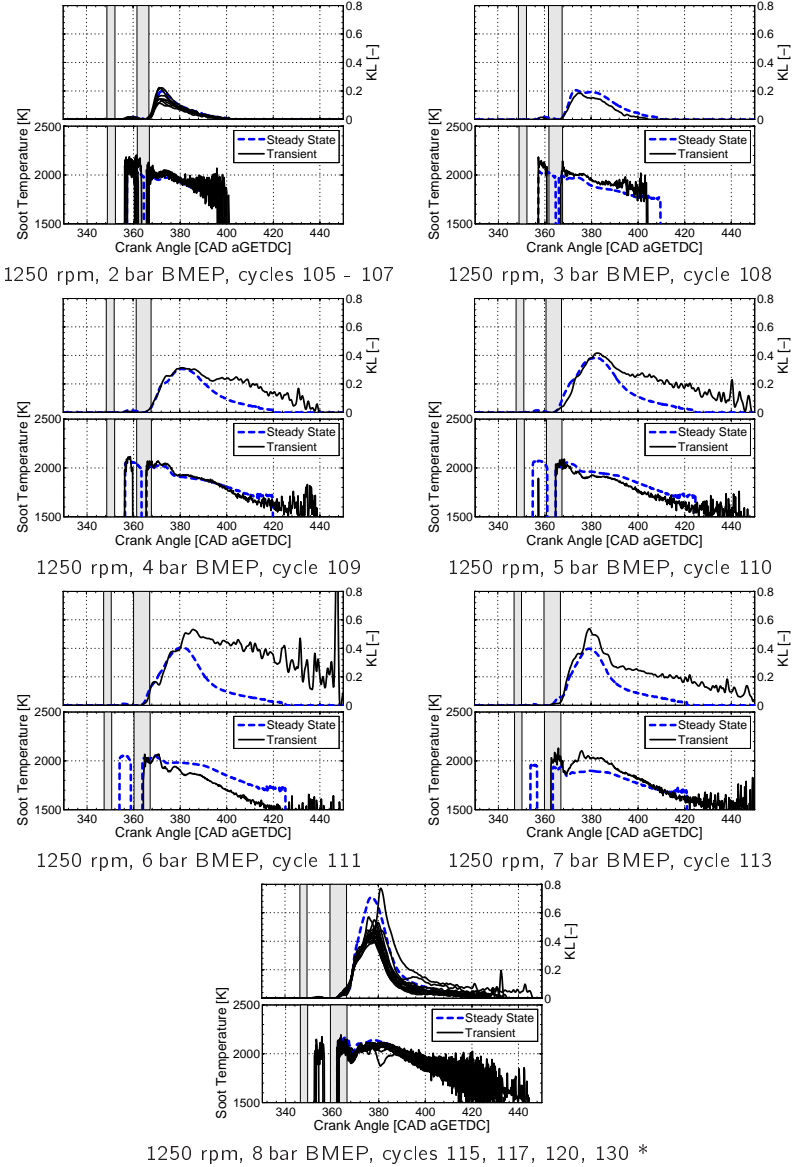
Figure 5.27: Comparison of steady state and transient pyrometry measurements during a tip-in transient at 1250 rpm. Shaded regions denote injection events. (*) Sensor contamination during steady state measurements.

1250 rpm, 2 bar BMEP, cycles 170 & 171

1250 rpm, 3 bar BMEP, cycle 172

1250 rpm, 4 bar BMEP, cycle 174

1250 rpm, 5 bar BMEP, cycle 175

1250 rpm, 6 bar BMEP, cycle 177

1250 rpm, 7 bar BMEP, cycle 179

1250 rpm, 8 bar BMEP, cycles 182, 185, 190, 200, 215, 230
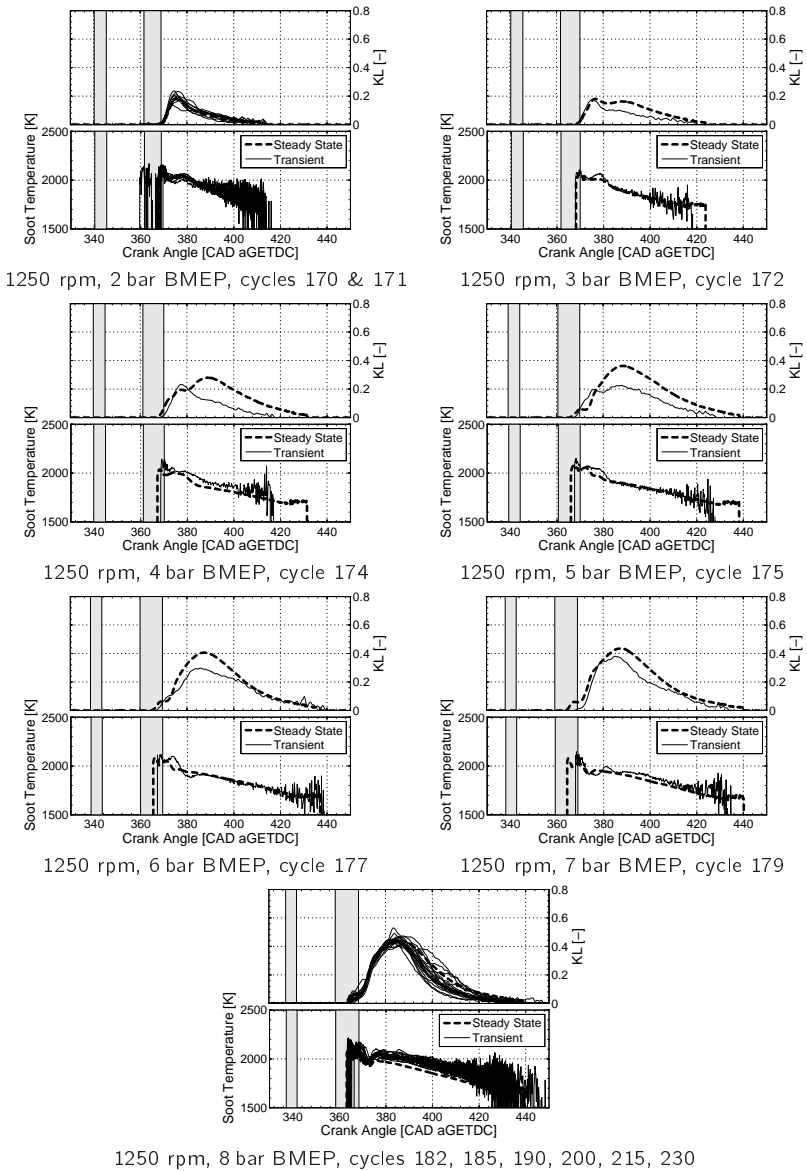
Figure 5.28: Comparison of steady state and transient pyrometry measurements during a tip-in transient at 2000 rpm

To gain a more in-depth understanding of the transient in-cylinder KL factors and soot temperature, they were compared to representative KL factor and temperature histories during steady-state operation. The histories were compared for cycles with the same engine speeds and BMEPs, as shown in figures 5.27 and 5.28 for 1250 rpm and 2000 rpm, respectively. During the 1250 rpm transient (figure 5.27), it is evident that there is no considerable difference between the formation ($(KL)_{max}$) during steady-state and transient operation. At later stages in the transient (cycles 109-115), an inhibited oxidation process is noticeable. In particular, the oxidation rate [9] and total oxidized mass is considerably smaller than during steady-state operation. This decrease in oxidation occurs at approximately the same stage in the transient as the oxygen deficit characterized using λ_{O_2}. This supports the hypothesis that the increase in the cylinder-out soot emissions is caused by a decrease in the oxidation and not through changes in the formation process. At the higher engine speed (figure 5.28), there is no considerable difference between the steady-state and transient operation, as there is no critical oxygen deficit. In general, the transient KL factor histories are lower than the measured steady-state values, though this is likely due to sensor contamination during the transient measurements.

Similar to the cylinder pressure measurements, a significant challenge for transient pyrometry measurements is ensuring that a satisfactorily high signal-to-noise ratio is obtained. This is of particular concern for pyrometry, as at the point where $(KL)_{end}$ is determined, the signal intensity is extremely low. Indeed considerable noise is evident in the transient measurements[10] towards the end of the measurement, which introduces considerable difficulty in determining $(KL)_{end}$.

5.6   Soot Measurement Uncertainty

Exhaust Stream Measurements

The repeatability of the exhaust stream soot emission measurements was quantified through consideration of all measurements of the reference point (3000 rpm, $BMEP = 8$ bar). Throughout the course of the OM611 mea-

---

[9]The oxidation rate can be approximated using the slope of the KL factor after its maximum value.

[10]The transient histories are based on the measurements of a single cycle, while the steady-state measurements are the average of 144 cycles. When only a single cycle during steady-state operation is considered, significant noise is also seen.
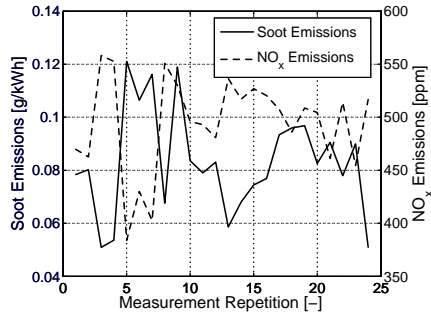
Figure 5.29: Repeatability of soot and NO_x emissions during multiple repetitions of the steady state reference point. OM611 reference fuel, 3000 rpm, $BMEP = 8$ bar.
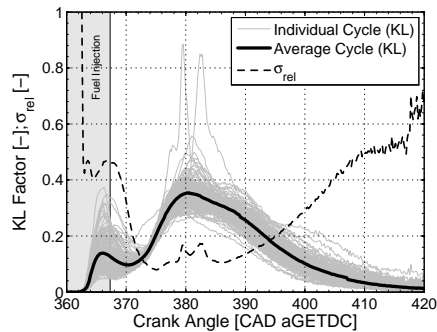
Figure 5.30: Cycle-specific variability of KL histories during steady state operation. OM611, reference fuel, 3000 rpm, $BMEP = 8$ bar.

surements, the reference point was measured a total of 24 times with the same engine configuration, during steady state and transient measurement campaigns, over a period of approximately one month. The measured soot and NO_x emissions are given in figure 5.29 for each of the measurement repetitions (the NO_x emissions are only included as a reference). Overall, the soot emissions varied with a relative standard deviation[11] of 24%, while the NO_x emissions varied by 9.1%.

As with all other steady state measurements presented in this chapter, the

---

[11]The relative standard deviation is defined as $\sigma_{rel} = \sigma / \bar{x}$.

reference operating point was defined through an engine speed and mean effective pressure. All remaining engine operating parameters were set by the ECU. On the same engine, it was found that by additionally defining the injection pressure, injection timing, and EGR valve position, the repeatability of the soot measurements could be improved to a relative standard deviation of 10% [66]. In a comprehensive study [34], the repeatability of tailpipe particulate mass measurements over the NEDC from several different vehicles at various labs was presented. It was found that depending on the vehicle, the variability in the measured soot emissions can range from 8% to 97%, with vehicles without aftertreatment having the lower variabilities.

In-Cylinder Measurements

When the in-cylinder measurements are considered, it is possible to quantify the variability in the cycle and cylinder specific particulate emissions. Shown in figure 5.30 are the KL factor histories for 144 consecutive cycles at the steady state reference operating point. Additionally the temporal inter-cycle variability is shown using the relative standard deviation σ_{rel}. Particularly towards the end of oxidation a large variability, on the order of $\sigma_{rel}(KL) = 80\%$ in the cycle-specific KL values is seen. At the beginning of the combustion processes a large inter-cycle variability is expected due to variations in the localized mixture state. During the soot formation periods (between approximately 372° and 380°CAD) there is generally a low variability in KL. After the global KL maximum, during the oxidation process, the variability once again begins to increase. This indicates that not only is there a large inter-cycle variability in the cylinder-out particle emissions, but that it is largely due to the oxidation process. The variability in the oxidation stems from the fact that it is largely dependent on the local oxygen concentration, which in turn is strongly influenced by the in-cylinder turbulence. During the later stages of the cycle, the in-cylinder turbulence is no longer dominated by the well-defined injection process, but rather by the charge motion, which is influenced by piston motion and combustion itself.

By comparing the $(KL)_{end}$ values from all cylinders, it is possible to quantify the inter-cylinder soot emissions variability. As was shown in figure 5.1, the $(KL)_{end}$ values from cylinders three and four were similar ($\sim 8\%$ difference), while cylinder one had considerably higher values. As already mentioned, the higher values from cylinder one were attributed to a poor signal to noise ratio and its implications for the data processing, and not necessarily a difference in the particle emissions. In other works, significant difference in the cylinder

specific soot emissions have been noted [48].

The repeatability of the soot emissions measured during the transients has already been commented on in section 5.5. It was seen that the soot emissions can vary considerably (up to ±50%) particularly for the shorter duration transients.

5.7 Summary

Through the consideration of the exhaust stream and in-cylinder soot concentrations, along with a combustion analysis, the influences of steady state engine parameters, fuel properties, and transient engine operation on the soot emissions were evaluated. It was found that three-color pyrometry could be used to characterize the cylinder and cycle-specific soot emissions, as well as the in-cylinder soot formation and oxidation processes. This method however is sensitive to errors in the calibration introduced by window contamination and low signal-to-noise ratios.

The influences of the global steady state engine parameters on the exhaust stream soot emissions, has been well described in the literature. The trends observed in this work are in agreement with literature. The pyrometry results here indicated that the soot formation is largely a function of only the engine load, while the soot oxidation is much more sensitive to the engine operating parameters. The relevance of the soot oxidation was also seen during inter-cycle comparisons where the large inter-cycle variability was attributed to fluctuations in the oxidation process at later stages in cycle.

Operation with fuel two resulted in lower soot emissions throughout the entire operating map, compared to operation with the reference fuel. A combustion analysis, which was carried out at several operating points, indicated that the primary difference between the two fuels was in the soot processes and not due to changes in the combustion. Through the use of in-cylinder pyrometry, the reduction in the soot emissions was attributed to a reduced soot formation rate caused by the low aromatic content of fuel two.

The acceleration transients were not found to have a significant effect on the soot emissions, while the tip-in transients did. In particular, the short duration transients at low engine speeds were seen to result in considerable increases in the soot emissions. Through consideration of the global engine parameters, this was attributed primarily to a momentary oxygen deficit. Additionally, a short-term reduction in the soot emissions was seen immediately following the transient, explained by a short term reduction in the mean charge temperature

at intake valve closing. The influence of this temperature is described primarily by the $\phi - T$ map in which a reduction in temperature results in a reduction in the soot emissions.

Further insight was gained through the consideration of the combustion and soot formation and oxidation processes during transient operation, on the basis of cylinder pressure and pyrometry measurements. It was seen that the maximum heat release rate increased at first due to higher relative injection pressures, and then decreased due to the global oxygen deficit. In general, the differences between the combustion during steady-state and transient operation - characterized based on global thermodynamic measurements - were not as significant as the difference seen in the exhaust stream soot emissions or in-cylinder pyrometry measurements.

From the in-cylinder pyrometry measurements, the spike in the soot emissions could be attributed to a weak oxidation process (γ_{ox}), due to the lack of oxygen. The formation process ($(KL)_{max}$) was seen to be relatively unchanged during the transient, when compared to steady-state operation. The short-term reduction in the soot emissions following the transient (primarily at 2000 rpm) was attributed to an inhibited soot formation process, due to the lower charge temperature and hence formation rates.

Chapter 6

Model Calibration and Validation

6.1 Introduction

Using the steady-state measurements presented in chapter 5, the MVSM was parameterized for each of the investigated engine and fuel combinations using evolutionary algorithms. Based on the steady state implementation of the MVSM, several sensitivity analyses were carried out to elucidate the influences of the model parameters, inputs, as well as the number of operating points considered during the parameterization. Using the model parameterized for the OM611 operating with the reference fuel, the ability of the MVSM to calculate the soot emissions during transient operation was evaluated.

6.2 Steady State MVSM Parameterization and Validation

The MSVSM was parameterized for each of the engine-fuel combinations by following the same general procedure outlined in section 3.6. The parameterization of the MVSM for operation with the reference fuel was considered to be the base case, in that the resulting parameter set would be used directly for the transient investigations, and would also serve as a basis for parameterization for fuel 2. The parameterization for engine two and fuel three was carried out
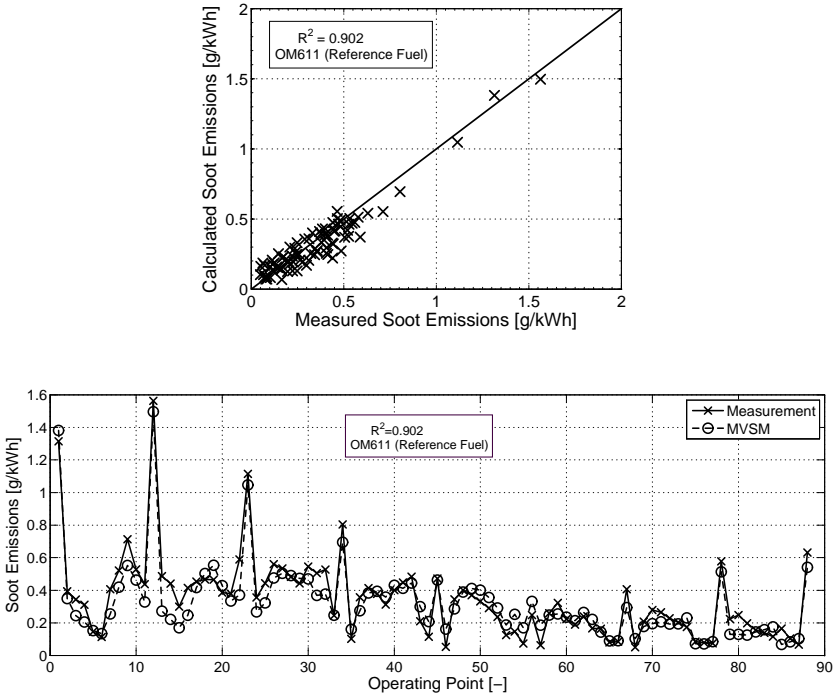
Figure 6.1: Comparison of the calculated and measured soot emissions for steady state operation after model parameterization. OM611, reference fuel.

as a validation of the applicability of the MVSM to other engines. For each of the parameterizations, the performance of the MVSM was quantified using the correlation coefficient (R^2, equation 3.47) and the mean of the square errors ($\bar{\delta}^2$, equation 3.48).

6.2.1   OM611 - Reference Fuel

As it was the basis parameterization of the MVSM, all 16 of the parameters listed in table 3.1 were parameterized based on 89 steady state operating points (excluding the reference measurements) using evolutionary algorithms. The parameterization required 15 generations, each with 400 individuals, resulting in a total parameterization time of approximately 2 hours. As shown in figure 6.1, the parameterized model was able to reproduce the qualitative and

quantitative soot emissions trends for all considered operating points. All of the model inputs (see table 3.2) were taken either from the ECU, fuel properties, or engine geometry, with the exception of the intake charge temperature and the EGR rate, as already discussed.

The ECU intake temperature sensor is located after the intercooler, but upstream of the EGR mixing point, and thus does not consider the influence of the EGR on the actual gas temperature at IVC. Thus the average of the gas temperature measured using a thermocouple in all of the intake runners was used. Alternatively, it is possible to use the estimated intake charge temperature according to equation 4.15, in which case the correlation coefficient of the parameterization drops from 0.90 to 0.81. More modern diesel engines are equipped with charge temperature sensors rather than intake air temperature sensors [84] so neither an additional sensor, nor a model for the estimation of the charge temperature is required. As the ECU does not provide the actual EGR rate, it was taken from the direct measurements outlined in section 4.3.1. It is possible to estimate the EGR rate based on the fresh air mass flow rate and an estimate of the mass flow rate entering the cylinder, or based on a model of the mass flow rate through the EGR valve, though both of these methods require additional transducers[1] [30].

6.2.2   OM611 - Fuel 2

Using the parameter set determined from the reference fuel parameterization, the MVSM was parameterized for the OM611 using fuel two by changing only model parameters considered to be influenced by a change in the fuel properties. These parameters included:

A_{form}, A_{ox} Soot formation and oxidation rate scaling factors

β The fuel evaporation coefficient is expected to change as the new fuel has a lower evaporation temperature (see equation 3.8).

λ_{form}, n_1 The representative relative air-fuel ratio of the formation was varied as this is used in conjunction with the $\Phi - T$ map to describe the chemistry of the soot formation, which is expected to be different for the new fuel due to its different composition. The soot formation kinetics

---

[1]The estimate based on mass flow rates requires the mixture density in the intake manifold and thus the gas temperature in the intake manifold which could be estimated using $T_{ivc,est}$. Additionally, the exhaust manifold pressure is also required to estimate the volumetric efficiency. To determine the mass flow rate of EGR through the EGR valve, the valve position and the pressure ratio across the valve is needed.
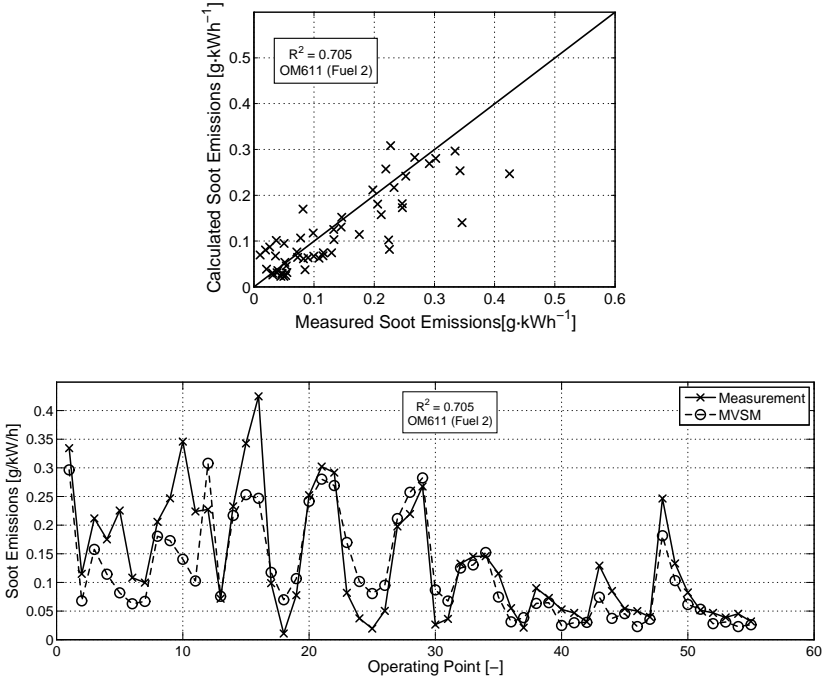
Figure 6.2: Comparison of the calculated and measured soot emissions for steady state operation. OM611, fuel two.

were also thought to be influenced differently by the cylinder pressure (characterized using the exponent n_1).

C_{diff}, φ_{ox}, n_4 The soot formation duration scaling factor, representative oxidation crank angle and oxygen partial pressure exponent were expected to change due to the different combustion characteristics of the new fuel caused by the lower cetane number, evaporation temperature, and density.

C_{inj}, n_3 Because of the different viscosity of fuel two, the injection generated turbulence scaling factor along with the fuel injection pressure exponent were varied. This influence was noted *a posteriori*.

After the determination of the above listed 10 parameters for the OM611 with fuel two, the MVSM was capable of reproducing the qualitative and quantitative trends of the measured soot emissions, as shown in figure 6.2. Table

6.1 presents a comparison of the model parameters determined for operation with both fuels, the respective parameterization times, and the performance characteristics of the parameterized model. When the correlation coefficients for the parameterization with the reference fuel and fuel two are compared, a somewhat lesser agreement is seen with fuel two, though the absolute error characterized using $\bar{\delta}^2$ is also lower for fuel two (see table 6.1).

The changes in the MVSM parameters outlined in table 6.1 could, in part, be explained through physical and chemical considerations, though due to the simplistic nature of the model the parameters also serve to account for processes not considered by the MVSM. From the lower aromatic content of fuel two, a lower soot formation rate is expected (as seen from the in-cylinder pyrometry measurements, see figures 5.7 through 5.10), and is compensated for by a decrease in λ_{form}, which results in a decrease in the calculated soot mass (see section 6.3.1). That the formation scaling factor increased rather than decreased as would be expected, is overcompensated by the reduction in λ_{form} and reduction in the soot formation duration scaling factor C_{diff}. The observed increase in the oxygen partial pressure exponent n_4 implies an enhanced oxidation and lower soot emissions, though as will be discussed in section 6.3.1, the MVSM is relatively insensitive to this parameter. It is worth re-iterating that while the changes in the MVSM parameter values for the two fuels can generally be explained, the parameters do also serve as means for describing phenomena which are not completely captured by the MVSM. They cannot be taken as absolute representation of the physical parameters which they are to assumed to represent.

From the above two validations, the MVSM has been shown to be capable of calculating the soot emissions across an engine operating map for two different fuels.

6.2.3 Engine Two - Fuel Three

To evaluate the ability of the MVSM to calculate the soot emissions from a different engine, it was parameterized using the two measurements series from engine two (operating with fuel three). There were several differences in the available measured parameters for the two measurement series. During the operating map measurements (see figure 5.12) the majority of the engine parameters were specified by the ECU, while for the parameter variation series, prescribed parameter values were used. As a new engine-fuel combination was being considered, all were re-parameterized. A measurement of the EGR rate

Parameter	OM611 Reference Fuel	OM611 Fuel 2	Engine 2 Fuel 3
A_{form}	**31**	**80**	**800**
A_{ox}	**1e10**	**2.9e14**	**9.12e11**
β	**1e-7**	**1e-7**	**5.03e-6**
λ_{diff}	**1.0**	1.0	**0.86**
λ_{form}	**0.02**	**0.0144**	**0.0011**
$T_{A,ox}$	**9.65e4**	9.65e4	**3.85e4**
$T_{ox,min}$	**1585**	1585	**1580**
c_{pm}	**4.49**	4.49	**1.0**
c_{inj}	**1.95**	**20**	**10**
c_{diff}	**2.55**	**1.67**	**4.40**
c_{O_2}	**3.1**	3.1	**2.0**
φ_{diff}	**360**	360	**360**
φ_{ox}	**388**	**401**	**440**
n_1	**0.61**	**0.64**	**2.38**
n_3	**-4.2**	**-4.7**	**-1.4**
n_4	**1.53**	**4.37**	**3.31**
R^2	0.902	0.705	0.88
MSE [g/kWh]	6.54e-3	3.35e-3	4.09e-003
N_{points} [-]	89	55	55
N_{gen} [-]	15	5	5
$\sim t_{param}$ [h]	2	1	1

Table 6.1: Optimum model parameters determined using the evolutionary algorithms for each of the engine and fuel combinations. Bold values indicate that the parameter was varied during the parameterization

was not available for the operating map measurements and thus required estimation, while a measured EGR rate was available for the parameter variation measurements. Additionally, the intake charge temperature was measured directly for the parameter variations, while for the operating map measurements only the fresh air temperature after the intercooler was available. It should also be noted that the soot emissions were quantified using a FSN for all measurements on engine two. While FSN has been shown by numerous investigations, including this one (see figure 4.10), to correlate well with measurements of the elementary carbon concentration, it is not a direct measurement thereof.
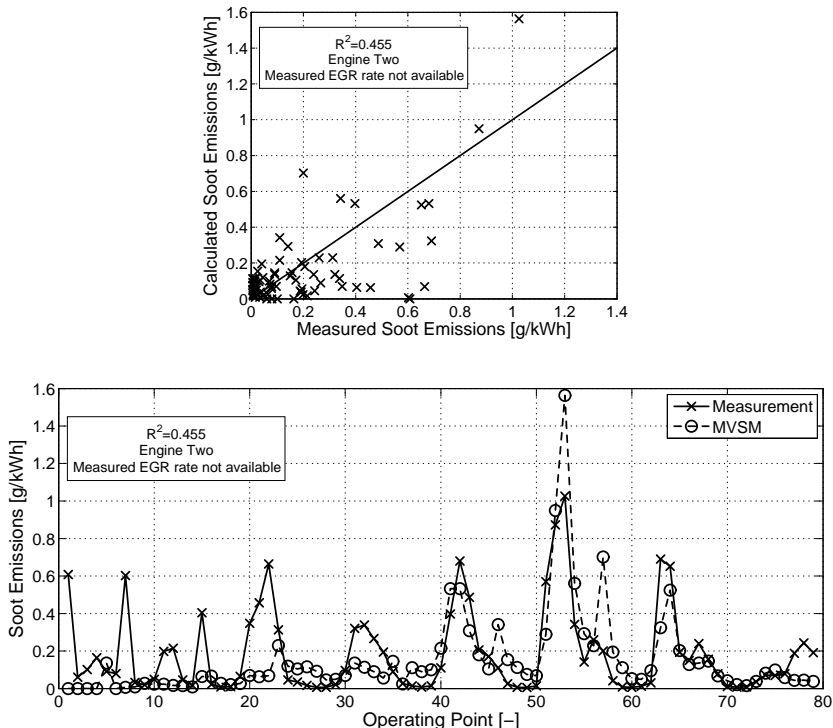
Figure 6.3: Comparison of the calculated and measured soot emissions for ECU defined steady state operation of engine two with fuel three. NOTE: Measured EGR rate not available and was estimated according to equation 4.4.

Operating Map

Using all 120 operating points the MVSM was parameterized, whereby the EGR rate was estimated based on the measured fresh air mass flow rate (from the mass flow meter) and the mass flow rate of the mixture drawn into the cylinder, as described in equation 4.4. The parameterization required 15 generations, after which the MVSM could only partially reproduce the qualitative soot emission trends, as shown in figure 6.3. The poor performance of the MVSM is attributed to the lack of an accurate EGR and intake charge temperature measurement.
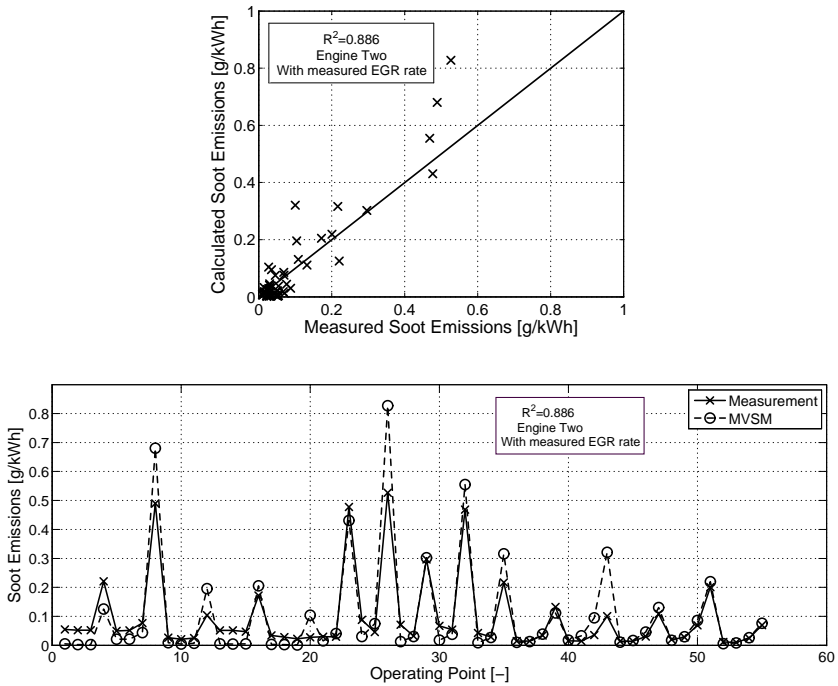
Figure 6.4: Comparison of the calculated and measured soot emissions for defined parameter variation on engine two with fuel three.

Parameter Variation

For the parameterization of the MVSM, all model parameters were once again varied as the results with the operating map measurements were not satisfactory. Shown in figure 6.4 is a comparison of the measured soot emissions and those calculated using the MVSM parameterized omitting the 5 operating points with very high soot emissions ($>4\,$g/kWh, see figure 5.12). The MVSM is capable of reproducing the qualitative and quantitative soot emissions with an accuracy similar to that for the OM611. When the operating points with very high soot emissions are considered during the parameterization, they were found to reduce the fidelity of the MVSM in the typical emissions regime ($\lesssim 1\,$g/kWh). The improved performance of the MVSM compared to the operating map measurements is attributed to accurate knowledge of the EGR rate and intake charge temperature.

When the soot emissions for the omitted operating points are calculated using the MVSM as parameterized in figure 6.4 (i.e. without a subsequent re-parameterization), the MVSM is capable of predicting the drastic increase in soot emissions caused by the 10% increase in the EGR rate. Despite the MVSM not having considered such high soot emissions during the parameterization, the correlation coefficient is only marginally decreased ($R^2 = 0.89$ to $R^2 = 0.79$), indicating that the MVSM is capable of reproducing soot emissions outside of the region for which it was calibrated, due to the consideration of the underlying chemical and physical processes.

6.3 Model Analysis

While the ability of the model to reproduce the soot emissions has been shown above, it is of interest to understand how the calculated soot emissions are influenced by the model parameters, the model inputs, and the number of operating points considered during parameterization. To this end, sensitivity analyses were carried out, in which each of the aforementioned parameters were varied and their effect on the calculated soot emissions quantified. For all three of the sensitivity analyses the steady state measurements and MVSM parameterized for the OM611 operating with the reference fuel, as outlined in table 6.1, were used.

6.3.1 Sensitivity Analysis: Model Parameters

To determine the relative influence of the model parameters, each parameter was increased or decreased by a factor of 3/2 and 2/3, respectively from the basis values. The relative change in the calculated soot emissions as a result of a change in each parameter is shown in figure 6.5, where the relative change is defined as:

$$\Delta m_s = \frac{m_{s,mod}}{m_{s,basis}} \tag{6.1}$$

The most dominant influences are from the representative relative air-fuel ratio in the soot formation zone λ_{form} and the cylinder pressure exponent n_1, which also influences the soot formation (see equation 3.3). λ_{form} is used in conjunction with the $\Phi - T$ map to determine the normalized soot yield, though here an increase in λ_{form} (a decrease in Φ) should result in a decrease in the soot emissions. However, in figure 6.5 the opposite is seen, implying that this not the primary influence of λ_{form}. Recall that λ_{form} is also used for
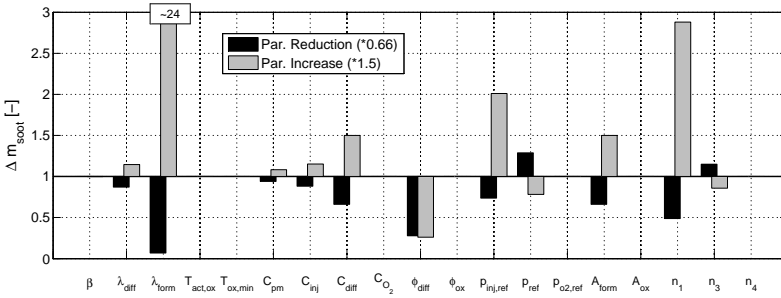
Figure 6.5: Influence of the model parameters on the calculated soot emissions. OM611, reference fuel, 2250 rpm, $BMEP = 6.0\,\text{bar}$.

the estimation of the soot formation zone temperature:

$$T^*_{form} = T^*_{ign} + \Delta T_{adb} \tag{3.27}$$

$$\Delta T_{adb} = \begin{cases} \dfrac{LHV}{c_p(1+\lambda_{form} m_{air,st})} & \text{if } \lambda_{form} \geq 1, \\[3mm] \dfrac{LHV}{c_p(1+\lambda_{form} m_{air,st})}\lambda_{form} & \text{if } \lambda_{form} < 1 \end{cases} \tag{3.28}$$

where an increase in λ_{form} results in an increase in the soot formation temperature. As discussed below, the soot formation temperature has a strong influence on the soot formation rate.

Also evident in figure 6.5 is that the oxidation relevant parameters, generally have little or no influence on the calculated soot mass. Indeed, it was found that the parameterized model tends to reproduce the soot emission trends primarily through consideration of the formation process, and is insensitive to changes in the oxidation. This is an important limitation of the MVSM, as the preceding chapter has well illustrated the importance of the oxidation process, particularly during transient operation. An improvement of the oxidation component of the MVSM will be the focus of future investigations.

6.3.2 Sensitivity Analysis: Input Parameters

In a similar fashion to the model parameter sensitivity analysis, the influence of inaccuracies in the model input parameters (engine operating conditions) was investigated. The input parameters were increased and decreased by a factor of 5/4 and 4/5, respectively. Shown in figure 6.6 are the relative changes
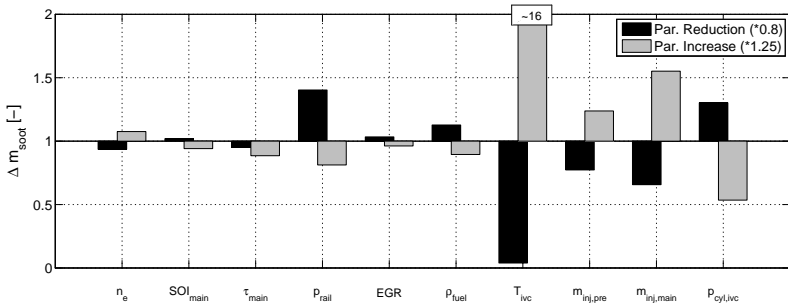
Figure 6.6: Influence of the model inputs on the calculated soot emissions. OM611, reference fuel, 2250 rpm, $BMEP = 6.0$ bar.
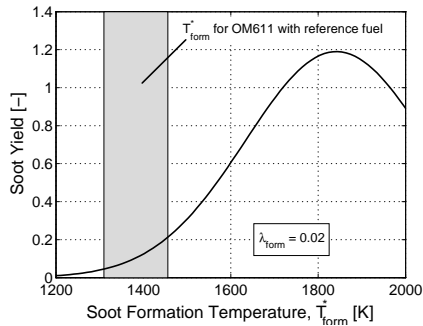
Figure 6.7: Influence of the soot formation temperature on the soot yield. OM611, reference fuel.

in the calculated soot emissions for variations in the individual model input parameters, where it can be seen that the temperature at intake valve closing, T_{ivc} has a very strong influence on the calculated soot emissions. This is again due to the dependance of the soot formation function ($\Phi - T$ map [3]) on the temperature in the soot formation zone, T_{form}, which is estimated based on T_{ivc}. The influence of the soot formation temperature on the soot yield is shown in figure 6.7 for $\lambda_{form} = 0.02$ (value for λ_{form} resulting from the parameterization, see table 6.1) as well as the range of soot formation temperatures considered by the MVSM for all OM611 operating points with the reference fuel. In this two dimensional slice of the $\Phi - T$ map, the strong
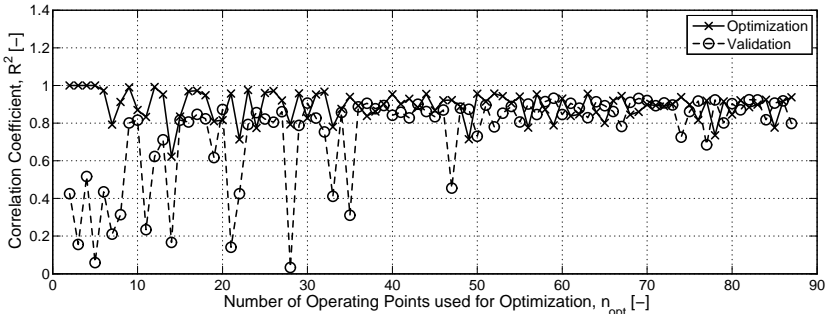
Figure 6.8: Influence of the number of stochastically selected operating points considered during the MVSM parameterization on the MVSM performance during validation. OM611, reference fuel.

influence of the soot formation temperature on the soot yield is evident.
The intake charge temperature influences not only the soot formation temperature, but also the combustion process itself, which naturally also has consequences for the soot emissions. For example, a decrease in the charge temperature results in a longer ignition delay and more time for fuel evaporation. This results in a higher premixed combustion fraction, which coupled with the assumption that soot is only formed during the diffusion controlled combustion, implies a reduction in the soot emissions. The necessity for an accurate estimation of the charge temperature at IVC for an accurate calculation of the soot emissions has also been noted by others [22].

6.3.3   Sensitivity Analysis: Number of Operating Points for Parameterization

A sensitivity analysis to determine the influence of the number of operating points considered during the model parameterization was carried out. In particular the number of operating points considered for parameterization was systematically varied from 2...87, whereby for each parameterization, the operating points were randomly selected. The resulting parameter set was then used to calculated the soot emissions for the remaining points not considered during the optimization. For example: 87 operating points were randomly selected from the available 92, the parameterization was carried out based on the 87 operating points, and the resulting parameter set was used to calculate the soot emissions for the remaining 5 operating points. The correlation be-

tween the measured and calculated soot emissions was characterized using the correlation coefficient for both the parameterization and validation operating points. This process was then repeated for 86, 85, 84, ... 2 operating points for the parameterization. The parameterization and validation correlation co-efficients are shown for all considered number of parameterization operating points in figure 6.8. When fewer than ~50 operating points are considered for the optimization, the validation correlation coefficient begins to decrease. This implies that ≈50 operating points are required for the parameterization of MVSM for this type of engine. As the number of degrees of freedom afforded by the ECU increases or decreases, so too will the required number of operating points. The somewhat stochastic reduction in the validation correlation coefficient is due to the random selection of the operating points.

6.4 Model Validation for Transient Operation

Using the transient measurements presented in section 5.5, the ability of the model to predict the soot emissions during transient engine operation was evaluated. As the MVSM is based on phenomenological consideration, it should be able to reproduce the soot emissions during transient operation, given that all relevant processes are adequately described and that the model inputs are temporally correct. As such the MVSM parameterization was not changed from that which was determined for steady state operation as given in table 6.1.

6.4.1 Model Extensions

As a preliminary trial, the MVSM was implemented without any changes to calculate a 0.5 s tip-in transient at 1250 rpm, the results of which are shown in the left hand side of figure 6.9. It is seen that the peak in the soot emissions caused by the transient is under-estimated by the MVSM and that the decay of the soot emissions peak is considerably drawn out compared to the measured values. For these calculations the measured EGR rate and intake charge temperature were used, as was the case for the steady parameterization. In light of the strong influence of the intake charge temperature seen during the sensitivity analyses, the measured intake charge temperature was replaced *a posteriori* with that estimated according to equation 4.15. When the soot emissions are calculated using this temperature, they are in much better agreement with the measured values, as seen in the right hand side of
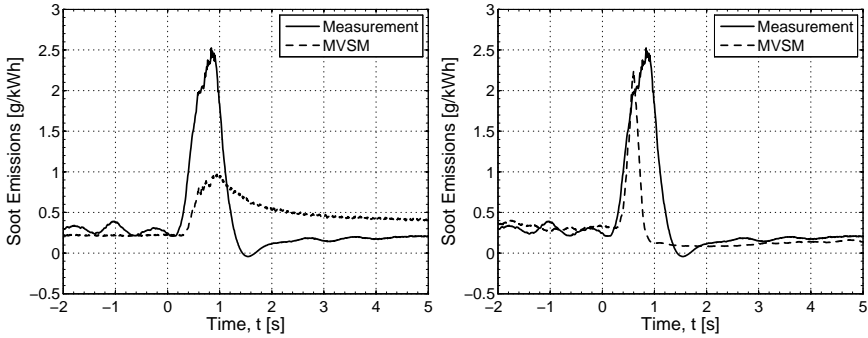
Figure 6.9: Comparison of the measured soot emissions and those calculated using the measured intake charge temperature (left) and an estimated intake charge temperature (right). Tip-in transient ($\Delta t = 0.5$ s, 1250 rpm), OM611, reference fuel.

figure 6.9. Neither the undershooting, nor the delayed decay of the soot emissions peak are evident, which is attributed to the better temporal resolution of the estimated charge temperature than its corresponding measured value. When the estimated intake charge temperature, as defined by equation 4.15, was used as an input, however, it was found that the MVSM was not capable of reproducing the soot emissions during the acceleration transient, as shown in the left hand side of figure 6.10. After consideration of various engine parameters, it was found that the EGR temperature measurement, which is used in equation 4.15 for the charge temperature estimation, lacked the temporal resolution to describe the change in EGR temperature during the transient[2]. As means of correcting the estimated charge temperature, and hence the too slow EGR temperature measurement, the corrected charge temperature, $T^*_{ivc,est}$, was defined as the weighted average of the steady-state estimate charge temperature (determined using the QSS approximation) $T^{stat}_{ivc,est}$ and the estimated charge temperature during the transient according to equation 4.15, $T^{trans}_{ivc,est}$:

$$T^*_{ivc,est} = \zeta \cdot T^{stat}_{ivc,est} + (1 - \zeta)T^{trans}_{ivc,est} \qquad (6.2)$$

where ζ is a weighting factor. It was found that with a weighting factor

---

[2]The thermocouple used to measure the EGR temperature is expected to have a time constant $\tau < 1$ s. However, since it is mounted in the EGR channel it was susceptible to particulate deposition from the exhaust gas, which will decrease the convective heat transfer between the gas and the thermocouple, thereby increasing the response time.
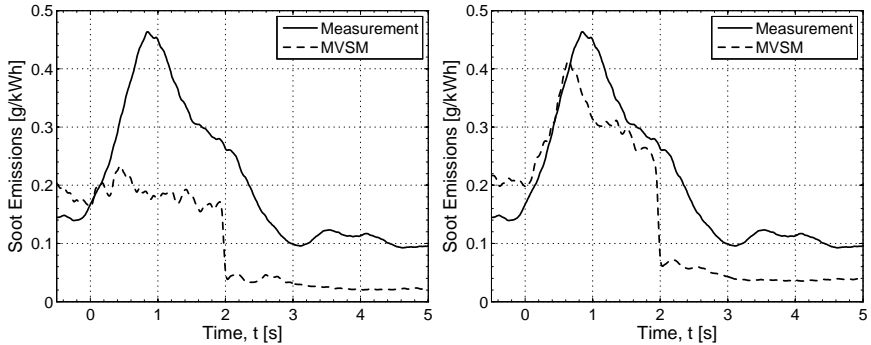
Figure 6.10: Comparison of the measured soot emissions and those calculated using the estimated intake charge temperature, $T_{ivc,est}$, (left) and a corrected intake charge temperature (right), $T^*_{ivc,est}$. First gear acceleration transient, OM611, reference fuel.

of $\zeta = 0.35$ the MVSM could reproduce the soot emission trends during the acceleration (as shown in the right hand side of figure 6.10) and tip-in transients. The sharp drop in the calculated soot emissions at 2 s is due to the transition to an operation without pilot injection and an associated increase in the premixed combustion fraction.

It should be noted that the purpose of equation 6.2 is to correct the slow EGR temperature measurement and not to describe a physical process. The most ideal solution would be to have an accurate, temporally resolved measurement of the intake charge temperature so that such a correction is not necessary. A detailed comparison of the calculated and measured soot emissions for all considered transients follows below.

6.4.2 Acceleration Transients

The soot emissions during the acceleration transients were calculated using the MVSM, whereby the model inputs were the average parameter histories (for example EGR rate) from all repetitions of the transient. Shown in figure 6.11 is a comparison of the measured and calculated transient and calculated steady-state (QSS) soot emissions for the two acceleration transients. Both the average and individual measured soot emission histories are shown to indicate the variability in the measured soot emissions, which, as discussed in section 5.5.1 is considerable. For both of the considered acceleration transients, the
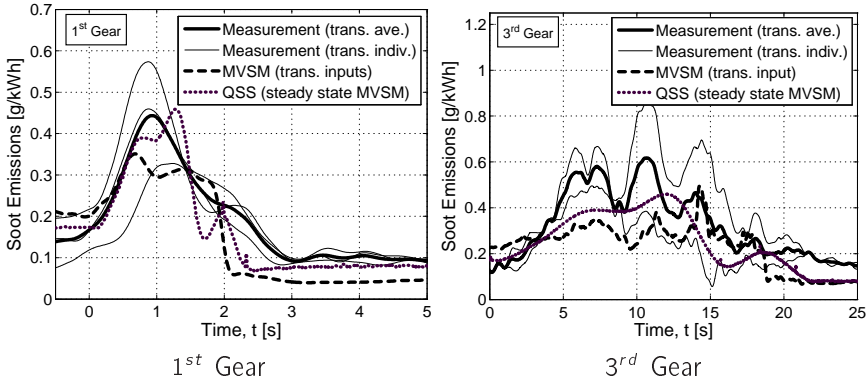
Figure 6.11: Comparison of the measured transient and calculated steady-state (QSS) and transient soot emissions during first gear (left) and third gear (right) acceleration transients of different durations at $BMEP = 8$ bar.

MVSM is capable of reproducing the soot emission history trends, in part to within the limits of the experimental variability. As expected the steady-state and transient calculated soot emissions do not differ substantially, as no major difference was seen between the measured steady-state and transient emissions. Therefore, the MVSM as calibrated for the steady-state operation is capable of calculating the soot emissions during acceleration transients as well, given that an adequate estimate of the intake charge temperature is available.

6.4.3   Tip-In Transients

Following the same procedure, the soot emissions were calculated for all of the considered tip-in transients. Shown in figures 6.12 and 6.13 are comparisons of the measured and calculated soot emissions for tip-in transients at 1250 rpm and 2000 rpm, respectively. For all of the considered tip-in transients at 1250 rpm the MVSM provided an improvement in the estimate of the soot emissions over the QSS, and was generally within the bounds of the experimental variability. The soot emissions peak was over-estimated by the MVSM for all of the tip-in transients at 2000 rpm, despite the fact that the QSS provided an accurate estimate of the peak emissions for 1.0 s and 2.0 s transients. As discussed in section 5.5, there is a period immediately following the tip-in transient during which the soot emissions are lower than their steady-state values. That this phenomena is reproduced by the MVSM, is attributed to the
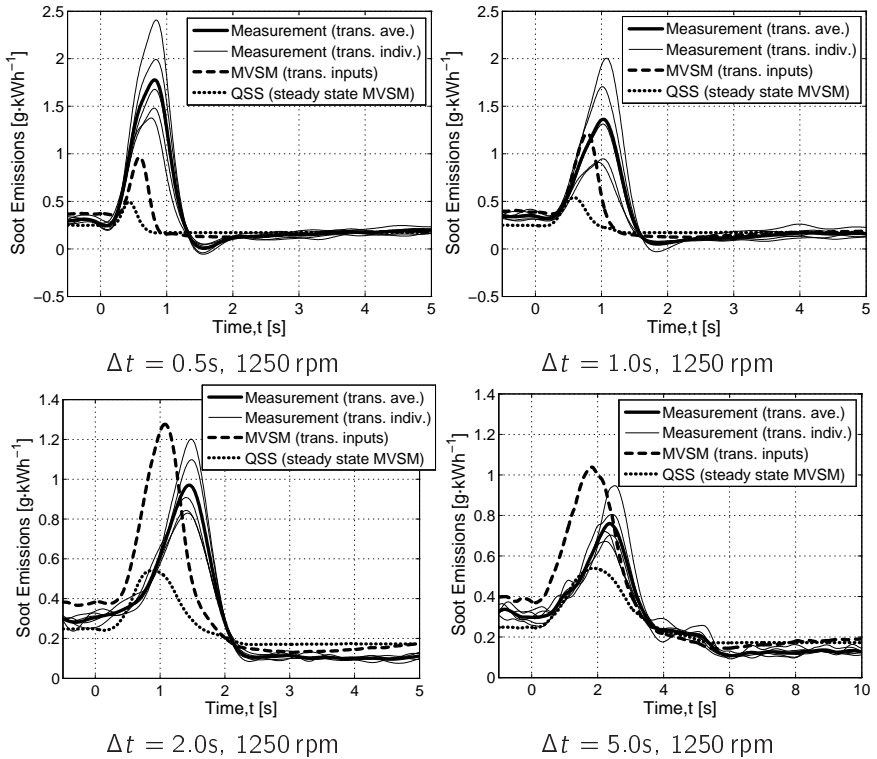
Figure 6.12: Comparison of the measured transient and calculated steady-state (QSS) and transient soot emissions during tip-in transients of different durations at 1250 rpm

consideration of the temporally resolved intake charge temperature $T^*_{ivc,est}$.

6.5 Summary

The steady-state and transient measurements presented in chapter 5 were use to evaluated the ability of the MVSM to reproduce the engine out soot emissions. Additionally, several sensitivity analyses were carried out to gain insight to the behaviour of the MVSM. After parameterization of the MVSM, it was capable of predicting the steady-state qualitative and quantitative soot emission trends from the OM611 engine operating with both fuels. The para-
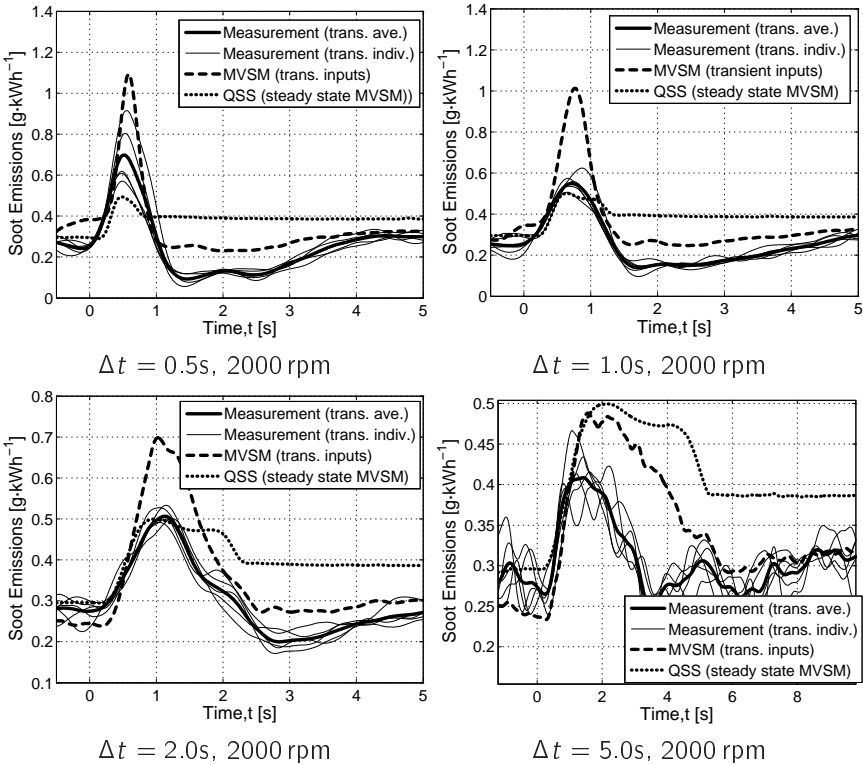
Figure 6.13: Comparison of the measured transient and calculated steady-state (QSS) and transient soot emissions during tip-in transients of different durations at 2000 rpm

meterization of the MVSM was first carried out for the reference fuel, followed by the by fuel two, whereby only those parameters thought to be influenced by the fuel were parameterized. When the MVSM was parameterized for the two measurement series from engine two, it became evident that an accurate measurement or estimate of the EGR and mean charge temperature (T_{ivc}) is required. These parameters were available for the parameter variation measurements from engine two, where the MVSM indicated that it was capable of reproducing the soot emissions in extreme regimes for which it was not parameterized.

From the sensitivity analysis, an extreme sensitivity of the MVSM to the mean

charge temperature and relative air-fuel ratio of the soot formation zone was noted. Both of these parameters are used in conjunction with the $\phi - T$ map to represent the chemistry of the soot formation process. Furthermore, it was seen that only formation relevant parameters have an influence on the calculated soot emissions and that the MVSM effectively considers only the soot formation process and that oxidation effects are poorly captured. From a sensitivity analysis of the number of operating points considered during model parameterization, it was determined that a minimum of approximately 50 operating points must be considered. This number is of course dependant on the engine considered and the number of degrees of freedom afforded by the ECU.

Several modifications to the MVSM were required to enable it to predict the soot emissions during transient operation. For the tip-in transients, it was shown that if the measured mean intake charge temperature is replaced with that estimated according to 4.15, the qualitative and quantitative performance of the MVSM is significantly improved. So that the MVSM exhibited adequate performance for the acceleration transients as well, it was necessary to correct the slow EGR temperature measurement.

While the MVSM was capable of reproducing the steady-state and, in part, transient soot emissions trends, there is considerable potential for its improvement. In particular, the MVSM must more satisfactorily consider the oxidation process, as this has been seen to play a strong role in the observed transient soot emissions. Furthermore, the influence of the boundary conditions (such as T_{ivc}) on the soot emissions must be better understood, and their influences adequately described by the MVSM. In the following chapter, several methods for improvement of the MVSM are presented.

Chapter 7

Conclusions and Outlook

This work outlines an investigation in which a mean value soot model was developed and validated against exhaust stream soot measurements for steady-state and transient operation. To further the understanding of the influences of the engine operating parameters, fuel properties, and transient engine operation, the exhaust stream measurements were complemented with in-cylinder pyrometry measurements. This chapter provides a summary of the major conclusions of this work, as well as guidelines for its continuation.

7.1 Exhaust Stream and In-Cylinder Soot Measurements

The exhaust-stream soot emissions were measured during steady-state and transient operation, in part to validate the MVSM, but also to gain further understanding of the influence of engine operation and fuel properties on the soot emissions. In addition, the in-cylinder soot concentration and temperature was measured using three-color pyrometry, so that the formation and oxidation processes could be directly characterized.

It was shown that features of the in-cylinder soot concentration quantified using the KL factor could be used to characterize the soot formation ($(KL)_{max}$) and oxidation processes (γ_{ox}), as well as cycle-specific, cylinder-out soot emissions ($(KL)_{end}$). The implemented miniature sensors could be used over multiple measurement campaigns, with minimal installation overhead, though particular attention to the validity of the calibration is required. During the tran-

sient measurements, window contamination was suspected (thereby resulting in an invalid pyrometer calibration), though this may potentially be avoided by increasing the window temperature. In a previous work [47] the windows were maintained at 600°C and no window contamination was noted, while here they were kept at 550°C to ensure longevity of the sensors and some contamination was noted.

From the exhaust stream and in-cylinder soot concentration measurements, the maximum in-cylinder soot concentration was seen to be largely a function of the engine load, while the large variations between operating points was found to be a result of changes in the oxidation process. For example, in the steady-state measurements, certain regions in the operating map were found to have higher exhaust-stream soot emissions due to low oxygen availability or low injection pressures and therefore less efficient localized fuel-air mixing. When these same regions were considered on the basis of the in-cylinder measurements, it was seen that the increased soot emissions could be attributed to decreases in the oxidized soot fraction, while the formation process remained relatively constant.

The in-cylinder soot measurements were further used to describe the reduced exhaust stream soot emissions seen for operation with a second fuel. The second fuel, which had a lower evaporation temperature, cetane number, and aromatic content, resulted in lower soot emissions for all considered operating points than for operation with the reference fuel. From a comparison of the combustion processes of the two fuels, a slightly higher fuel conversion rate was seen for fuel two, and in some instances a higher premixed combustion fraction. The most significant differences between the reference fuel and fuel two were noticed from the pyrometry measurements. It was seen that the lower soot emissions from fuel two were caused by an inhibition of soot formation due to the reduced aromatic content of the fuel and that the oxidation process was not significantly different between the two fuels.

From exhaust stream soot measurements during transient operation, it was seen that the soot emissions were increased during tip-in transients (compared to steady-state operation), while they remained relatively unchanged during acceleration transients. The increase in soot emissions during the tip-in transients was attributed to a short-term oxygen deficit characterized using the relative oxygen-fuel ratio. This deficit was caused by a rapid increase in the fuel quantity, coupled with a delayed increase in the charge pressure, and slow decrease in the EGR rate. This hypothesis was confirmed by the KL measurements that indicated that the increase in the exhaust stream emission

was caused by a weak oxidation. Additionally, the oxygen deficit was seen to decrease the maximum fuel conversion rates. Immediately after the tip-in transients, a short-term reduction in the soot emissions, compared to steady state operation, was observed. This was attributed to a short term reduction in the mean charge temperature, which is reduces the soot formation rate. No significant influence of the decreased mean charge temperature on the combustion process was observed.

In general, the soot emission trends observed during steady-state and transient operation could be described in terms of global engine parameters and multi-color pyrometry provided the possibility to consider the soot formation and oxidation processes directly. A combustion analysis based on cylinder pressure measurements indicated some differences between steady-state and transient operation, though they were much less pronounced as those observed using pyrometry.

7.2 Development and Validation of the MVSM

As presented in chapter 3, the MVSM developed in this investigation was to satisfy the following constraints:

1. be capable of realtime calculation of the cycle specific soot emissions ($\sim 20\,$ms per operating point)

2. use only engine parameters readily available from the ECU as model inputs

3. be capable of predicting the soot emissions during steady state *and* transient engine operation

4. be adaptable for implementation with different engines and fuels

The developed MVSM requires $\sim 10\,$ms per operating point to calculate the soot emissions. This is based on a Matlab .m implementation on a 3 GHz Windows XP PC.

With the exception of the EGR rate and mean intake charge temperature, all model inputs are available from the ECU for steady state operation. In this investigation the EGR rate was determined based on CO_2 measurements, though this method could be replaced with an adequate air path model. This would be particularly useful for transient engine operation, where the measurement of the EGR rate with sufficient temporal resolution is only possible with considerable overhead. In addition to the EGR rate, it was necessary to

estimate the mean charge temperature in the intake runner at intake valve closing, as this was found to have a profound impact on the performance of the MVSM during transient operation.

The performance of the MVSM was evaluated for steady state operation on two different engines with a total of three different fuels. From these steady-state validations, it was shown that the MVSM is capable of reproducing the qualitative and quantitative soot emission trends ($R^2 = 0.71...0.9$). This requires, however, that the 16 model parameters be determined for each engine and fuel combination, and that the EGR rate and mean charge temperature, as well as all other ECU parameters are well known. The parameterization of the model itself requires a minimum of approximately 50 operating points (for the considered engine). The extreme sensitivity of the MVSM to the mean charge temperature stems from the use of a $\phi - T$ map to describe the soot formation chemistry. Furthermore, the mean charge temperature is also assumed to influence the soot emission indirectly through influences on the combustion process through changes in the fuel evaporation, ignition delay, premixed combustion fraction and heat transfer.

If the model inputs are known with sufficient temporal resolution, the MVSM is also capable of reproducing the transient soot emissions, though with a lesser fidelity than for steady-state operation. Nonetheless, the MVSM was able to reproduce the short term increase in the soot emissions during tip-in transients, as well as the reduction immediately following the transient. For the calculation of the transient soot emissions, it was required to consider a weighted average of the steady-state and transient mean charge temperature to compensate for a slow EGR temperature measurement. From the steady state sensitivity analyses, it was seen that the MVSM is insensitive to soot oxidation relevant parameters. As the engine-out soot emissions are strongly dependant on the soot oxidation process, an improvement in the oxidation sub-model would likely result in an improvement in the calculated engine-out soot emissions during both steady state and transient operation.

While the 16 model parameters are used to represent physical processes or properties, the parameter values resulting from the parameterization should be considered as model parameters, and not as physical values. Due to the simplistic nature of the MVSM (compared to the "true" complexity of soot formation and oxidation) these parameters are also used to compensate for inadequacies of the MVSM in describing the physical processes, which are considered as lumped parameters.

7.3 Outlook

Although the MVSM presented in this work fulfills the requirements outlined above, there is still considerable potential for its further development - particularly for transient operation, though this requires a more detailed knowledge of the fundamental influences of transient operation on the soot emissions. Multicolor pyrometry has proven itself very useful in this investigation, though the characteristics of the implemented pyrometers are not yet fully understood. The possibility for future work in each of these areas is briefly outlined below.

7.3.1 Further Development of the MVSM

As mentioned above, the soot emissions calculated using the current version of the MVSM are largely described by the formation sub-model, while oxidation influences on the cylinder out emissions were not well captured. From the pyrometry investigations, however, it was found that the oxidation plays a very strong role in the steady-state and transient emissions. Thus, the MVSM performance can likely be improved by a better consideration of the oxidation process. This may be possible through a model parameterization during which not only the exhaust stream soot concentration, but also the in-cylinder soot concentration history is considered. This would allow the MVSM to be parameterized on the basis of measured characteristics of the formation and oxidation processes, rather than just their integrated net effect, as measured in the exhaust stream.

Currently the MVSM can consider the influence of one pilot injection, though it is assumed that soot is only formed during the main injection event. As the implementation of multiple injection (up to eight) strategies is becoming evermore relevant, a realistic implementation of the MVSM would require it to consider the influence of multiple injections. A potential starting point for the estimation of the thermodynamic state after each injection could be taken from [83]. In addition to multiple injection strategies, numerous modern production engines are equipped with cylinder pressure transducers. This would provide a more accurate estimate of the in-cylinder thermodynamic state and should thus be considered by the MVSM.

Though the MVSM was capable of reproducing the general soot emission trends during transient operation, it was not specifically developed or parameterized for transient engine operation. Once the most relevant physical processes, have been elucidated (potentially through experimental investigations, see below), the MVSM can be expanded to consider these processes

more directly. A parameterization specific to the transient components will likely be necessary based on transient measurements.

The manner in which the MVSM is parameterized has potential for improvement as well. In this investigation, "standard" steady-state operating points in which the majority of the engine operating parameters were specified by the ECU were considered. Through the consideration of a few relevant parameter variations, potentially selected using Design of Experiments, not only could the number of required measurements be reduced, but the quality of the parameterization could also be increased. Finally, all of the model parameters are currently determined on the basis of maximizing the agreement between the measured and calculated soot emissions, while it may be advantageous to consider other parameterization based on other measurements as well (such as the engine block or coolant temperature to account for the thermal behavior of the engine, for example).

7.3.2   Experimental Investigations

Considerable effort was placed into understanding the influence of transient engine operation on the soot emissions, though the effects are still only partially understood. Further work in this area would focus primarily on accurate, temporally resolved determination of all relevant engine parameters. The EGR rate determination likely holds the greatest potential for improvement, either through faster experimental methods (potentially optical) or through the use of a suitable EGR model. Recently a sensor suitable for EGR mass flow rate measurements in production engines has been introduced [26], which may provide an accurate EGR rate estimate during transient operation. Additionally, simultaneous cylinder pressure and pyrometry measurements in the same cylinder would remove the uncertainty introduced by either considering the processes in different cylinders or during different repetitions of the transient. Especially for investigations with multiple injection strategies, it would be necessary to sufficiently characterize the mass flow rates of the injectors.

This work identified the importance of the intake charge temperature for both the calculated and measured soot emissions, in particular during transient operation. While it is known that the calculated soot emissions are influenced through the $\Phi - T$ map, the mechanistic influence of T_{ivc} on the combustion and soot formation and oxidation are not yet understood. To further investigate its effect a systematic variation of the intake charge temperature (using the intercooler, for example) during steady state operation, coupled

with pyrometery and a thermodynamic analysis could be used. Furthermore, to better characterize the process during transient operation, thermocouples with a faster response times ($\tau \ll 1\,\mathrm{s}$) could be implemented.

7.3.3 Three Color Pyrometry

The miniature pyrometers used in this investigation proved invaluable in understanding the observed exhaust stream soot emission phenomena. However, there are several topics which deserve further consideration:

- While the calibration procedure of the pyrometers has been well defined [59], the validity of the calibration after changes in the effective field of view of the sensor, as well as through contamination, should be considered. In general, a systematic investigation of the calibration and potentially a correction method based on the agreement of the three temperatures and KL factors is required.

- As window contamination will influence the calibration and hence the performance of the pyrometers, the contamination must be minimized. As mentioned above, one potential solution is an increase in the window temperature, though this negatively influences the longevity of the sensor. Thus some means of reducing or compensating for window contamination is needed.

- One very useful parameter available from pyrometry is $(KL)_{end}$ which characterizes the cycle-specific, cylinder-out soot emissions. Its determination however, is very susceptible to reduced signal-to-noise ratios. Ideally the signal-to-noise ratio of the implemented transducers should be increased, or a robust algorithm for the determination of $(KL)_{end}$ should be determined. The increased sensitivity may prove to be particularly relevant when new, alternative combustion processes with low temperatures are considered, as the radiation intensity will be considerably lower.

- This work considered $(KL)_{max}$ and introduced γ_{ox} to describe the soot formation and oxidation processes, respectively. To investigate their validity for the representation of these processes, a comparison with other in-cylinder methods would be beneficial. Suitable methodologies here may include cylinder gas sampling or other optical techniques such as laser induced incandescence (LII, [15]). Furthermore, a comparison with spatially resolved in-cylinder measurements (for example using two

dimensional pyrometry) would elucidate the influence of spatial inho-
mogeneities on the integral measurement afforded by the implemented
pyrometers.

Bibliography

[1] D. Ajtay and M. Weilenmann. Compensation of the exhaust gas transport dynamics for accurate instantaneous emission measurements. *Environmental Science & Technology*, 38(19):5141–5148, 2004.

[2] D. E. Ajtay. *Modal pollutant emissions model of diesel and gasoline engines*. PhD thesis, ETH Zurich, 2005.

[3] K. Akihama, Y. Takatori, K. Inagaki, S. Sasaki, and A. Dean. Mechanism of the Smokeless Rich Diesel Combustion by Reducing Temperature. *SAE 2001-01-0655*, 2001.

[4] E. Alfieri. *Emissions-Controlled Diesel Engine*. PhD thesis, ETH Zurich, 2009. Diss. 18214.

[5] E. Alfieri, A. Amstutz, L. Guzzella, and A. Schilling. Emissionsgeregelte Dieselmotoren. *Motortechnische Zeitschrift*, 68(11):982–989, 2007.

[6] C. A. Amann and D. C. Siegla. Diesel Particulates; What They Are and Why. *Aerosol Science And Technology*, 1(1):73 – 101, 1981.

[7] C. Barba. *Erarbeitung von Verbrennungskennwerten aus Indizierdaten zur verbesserten Prognose und rechnerischen Simulation des Verbrennungsablaufes bei Pkw-DE-Dieselmotoren mit Common-Rail-Einspritzung*. PhD thesis, ETH Zürich, 2001.

[8] J. Bayer and D. E. Foster. Zero-Dimensional Soot Modeling. *SAE 2003-01-1070*, 2003.

[9] H. A. Beck, R. Niessner, and C. Haisch. Development and characterization of a mobile photoacoustic sensor for on-line soot emission monitoring in diesel exhaust gas. *Analytical And Bioanalytical Chemistry*, 375(8):1136–1143, 2003.

[10] P. Belardini, C. Bertoli, A. Ciajolo, A. D'Anna, and N. Del Giacomo. Three Dimensional Calculations of DI Diesel Engine Combustion and Comparison With in Cylinder Sampling Valve Data. *SAE 922225*, 1992.

[11] A. G. Bell. On the Production and Reproduction of Sound by Light. *American Journal of Sciences*, 20(118):305–324, 1880.

[12] A. G. Bertola. *Technologies for lowest NOx and particulate emissions in DI-diesel engine combustion influence of injection parameters, EGR and fuel composition*. PhD thesis, ETH Zurich, 2004.

[13] H. Bockhorn. *Soot formation in combustion: mechanisms and models*. Springer-Verlag, Berlin etc., 1994.

[14] C. F. Bohren and D. R. Huffman. *Absorption and scattering of light by small particles*. Wiley, 1998.

[15] A. Boiarciuc, F. Foucher, C. Mounaïm-Rousselle, and O. Pajot. Estimate Measurement of Soot Diameter and Volume Fraction Inside the Bowl of a Direct-Injection-Compression-Ignition Engine: Effect of the Exhaust Gas Recirculation. *Combustion Science And Technology*, 179(8):1631 – 1648, 2007.

[16] I. Brahma, C. J. Rutland, D. E. Foster, and Y. He. A New Approach to System Level Soot Modeling. *SAE 2005-01-1122*, 2005.

[17] B. Brechbühl, M. Schnepf, R. Sonntag, and P. Wolfer. Neue Möglichkeiten der Druckindizeirung in Verbrennungsmotoren ohne seperate Messbohrung. In *4. Internationales Sypmosium für Verbrennungsdiagnostik*, pages 49–60, Baden-Baden, 2000.

[18] Bundesamt für Umwelt, Wald und Landschaft. Feinstaub macht Krank. Technical report, 2005.

[19] A. Burcat and B. Ruscic. Third Millennium Ideal Gas and Condensed Phase Thermochemical Database for Combustion with Updates from Active Thermochemical Tables. Technical Report TAE960, 2005.

[20] C. Burkhardt and M. Bargende. Thermoschokkorrektur bei Druckindizierungen mit Zünd- und Glühkerzenadaptern. *Motortechnische Zeitschrift*, 56(12):736–741, 1995.

[21] H. Burtscher. Physical characterization of particulate emissions from diesel engines: a review. *Journal Of Aerosol Science*, 36(7):896–932, 2005.

[22] M. Chan, D. Sudhakar, and R. D. Reitz. Modeling Multiple Injection and EGR Effects on Diesel Engine Emissions. *SAE 972864*, 1997.

[23] R. Christian, F. Knopf, A. Jaschek, and W. Schindler. Eine neue Messmethodik der Bosch-Zahl mit erhöhter Empfindlichkeit. *Motortechnische Zeitschrift*, 54:16–22, 1993.

[24] J. Dec. A conceptual model of DI diesel combustion based on laser-sheet imaging. *SAE 970873*, 1997.

[25] Dekati Limited. *Dekati Fine Particle Sampler: User Manual*. 2004.

[26] H. Dismon, K. Grimm, A. Tönnesmann, S. Nigrin, K. Wienand, and M. Muziol. Ceramic Hot Film Sensor for Exhaust Gas Mass Flow Measurements in Automotive Applications. In *Aachen Colloquium*, pages 1245–1270, Aachen, 2008. VDI.

[27] D. W. Dockery, C. A. Pope, X. P. Xu, J. D. Spengler, J. H. Ware, M. E. Fay, B. G. Ferris, and F. E. Speizer. An Association between Air Pollution and Mortality in 6 United States Cities. *New England Journal of Medicine*, 329(24):1753–1759, 1993.

[28] G. D'Urbano and A. Mayer. Filterliste BAFU/Suva. Geprüfte und erprobte Partikelfilter-Systeme für die Nachrüstung von Dieselmotoren. Technical report, Bundesamt für Umwelt, 2007.

[29] European Community, 1999. Directive 1999/96/EC.

[30] F. Ferretti. Transient EGR-Model for Diesel Engines. Technical report, ETH Zürich, IMRT, 2007.

[31] M. Frenklach. Reaction mechanism of soot formation in flames. *Physical Chemistry Chemical Physics*, 4(11):2028–2037, 2002.

[32] M. Frenklach and H. Wang. Detailed Modeling of Soot Particle Nucleation and Growth. In *Twenty Third Symposium (International) on Combustion*, pages 1559–1566. The Combustion Institute, 1990.

[33] A. Fusco, A. Knox-Kelecy, and D. E. Foster. Application of a Phenom-enological Soot Model to Diesel Engine Combustion. In *COMODIA*, pages 571–576, 1994.

[34] B. Giechaskiel, P. Dilara, and J. Andersson. Particle Measurement Programme (PMP) Light-Duty Inter-Laboratory Exercise: Repeatabil-ity and Reproducibility of the Particle Number Method. *Aerosol Science And Technology*, 42(7):528 – 543, 2008.

[35] I. Glassman. *Combustion*. Academic Press, San Diego, 3rd edition, 1996.

[36] J. R. Hagena, Z. S. Filipi, and D. N. Assanis. Transient Diesel Emissions: Analysis of Engine Operation During a Tip-In. *SAE 2006-01-1151*, 2006.

[37] J. Haywood and O. Boucher. Estimates of the direct and indirect ra-diative forcing due to tropospheric aerosols: A review. *Reviews of Geo-physics*, 38(4):513–543, 2000.

[38] J. B. Heywood. *Internal combustion engine fundamentals*. McGraw-Hill, New York, international edition, 1988.

[39] H. Hiroyasu and T. Kadota. Development and Use of a Spray Com-bustion Modeling to Predict Diesel Engine Efficiency and Pollutant Emissions (Part 1, Comubstion Modelling). *Bulletin of the JSME*, 26(214):569–575, 1983.

[40] S. Hong, M. S. Wooldridge, H. G. Im, D. N. Assanis, and H. Pitsch. Development and application of a comprehensive soot model for 3D CFD reacting flow studies in a diesel engine. *Combustion and Flame*, 143(1-2):11, 2005.

[41] H. C. Hottel and F. P. Broughton. Determination of True Temperature and Total Radiation from Luminous Gas Flames. *Ind. Eng. Chem. Anal. Ed.*, 4(2):166–175, 1932.

[42] ISO. Measurement apparatus for smoke from engines operating under steady-state conditions., 1998. Standard No. 10054.

[43] Y. J. Kaufman, D. Tanre, and O. Boucher. A satellite view of aerosols in the climate system. *Nature*, 419(6903):215–223, 2002.

[44] A. Kazakov and D. E. Foster. Modeling of Soot Formation during DI Diesel Combustion Using a Multi-Step Phenomenological Model. *SAE 982463*, 1998.

[45] J. Keskinen, K. Pietarinen, and M. Lehtimaki. Electrical Low-Pressure Impactor. *Journal Of Aerosol Science*, 23(4):353–360, 1992.

[46] P. Kirchen, S. Walther, P. Obrecht, K. Boulouchos, D. Karst, and C. Cavalloni. Measurement of the Instantaneous In-Cylinder Soot Temperature and Concentration in a Multi-Cylinder Engine. In *11th ETH Conference on Combustion Generated Nanoparticles*, Zurich, Switzerland, 2007.

[47] P. Kirchen, S. Walther, P. Obrecht, K. Boulouchos, D. Karst, and C. Cavalloni. Correlation and Analyis of In-Cylinder and Engine-Out Soot Emission Measurements from a Multi-Cylinder Diesel Engine. In *8. Internationales Stuttgarter Symposium*, volume 2, pages 129–145, Stuttgart, Germany, 2008.

[48] P. Kirchen, S. Walther, P. Obrecht, K. Boulouchos, D. Karst, and C. Cavalloni. Correlation and Analysis of In-Cylinder and Engine-Out Soot Emission Measurements from a Multi-Cylinder Diesel Engine. In *8. Internationales Stuttgarter Symposium*, volume 2, pages 129–145, Stuttgart, Germany, 2008.

[49] D. B. Kittelson. Engines and nanoparticles: A review. *Journal Of Aerosol Science*, 29(5-6):575–588, 1998.

[50] R. Klingmann and H. Brüggemann. Der neue Vierzylinder-Dieselmotor OM611 mit Common-Rail-Einspritzung Teil 1: Motorkonstruktion und mechanischer Aufbau. *Motortechnische Zeitschrift*, 58(11):652–659, 1997.

[51] W. Koch, H. Lödding, W. Mölter, and F. Munzinger. Verdünnungssystem für die Messung hochkonzentrierter Aerosole mit optischen Partikelzählern. *Staub - Reinhaltung der Luft*, 48:341–344, 1988.

[52] P. Kožuch. *Ein phänomenologisches Modell zur kombinierten Stickoxid- und Russberechnung bei direkteinspritzenden Dieselmotoren*. PhD thesis, Universität Stuttgart, 2004.

[53] P. Kožuch, M. Grill, and M. Bargende. Ein neuer Ansatz zur kombinierten Stickoxid- und Russberechnung bei DI-Dieselmotoren. In M. Bargende and U. Essers, editors, *Dieselmotorentechnik*, Ostfildern, 2004.

[54] M. Kraft. Towards a Detailed Soot Model for Internal Combustion Engines. In *12th ETH Conference on Combustion Generated Nanoparticles*, Zürich, 2008.

[55] W. G. Kreyling, M. Semmler-Behnke, and W. Moller. Health implications of nanoparticles. *Journal of Nanoparticle Research*, 8(5):543–562, 2006.

[56] N. Kuenzli. Traffic Related Pollution: Risk Factor for the Development of Cardiovascular Diseases? In *11th ETH Conference on Combustion Generated Nanoparticles*, 2007.

[57] S. Kunte, A. Bertola, and K. Boulouchos. Potenzial moderner Verbrennungsmotoren zur Partikelminderung. In *Minimierung von Partikelemissionen*. Expert Verlag, 2005.

[58] S. Kunte, A. Bertola, P. Obrecht, and K. Boulouchos. Temporal soot evolution and diesel engine combustion: influence of fuel composition, injection parameters, and exhaust gas recirculation. *International Journal of Engine Research*, 7:459, 2006.

[59] S. Kunte, P. Obrecht, B. Ineichen, and K. Boulouchos. KTI Abschluss Bericht: Industrietaugliche Lichtwellenleitersonden-Messkette zur Bestimmung der Russmenge, Russtemperatur und des Zündverzugs am Verbrennungsmotor. Technical report, 2005.

[60] N. Ladommatos, P. Rubenstein, K. Harrison, Z. Xiao, and H. Zhao. The effect of aromatic hydrocarbons on soot formation in laminar diffusion flames and in a diesel engine. *Journal Of The Institute Of Energy*, 70(484):84–94, 1997.

[61] U. Lehmann, V. Niemela, and M. Mohr. New method for time-resolved diesel engine exhaust particle mass measurement. *Environmental Science & Technology*, 38(21):5704–5711, 2004.

[62] K. M. Leung, R. P. Lindstedt, and W. P. Jones. A simplified reaction mechanism for soot formation in nonpremixed flames. *Combustion And Flame*, 87(3-4):289–305, 1991.

[63] X. Li. *Soot Formation and Oxidation in DI Diesel Engines*. PhD thesis, University of Toronto, 1995.

[64] X. Li and J. Wallace. A Phenomenological Model for Soot Formation and Oxidation in Direct-Injection Diesel Engines. *SAE 952428*, 1995.

[65] J. Lyyränen, J. Jokiniemi, E. I. Kauppinen, and J. Joutsensaari. Aerosol Characterisation in Medium-Speed Diesel Engines Operating with Heavy Fuel Oils. *Journal Of Aerosol Science*, 30(6):771–784, 1999.

[66] G. Maag and M. Zanini. Diesel Engine Soot Emissions Measurement and Calculation. Technical report, ETH Zurich, 2006.

[67] S. R. Magari, R. Hauser, J. Schwartz, P. L. Williams, T. J. Smith, and D. C. Christiani. Association of heart rate variability with occupational and environmental exposure to particulate air pollution. *Circulation*, 104(9):986–991, 2001.

[68] B. F. Magnussen and B. H. Hjertager. On mathematical modeling of turbulent combustion with special emphasis on soot formation and combustion. *Symposium (International) on Combustion*, 16(1):719–729, 1977.

[69] M. M. Maricq. Nanoparticles in the Exhaust of Internal Combustion Engines. In *SAE - ICE2007: 8th International Conference on Engines for Automobiles*, Capri, Italy, 2007.

[70] U. Mathis. Effect of Organic Vapour in Diesel Exhaust on Nanoparticle Formation. In *7th ETH Conference on Combustion Generated Nanoparticles*, Zurich, 2003.

[71] T. Mathworks. Matlab, 2007. Version 7.4.0 (R2007a).

[72] Y. Matsui, T. Kamimoto, and S. Matsuoka. A Study on the Application of the Two-Color Method to the Measurement of Flame Temperature and Soot Concentration in Diesel Engines. *SAE 800970*, 1980.

[73] C. Mutsch. Korrelation zwischen innerzylindrisch und im Abgas gemessenen Russemissionen. Technical report, ETH Zürich, 2008.

[74] J. Nagle and R. F. Strickland-Constable. Oxidation of Carbon Between 1000-2000°C. In *Fifth Conference on Carbon*, pages 154–164, 1961.

[75] P. Obrecht. WEG - Benutzerhandbuch und Programdokumentation, Teil 3. Technical report, ETH Zurich, 2004.

[76] P. Obrecht. WEG - Verbrennungsanalyse: Berechnung des Wärmeentwicklungsgesetzes. Version 15, 2008.

[77] M. Patterson, S. C. Kong, G. Hampson, and R. D. Reitz. Modeling the Effects of Fuel Injection Characteristics on Diesel Engine Soot and NOx Emissions. *SAE 940523*, 1994.

[78] A. Peters, D. W. Dockery, J. E. Muller, and M. A. Mittleman. Increased particulate air pollution and the triggering of myocardial infarction. *Circulation*, 103(23):2810–2815, 2001.

[79] A. Peters and W. Pütz. Der neue Vierzylinder-Dieselmotor OM611 mit Common-Rail-Einspritzung Teil 2: Verbrennung und Motormanagement. *Motortechnische Zeitschrift*, 58(12):760–767, 1997.

[80] A. Petzold and R. Niessner. Photoacoustic soot sensor for in-situ black carbon monitoring. *Applied Physics B: Lasers and Optics*, 63(2):191–197, 1996.

[81] H. Pohlheim. *Evolutionäre Algorithmen: Verfahren, Operatoren und Hinweise für die Praxis*. Springer, Berlin, 2000.

[82] K. Reavell, T. Hands, and N. Collings. A Fast Response Particulate Spectrometer for Combustion Aerosols. *SAE 2002-01-2714*, 2002.

[83] H. Reinhardt and M. Bargende. Modelliuerung des Zünderverzugs bei Mehrfacheinspritzungen aufgeladener Dieselmotoren mit Direkteinspritzung innerhalb der thermodynamischen Prozessrechnung. In *Informationstagung Motoren*, volume R541, pages 59–81, Frankfurt am Main, 2008.

[84] Robert Bosch GmbH. *Diesel-Engine Management*. John Wiley & Sons, 4th edition, 2005.

[85] E. Roseel, R. Sierens, and R. Baert. Evaluating Piezoelectric Transducer Response to Thermal Shock from In-Cylinder Pressure Data. *SAE 1999-01-0935*, 1999.

[86] A. Schilling. *Model-Based Detection and Isolation of Faults in the Air and Fuel Paths of Common-Rail DI Diesel Engines Equipped with a Lambda and a Nitrogen Oxides Sensor*. PhD thesis, ETH Zurich, 2008. Diss. 17764.

[87] W. Schindler, C. Haisch, H. A. Beck, R. Niessner, E. Jacob, and D. Rothe. A Photoacoustic Sensor System for Time Resolved Quantification of Diesel Soot Emissions. *SAE 2004-01-0968*, 2004.

[88] R. Schubiger, K. Boulouchos, and M. Eberle. Russbildung und Oxidation bei der dieselmotorischen Verbrennung. *Motortechnische Zeitschrift*, 5(63):342–353, 2002.

[89] R. A. Schubiger. *Untersuchungen zur Russbildung und -oxidation in der dieselmotorischen Verbrennung Thermodynamische Kenngrössen, Verbrennungsanalyse und Mehrfarbenendoskopie*. PhD thesis, ETH Zurich, 2001.

[90] P. E. Schwarze, J. Ovrevik, M. Lag, M. Refsnes, P. Nafstad, R. B. Hetland, and E. Dybing. Particulate matter properties and health effects: consistency of epidemiological and toxicological studies. *Human & Experimental Toxicology*, 25(10):559–579, 2006.

[91] D. Siebers and Higgins. Flame Lift-Off on Direct Injection Diesl Sprays Under Quiescent Conditions. *SAE 2001-01-0530*, 2001.

[92] O. I. Smith. Fundamentals Of Soot Formation In Flames With Application To Diesel-Engine Particulate-Emissions. *Progress In Energy And Combustion Science*, 7(4):275–291, 1981.

[93] H. Stebler. *Luft- und brennstoffseitige Massnahmen zur internen NOx Reduktion von schnell laufenden direkt eigespritzten Dieselmotoren*. PhD thesis, ETH Zurich, 1998.

[94] W. Steiger and C. Kohnen. New Combustion System Based on a New Fuel Specification. In *27th International Vienna Motor Symposium*, Vienna, 2006.

[95] W. Steiger, U. Stolte, I. Scholz, and S. Schmerbeck. Das CCS-Brennverfahren von Volkswagen. *Motortechnische Zeitschrift*, 69(3):184–192, 2008.

[96] F. Tao, V. I. Golovitchev, and J. Chomiak. A phenomenological model for the prediction of soot formation in diesel spray combustion. *Combustion and Flame*, 136:270, 2004.

[97] F. Tao, Y. Liu, B. Rempelewert, D. E. Foster, R. D. Reitz, D. Choi, and P. Miles. Modeling the Effects of EGR and Injection Pressure on Soot Formation in a High-Speed Direct Injection (HSDI) Diesel Engine Using a Multi-Step Phenomenological Soot Model. *SAE 2005-01-0121*, 2005.

[98] D. R. Tree and K. I. Svensson. Soot processes in compression ignition engines. *Progress In Energy And Combustion Science*, 33(3):272–309, 2007.

[99] Verein Deutscher Ingenieure. Chemical Analysis of Elemental Carbon by Extraction and Thermal Desorption of Organic Carbon, 1996. VDI 2465.

[100] S. C. Wang and R. C. Flagan. Scanning Electrical Mobility Spectrometer. *Aerosol Science And Technology*, 13(2):230 − 240, 1990.

[101] J. Warnatz, U. Maas, and R. W. Dibble. *Combustion: Physical and Chemical Fundamentals, Modeling and Simulation, Experiments, Pollutant Formation*. Springer, Berlin, 3rd edition, 2001.

[102] M. Warth. Vorausberechnung von Brennverlauf, NO- und Russemissionen beim Dieselmotoroptimierung und Validierung eines neuen Ansatzes. In *9. Tagung der Arbeitsprozess des Verbrennungsmotors*, pages 115–133, Graz, Österreich, 2003.

[103] M. Warth. *Comparative Investigation of Mathematical Methods for Modeling and Optimization of Common-Rail DI Diesel Engines*. PhD thesis, ETH Zurich, 2006.

[104] M. Warth, P. Obrecht, A. Bertola, and K. Boulouchos. Predictive Phenomenological C.I. Combustion Modeling Optimization on the Basis of Bio-Inspired Algorithms. *SAE 2005-01-1119*, 2005.

[105] M. Weigl. Partikel Sensorik für Motorregelung und On-Board-Diagnose. In *8. Internationales Stuttgarter Symposium*, 2008.

[106] S. Wenzel. *Modellierung der Russ- und NOx Emissionen des Dieselmotors*. PhD thesis, Otto-von-Guericke Universität, 2006.

[107] R. Wijetunge, C. Brace, J. Hawley, N. Vaughan, R. Horrocks, and G. Bird. Dynamic Behaviour of a High Speed Direct Injection Diesel Engine. *SAE 1999-01-0829*, 1999.

[108] E. Winklhofer, A. Hirsch, T. Leifert, and M. Rzehorska. Crank Angle Resolved Flame Measurements in HSDI Diesel Engines. In *7th International Symposium on Internal Combustion Diagnostics*, Baden-Baden, Germany, 2006. AVL.

[109] www.metoffice.gov.uk. "Met Office: The Great Smog of 1952". Retrieved on 2008-08-17.

[110] J. Yan and G. Borman. Analysis and In-Cylinder Measurement of Particulate Radiant Emissions and Temperature in a Direct Injection Diesel Engine. *SAE 881315*, 1988.

[111] H. Zhao and N. Ladommatos. Optical diagnostics for soot and temperature measurement in diesel engines. *Progress In Energy And Combustion Science*, 24(3):221–255, 1998.

[112] H. Zhao and N. Ladommatos. *Engine Combustion Instrumentation and Diagnostics*. Society of Automotive Engineers, Warrendale, 2001.

Nomenclature

Abbreviations

FID	Flame Ionization Detector
MSS	Micro Soot Sensor
MVSM	Mean Value Soot Model
NDIR	Non-Dispersive Infrared
PASS	Photo-Acoustic Soot Sensor
QSS	Quasi Steady-State
RH	Relative Humidity

Indices

*	Representative (cycle average) parameter
adb	Adiabatic
air	Air
app	Apparent value
b	Blackbody property
$comb$	Combustion
cyl	Cylinder bulk property
d	Dry measurement
$diff$	Diffusion combustion process
$diss$	Turbulence dissipation parameter
$drop$	Droplet
EGR	Recirculated exhaust gases
est	Estimated parameter

$evap$	Evaporation
ex	Exhaust stream
f	Fuel
f, liq	Liquid fuel
f, v	Fuel vapor
$form$	Formation
fr	Fresh air
ign	Ignition
inj	Injection parameter
IVC	Intake valve closing
$main$	Main injection
mix	Mixture property
$nozzle$	Fuel injector nozzle
O_2	Oxygen
ox	Oxidation
$pilot$	Pilot injection
$pilot, comb$	Pilot combustion
pm	Piston motion
ref	Reference property
s	Soot
SOI	Start of injection
tdc	Top Dead Center
w	Wet measurement

Variables

$[EC]$	Elementary carbon concentration [mg/m^3]
$\bar{\delta}^2$	Mean relative square error [-]
$\bar{v}_p$	Mean piston speed [m/s]
β	Empirical evaporation coefficient [m^2/s]
$\dot{m}$	Mass flow rate [kg/s]
κ	Ratio of the specific heat capacities c_p/c_v [-]

λ	Relative air-fuel ratio [-]
λ	Wavelength [nm]
λ_{diff}	Relative air-fuel ratio relevant during diffusion combustion [-]
λ_{form}	Relative air fuel ratio in soot formation zone [-]
ω	Rotational speed [rpm]
ρ	Density [kg/m^3]
τ	Duration [s]
τ_{char}	Characteristic mixing time [s]
ε	Emissivity [-]
φ_{50}	Crank angle for 50% fuel conversion [CA]
φ_{diff}	Representative crank angle for diffusion combustion [°CA]
ξ_{diff}	Diffusion combustion fraction[-]
A	Area [m^2]
A_{form}	Formation scaling factor [-]
A_{ox}	Oxidation scaling factor [-]
C_{comb}	Combustion generated turbulence scaling factor [-]
C_{diff}	Diffusion combustion duration scaling factor [-]
$C_{inj,disp}$	Turbulent kinetic energy dissipation scaling factor [-]
$C_{inj,kin}$	Turbulent kinetic energy scaling factor [-]
C_{inj}	Injection turbulence scaling factor [-]
C_{O_2}	Oxygen quantity scaling factor 0...1 [-]
C_{pm}	Piston motion turbulence scaling factor [-]
c_p	Specific heat capacity at a constant pressure [kJ/kg/K]
CN	Cetane Number [-]
d	Diameter [m]
E_a	Activation energy [kJ/kg]
EGR	Exhaust gas recirculation rate [-]
FSN	Filter Smoke Number [-]]
i	Radiation intensity [W/sr/m^2]

K	Absorption Coefficient $[m^{-1}]$
$k(t)$	Instantaneous turbulent kinetic energy $[m^2/s^2]$
$k^*_{inj,gen}$	Effective turbulent kinetic energy generated through injection $[m^2/s^2]$
L	Optical Length [m]
l	Characteristic length scale [m]
LHV	Lower Heating Value [MJ/kg]
M	Molar mass [g/mol]
m	Mass [kg]
M_e	Braking moment [Nm]
$m_{air,st}$	Stoichiometric air mass $[kg_air/kg_fuel]$
n	Number of moles [-]
n_1	Formation pressure exponent [-]
n_2	Injection timing correction exponent [-]
n_3	Injection pressure correction exponent [-]
n_4	Oxygen partial pressure exponent [-]
n_e	Engine speed [rpm]
n_{nozzle}	Number of injection nozzles per injector [-]
n_{op}	Number of operating points [-]
p	Pressure, partial pressure [bar]
R_u	Universal gas constant, 8.314 [kJ/kmol/K]
T	Temperature [K]
t	Time[s]
$T_{A,ox}$	Oxidation activation temperature [K]
T_A	Activation temperature [K]
$T_{min,ox}$	Minimum temperature for soot oxidation [K]
u	Velocity [m/s]
u'	Turbulence intensity [m/s]
V	Volume $[m^3]$
X_i	Mole fraction of substance i [-]

Appendix A

Summary of Measurements

A.1   OM611 Operating Points

Listed in the following tables is a summary of the operating points measured on the OM611, with the reference fuel and fuel two.

12.5pt

	ω rpm	M_e Nm	λ -	λ_{ox} -	EGR -	p_{rail} bar	SOI_{main} CAD bTDC	SOI_p CAD bTDC	τ_{main} μs	τ_p μs
					OM611 - Reference Fuel - 1 of 3					
pt1	1000	31.03	2.172	3.038	0.515	293.5	-0.492	9.598	606.5	323
pt2	999.4	67.69	1.664	2.274	0.318	328.5	0.258	10.37	785.7	306.6
pt3	999.8	100.6	1.586	2.201	0.096	364.9	1.312	11.42	874.5	280.7
pt4	1000	120	1.509	2.019	0.027	403.7	2.297	12.41	914	258.7
pt5	1248	33.81	2.443	3.876	0.408	391.5	-0.021	12.85	481.9	261.1
pt6	1248	68.77	1.698	2.388	0.326	415.5	0.102	12.97	639.7	255.1
pt7	1249	102.7	1.55	2.183	0.175	475.7	1.219	14.09	712	237
pt8	1248	138.6	1.454	1.973	0.057	575.5	2.273	15.14	753.7	210.9
pt9	1249	151.8	1.411	1.908	0.031	621.4	2.787	15.66	762.3	200.2
pt10	1498	35.28	2.445	4.267	0.375	442.4	0.308	15.97	443.6	244.5
pt11	1498	69.91	1.695	2.485	0.319	468.1	0.269	15.91	596.4	240.5
pt12	1498	102.6	1.489	2.135	0.215	541.7	1.338	17.01	660.6	221.4
pt13	1499	136.9	1.359	1.845	0.123	649.7	2.482	18.14	696.5	194.9
pt14	1499	154.8	1.438	1.912	0.069	685.9	2.742	18.4	722.4	193.5
pt15	1748	34.14	2.676	4.585	0.332	480.2	0.553	18.99	419.9	235.5
pt16	1748	69.55	1.858	2.681	0.278	511.8	0.773	19.22	566	229.8
pt17	1749	103.4	1.603	2.156	0.205	601.7	1.969	20.42	615.2	206.6
pt18	1749	137.1	1.435	1.894	0.161	696.5	3.046	21.5	656.1	192.3
pt19	1749	154.9	1.458	1.88	0.139	743.4	3.563	22.01	684.7	188.9
pt20	1999	34.02	2.703	4.825	0.315	501.8	0.826	22.11	409.2	228.9
pt21	1999	69.25	1.889	2.777	0.267	536.4	1.269	22.54	545.6	222.7
pt22	1999	103.7	1.604	2.214	0.202	630	2.414	23.69	592	201.1
pt23	1998	137	1.47	1.934	0.188	750.1	3.803	25.09	626.3	188.4
pt24	1999	169.9	1.504	1.906	0.139	819.9	5.439	26.71	690.8	185.4
pt25	1999	191.7	1.659	2.051	0.055	846.1	6.198	27.48	789.3	184.7
pt26	2249	34.16	2.838	5.089	0.275	514.4	2.418	26.45	397.8	225.5
pt27	2249	69.18	1.979	2.901	0.229	567.1	2.686	26.71	517.4	214.4
pt28	2249	102.6	1.665	2.315	0.171	663.4	3.692	27.72	569.5	196.6
pt29	2249	137	1.511	2.027	0.161	770	4.999	29.03	609.7	186.4
pt30	2249	170.8	1.514	1.917	0.155	829.6	6.689	30.71	698.3	185.4
pt31	2249	188.5	1.86	2.201	0.007	859.2	7.179	31.22	770.4	184.5
pt32	2498	34.7	2.828	5.067	0.28	540.9	3.918	30.67	390.9	219.7
pt33	2498	68.95	2.074	3.005	0.239	611.9	4.227	30.99	492.3	203.3
pt34	2497	102	1.713	2.421	0.194	707	5.183	31.93	548	192.3
pt35	2497	135.9	1.58	2.118	0.193	815.6	6.445	33.2	599.2	185.4
pt36	2498	170.3	1.801	2.296	0.064	850.2	7.614	34.37	682.2	184.9
pt37	2498	189.8	1.896	2.265	0.005	890.6	7.945	34.7	767.4	184.5
pt38	2748	33.63	3.058	5.002	0.227	586.6	5.386	34.89	375	206.8
pt39	2746	68.35	2.173	3.356	0.2	662	5.82	35.31	470.5	194.5
pt40	2748	102.1	1.835	2.55	0.143	749.2	6.917	36.43	528.7	188.5
pt41	2747	134.8	1.702	2.244	0.157	825.3	7.875	0	608.7	0
pt42	2749	170.4	2.069	2.435	0.006	887.6	8.442	0	710.9	0
pt43	2748	187.3	1.959	2.346	0.006	931.4	8.645	0	767.2	0
pt44	2998	34.27	3.201	5.173	0.184	618	5.618	37.9	374.7	200.4
pt45	2999	68.58	2.326	3.475	0.176	691.1	6.65	38.93	456.3	193
pt46	3001	102.6	2.005	2.729	0.116	783.2	7.952	40.24	518	186.4
pt47	2999	138.9	2.046	2.696	0.052	857.3	9.041	0	604.1	0
pt48	2999	168	2.087	2.486	0.008	954.1	9.56	0	685.2	0
pt49	3250	35.57	3.812	5.611	0.002	654.5	6.23	41.29	377.2	194.9
pt50	3249	68.12	2.809	3.923	0.002	720.2	7.307	42.35	445.8	191.1
pt51	3249	102.8	2.436	3.078	0.002	819.1	8.805	43.84	517.2	185.4
pt52	3250	135.2	2.246	2.775	0.006	883.4	10.17	0	596	0
pt53	3249	169	2.068	2.376	0.008	1047	10.85	0	674.5	0
ref1	2999	137.8	2.326	2.893	0.01	854.5	9.01	0	601.5	0
ref2	3000	136.1	2.148	2.74	0.018	853.1	8.973	0	599.6	0
ref3	2999	136.7	2.073	2.684	0.021	849	8.97	0	599.6	0
ref4	2999	137.6	2.055	2.626	0.005	858.2	9.033	0	605.3	0

Table A.1: **OM611 with reference fuel:** steady state operating parameters

	p_{amb} bar	p_{im} bar	p_{em} bar	p_{exh} bar	T_{amb} K	T_{im} K	T_{em} K	T_{exh} K	T_{egr} K	T^*_{ivc} K	m_{air} kg/s	m_f g	m_{main} g
						OM611 - Reference Fuel - 2 of 3							
pt1	0.972	0.966	1.024	0.976	298.1	351.1	497.1	530.3	433.5	353.8	0.009	0.008	0.006
pt2	0.972	0.987	1.057	0.978	297.9	340.2	575.3	554.1	442	332.2	0.011	0.013	0.012
pt3	0.972	1.026	1.112	0.982	297.7	317.3	625.2	603.9	390.1	312.6	0.014	0.019	0.018
pt4	0.972	1.067	1.188	0.985	297.6	309.9	652.7	631.2	368.8	307	0.016	0.023	0.021
pt5	0.972	0.981	1.067	0.979	297.7	345.5	501.1	518	435	350.1	0.011	0.007	0.006
pt6	0.972	1.013	1.107	0.981	297.6	343.6	593.3	570.8	461.4	339	0.013	0.013	0.012
pt7	0.972	1.081	1.212	0.985	297.4	325.8	654	621.7	435.6	321.8	0.018	0.018	0.017
pt8	0.972	1.176	1.339	0.991	297.3	312.7	699.7	665.3	386.3	311.8	0.022	0.025	0.023
pt9	0.972	1.214	1.387	0.994	297.4	310.3	714.8	684.1	371	306.1	0.024	0.027	0.026
pt10	0.972	1.003	1.11	0.982	297.7	346.7	510.9	520.6	441.6	347.7	0.015	0.007	0.006
pt11	0.972	1.05	1.169	0.984	297.6	349.4	614	581.6	478.6	339.6	0.017	0.013	0.012
pt12	0.972	1.133	1.288	0.989	297.6	339.3	687.7	644.6	481.8	330.6	0.022	0.018	0.017
pt13	0.972	1.221	1.348	0.997	297.7	328.1	744.2	702.6	460.4	324.9	0.026	0.025	0.023
pt14	0.973	1.307	1.475	1.005	297.7	319.1	744.4	708.8	410.6	318.7	0.029	0.027	0.026
pt15	0.973	1.034	1.189	0.986	298	348.6	520.6	526.1	450.4	351.8	0.018	0.007	0.006
pt16	0.973	1.084	1.211	0.99	297.8	348.9	620.2	595.4	487.8	342.9	0.022	0.013	0.012
pt17	0.973	1.197	1.347	0.997	297.7	344.4	694.9	657.7	504.8	338.6	0.027	0.019	0.018
pt18	0.973	1.321	1.483	1.005	297.8	344	754.8	706.7	515.4	341.2	0.03	0.024	0.023
pt19	0.973	1.44	1.675	1.013	297.9	340.2	764.8	711.2	500.3	337.9	0.034	0.027	0.026
pt20	0.973	1.077	1.271	0.994	299.4	353.1	534.7	531.8	450.5	354.1	0.022	0.007	0.006
pt21	0.973	1.126	1.266	0.999	299	354	636.2	607.8	489.2	348.5	0.026	0.013	0.012
pt22	0.973	1.219	1.327	1.003	298.8	349.5	710.9	670.7	507.8	345.7	0.03	0.018	0.017
pt23	0.973	1.393	1.552	1.018	298.9	351.8	767.6	717	525	347	0.035	0.024	0.022
pt24	0.973	1.641	1.955	1.034	298.9	348.3	779.6	711.9	501.1	343.6	0.044	0.03	0.029
pt25	0.973	1.789	2.139	1.047	299.3	339.6	764.2	698	424.2	330.1	0.054	0.034	0.033
pt26	0.974	1.066	1.213	0.996	299.2	351	540.5	545.6	456.7	350.5	0.027	0.007	0.006
pt27	0.974	1.107	1.21	1.001	298.9	349.2	641.9	623.1	494.3	344.5	0.031	0.013	0.012
pt28	0.974	1.203	1.287	1.013	298.7	344.8	718.2	691	513.8	343.5	0.036	0.018	0.017
pt29	0.974	1.434	1.545	1.026	298.8	355.3	775.1	728.4	546.2	352.6	0.042	0.024	0.022
pt30	0.974	1.742	1.99	1.047	299.1	362.2	801.6	729.5	547.4	352.4	0.052	0.031	0.029
pt31	0.974	1.86	2.16	1.08	299.6	342.3	744.6	691.9	424.9	335.9	0.067	0.034	0.032
pt32	0.974	1.13	1.341	1	299.4	353.7	543.1	526.9	465	353.6	0.031	0.007	0.006
pt33	0.974	1.196	1.347	1.008	299.1	354	638.2	604.7	505.6	349.4	0.037	0.013	0.012
pt34	0.974	1.301	1.412	1.02	299	356.8	720.6	681.2	540.9	350.9	0.042	0.018	0.016
pt35	0.975	1.605	1.788	1.041	299.2	372.5	777.2	713.3	578	362.1	0.051	0.024	0.023
pt36	0.975	1.862	2.143	1.078	299.5	352.3	762.6	694.4	477.6	344.4	0.069	0.03	0.029
pt37	0.975	1.969	2.277	1.102	300.3	349.4	752.1	690.1	417.1	338.5	0.079	0.034	0.033
pt38	0.975	1.097	1.268	1.008	299.7	345.8	540.9	536	457	344.9	0.037	0.008	0.006
pt39	0.975	1.204	1.351	1.017	299.4	349.7	636	606.2	500.1	347	0.043	0.013	0.012
pt40	0.975	1.289	1.402	1.032	299.4	344.3	709.8	680.6	512	343.5	0.05	0.018	0.016
pt41	0.975	1.611	1.772	1.055	299.5	362.7	756.5	699.9	553.1	360.5	0.058	0.024	0.024
pt42	0.975	1.92	2.243	1.114	300.6	347.6	729.7	669.3	430.3	344.7	0.082	0.031	0.031
pt43	0.975	2.019	2.363	1.124	301.4	354.6	749.7	682.3	391.5	341.9	0.086	0.034	0.034
pt44	0.975	1.172	1.417	1.016	300.4	343.8	549.3	531.1	452.7	342.9	0.046	0.008	0.007
pt45	0.975	1.304	1.465	1.028	300.1	348.6	634.9	596.9	489.8	349.7	0.051	0.013	0.012
pt46	0.975	1.374	1.541	1.056	299.7	343.4	699.2	658.9	490.4	340.5	0.061	0.019	0.017
pt47	0.975	1.704	1.979	1.094	300	342.7	727.6	675.2	438.1	339.6	0.078	0.024	0.024
pt48	0.975	1.999	2.285	1.138	301.2	352.1	737.6	674.5	388.2	347.5	0.09	0.031	0.031
pt49	0.975	1.261	1.588	1.043	300	329.8	548.2	512.8	422.9	344.1	0.063	0.009	0.007
pt50	0.975	1.337	1.607	1.058	299.7	330.6	622.4	584.9	426.3	345.9	0.067	0.013	0.012
pt51	0.975	1.477	1.771	1.084	300	330.3	670.2	630.8	380.2	334.6	0.078	0.019	0.018
pt52	0.975	1.71	2.043	1.115	300.6	341.6	710.5	666.3	363.2	336.6	0.088	0.025	0.025
pt53	0.975	1.998	2.399	1.152	301.6	358.4	750.5	691.2	365.1	346.7	0.097	0.032	0.032
ref1	0.971	1.808	2.165	1.12	298.4	343.1	703	646.7	430.7	347	0.083	0.024	0.024
ref2	0.973	1.631	1.895	1.102	300.1	339.1	707.3	666.1	383.2	331.2	0.079	0.024	0.024
ref3	0.975	1.629	1.842	1.072	300.9	338.5	718.7	675.3	397.8	337.5	0.076	0.024	0.024
ref4	0.975	1.622	1.887	1.085	300.4	338.3	715.8	668.2	403.3	339	0.077	0.024	0.024

Table A.1: **OM611 with reference fuel:** steady state operating parameters

	NO_x ppm	$BSEC$ g/kWh	$[EC]$ mg/m^3	DR -	FSN -	KL_{end} -	KL_{max} -	γ_{ox} -	K_{end} m^{-1}	K_{max} m^{-1}
				OM611 - Reference Fuel - 3 of 3						
pt1	55.28	0.68	37.4	35.68	2.71	0.026	0.155	5.955	0.001	0.008
pt2	120.2	0.81	75.32	34.62	4.12	0.036	0.353	9.847	0.002	0.02
pt3	430.1	0.367	34.86	33.61	2.88	0.025	0.421	17.08	0.001	0.019
pt4	721.9	0.256	24.22	33.67	2.26	0.023	0.409	17.59	0.001	0.019
pt5	96.41	0.287	16.53	34.91	1.67	0.018	0.194	10.69	0.001	0.011
pt6	112.7	0.506	45.71	34.26	3.03	0.027	0.299	11.23	0.001	0.016
pt7	274.7	0.342	32.59	32.87	2.89	0.025	0.39	15.52	0.001	0.018
pt8	654.4	0.15	14.49	30.89	1.91	0.017	0.441	26.03	0.001	0.019
pt9	783.2	0.138	12.85	30.3	1.63	0.017	0.442	26.6	0.001	0.019
pt10	98.98	0.234	12.86	33.53	1.53	0.014	0.157	11.04	0.001	0.007
pt11	108.5	0.585	48.68	33.01	2.98	0.025	0.269	10.94	0.001	0.014
pt12	185	0.571	51.31	31.47	3.25	0.032	0.399	12.49	0.002	0.019
pt13	340.1	0.544	50.63	29.36	3.29	0.033	0.431	13.01	0.002	0.02
pt14	527.5	0.196	18.1	27.92	1.85	0.02	0.431	21.78	0.001	0.019
pt15	107.2	0.27	13.74	32.51	1.52	0.014	0.159	11.74	0.001	0.007
pt16	125.8	0.428	32.72	31.01	2.5	0.021	0.247	11.89	0.001	0.012
pt17	200	0.327	27.71	29.24	2.29	0.023	0.408	17.58	0.001	0.019
pt18	272.2	0.432	40.45	27.51	2.57	0.024	0.446	18.32	0.001	0.019
pt19	360.8	0.259	24.21	25.76	2.23	0.023	0.453	19.61	0.001	0.02
pt20	106.6	0.367	17.17	31.74	1.64	0.017	0.107	6.301	0.001	0.005
pt21	121.6	0.449	32.74	29.84	2.64	0.022	0.302	13.82	0.001	0.015
pt22	179.2	0.393	33.29	27.72	2.61	0.022	0.41	18.91	0.001	0.019
pt23	254.1	0.422	38.18	25.2	2.72	0.025	0.454	18.02	0.001	0.02
pt24	406.4	0.188	17.17	22.47	1.86	0.022	0.461	20.78	0.001	0.02
pt25	739.6	0.044	3.801	19.49	0.64	0.013	0.48	36.5	0.001	0.019
pt26	105.1	0.299	12.96	29.8	1.61	0.015	0.122	8.009	0.001	0.005
pt27	134	0.315	21.16	27.73	2.22	0.019	0.289	14.96	0.001	0.014
pt28	200.8	0.311	24.36	25.06	2.13	0.021	0.388	18.08	0.001	0.017
pt29	265.9	0.381	32.54	22.72	2.91	0.026	0.448	17	0.001	0.019
pt30	377	0.271	23.49	19.72	2.26	0.026	0.464	17.77	0.001	0.019
pt31	863	0.035	2.806	16.02	0.5	0.012	0.442	37.04	0	0.016
pt32	100.3	0.312	13.45	28.94	1.67	0.016	0.13	7.938	0.001	0.006
pt33	133.6	0.32	20.58	26.58	1.99	0.02	0.276	14.06	0.001	0.013
pt34	187.8	0.356	26.7	23.99	2.35	0.022	0.379	16.86	0.001	0.017
pt35	249.3	0.467	37.23	20.82	2.54	0.033	0.403	12.17	0.002	0.02
pt36	545.1	0.092	7.189	15.8	1.11	0.016	0.436	27.98	0.001	0.017
pt37	794.9	0.054	4.246	13.85	0.79	0.013	0.463	36.42	0	0.016
pt38	112.6	0.132	5.082	26.82	0.9	0.013	0.094	6.93	0.001	0.004
pt39	150	0.253	15.36	24.49	1.69	0.017	0.256	14.96	0.001	0.012
pt40	243.5	0.229	16.15	21.11	1.85	0.018	0.366	20.84	0.001	0.016
pt41	269.2	0.202	16.07	18.51	1.9	0.017	0.396	23.68	0.001	0.016
pt42	646.2	0.057	4.465	12.97	0.79	0.011	0.42	37.59	0	0.015
pt43	725.5	0.054	4.393	11.94	0.65	0.011	0.437	40.98	0	0.015
pt44	114	0.19	6.665	24.14	0.97	0.012	0.089	7.484	0	0.004
pt45	159.6	0.268	15.25	22.33	1.66	0.016	0.208	12.63	0.001	0.009
pt46	263	0.207	13.89	18.56	1.73	0.017	0.338	19.65	0.001	0.014
pt47	412.6	0.099	7.011	14.13	0.94	0.012	0.345	28.76	0	0.013
pt48	641.4	0.052	4.084	11.7	0.68	0.011	0.399	37.03	0	0.014
pt49	131.5	0.211	6.45	19.65	0.98	0.011	0.105	9.387	0	0.004
pt50	201.9	0.194	9.47	17.02	1.2	0.013	0.207	15.38	0.001	0.008
pt51	348.2	0.132	7.998	14.77	1.14	0.014	0.328	23	0.001	0.013
pt52	489.7	0.084	5.745	12.79	0.88	0.011	0.355	31.71	0	0.013
pt53	691	0.054	4.227	10.9	0.71	0.01	0.406	38.95	0	0.015
ref1	493.5	0.119	8.383	11.47	0.82	0.01	0.319	31.87	0	0.011
ref2	474.8	0.084	5.884	13.29	1.01	0.011	0.352	30.79	0	0.013
ref3	463.1	0.079	5.556	14.51	0.88	0.012	0.345	29.64	0	0.013
ref4	463.3	0.083	5.955	14.81	0.99	0.011	0.361	31.59	0	0.013

Table A.1: **OM611 with reference fuel:** steady state operating parameters

	ω rpm	M_e Nm	λ -	λ_{ox} -	EGR -	p_{rail} bar	SOI_{main} CAD bTDC	SOI_p CAD bTDC	τ_{main} μs	τ_p μs
						OM611 - Fuel Two - 1 of 3				
pt1	1001	31.94	2.24	3.658	0.35	300.3	-0.492	9.613	626.6	324
pt2	999.1	70.04	1.811	2.571	0.18	335.1	0.56	10.65	810.8	300.9
pt3	1000	103.7	1.698	2.24	0.025	379.1	1.594	11.69	892	270.3
pt4	1002	120.2	1.549	2.081	0.002	410.2	2.484	12.6	927.7	257.4
pt5	1249	31.3	2.548	4.284	0.329	386.3	-0.119	12.74	489.8	260.2
pt6	1248	67.98	1.726	2.615	0.255	422.6	0.21	13.07	648.4	253.5
pt7	1249	103.4	1.59	2.334	0.124	480.2	1.311	14.19	719.5	235
pt8	1248	137.5	1.477	2.08	0.018	574	2.273	15.14	754.1	211
pt9	1249	153.4	1.441	1.969	0.002	636	2.921	15.78	768.4	198.1
pt10	1498	34.29	2.506	4.421	0.313	443.4	-0.038	15.61	459.9	245.9
pt11	1498	68.76	1.763	2.799	0.255	470.1	0.277	15.93	597.7	240.8
pt12	1499	104.1	1.552	2.346	0.15	537.8	1.378	17.01	661.7	221.3
pt13	1499	138.5	1.429	2.013	0.095	651.2	2.484	18.14	697.6	194.6
pt14	1499	154.1	1.476	2.045	0.061	687	2.759	18.42	723.2	193.2
pt15	1749	33.89	2.606	4.774	0.302	478.8	0.307	18.76	431.6	235.6
pt16	1749	66.77	1.838	2.954	0.258	506.8	0.703	19.16	559.3	230.2
pt17	1749	102.7	1.552	2.318	0.189	586	1.849	20.3	617.5	209.7
pt18	1749	137.6	1.419	2.017	0.141	698.4	3.053	21.5	656.6	192.3
pt19	1748	152.4	1.441	1.988	0.124	730.2	3.502	21.93	677.5	189.4
pt20	1999	33.78	2.657	5.185	0.258	500.6	0.756	22.03	413.9	229.2
pt21	2001	69.51	1.85	3.149	0.243	533.8	1.269	22.54	552.6	222.9
pt22	1999	103.9	1.572	2.36	0.216	641.5	2.526	23.8	595.1	200.3
pt23	2000	137.1	1.449	2.09	0.193	752	3.831	25.09	627.2	188.4
pt24	1999	170.9	1.542	2.056	0.118	826	5.737	27.02	714.2	185.4
pt25	1999	187.4	1.776	2.355	0.028	825.1	6.291	27.53	768	185.4
pt26	2249	35.64	2.65	5.009	0.264	517.2	2.024	26.05	417.8	225.9
pt27	2248	68.39	1.93	3.141	0.253	565.1	2.696	26.72	518.9	214.4
pt28	2249	104.6	1.635	2.448	0.226	680.2	3.802	27.9	571.6	195.6
pt29	2250	136.4	1.547	2.189	0.188	779.4	5.182	29.19	615.4	186
pt30	2249	171.4	1.794	2.394	0.072	830.3	6.767	30.8	705.7	185.4
pt31	2249	189.3	1.91	2.478	0.001	847.7	7.217	31.24	761.1	184.5
pt32	2498	33.88	2.804	5.132	0.248	543.3	3.593	30.35	401.7	218.8
pt33	2498	69.54	2.002	3.179	0.241	616.1	4.27	31.03	496	203.8
pt34	2498	103.9	1.728	2.602	0.205	718	5.299	32.06	551.5	191.2
pt35	2499	136.4	1.585	2.25	0.18	819.6	6.488	33.26	601	185.4
pt36	2497	171.3	2.118	2.626	0.001	858.1	7.717	34.46	696.7	184.5
pt38	2748	36.29	2.855	5.05	0.22	590.8	4.754	34.26	387.3	206.7
pt39	2748	68.48	2.2	3.481	0.207	653.6	5.795	35.28	470.7	194.8
pt40	2748	101.8	1.904	2.861	0.186	743.2	6.868	36.37	526.1	189.1
pt41	2748	136.2	1.691	2.359	0.15	832.8	7.934	0	614.7	0
pt42	2748	171.1	2.063	2.542	0.001	889.3	8.45	0	714.8	0
pt44	2999	34.2	3.278	5.344	0.17	621.9	5.508	37.8	380.4	200
pt45	3001	67.54	2.41	3.682	0.16	694.2	6.676	38.95	457.4	193
pt46	2999	102.4	2.066	3.006	0.094	775.7	7.805	40.07	514.9	186.5
pt47	2998	136	2.038	2.781	0.045	853.1	8.973	0	599.8	0
pt48	3000	171.5	2.057	2.529	0.001	958.3	9.557	0	688.8	0
pt49	3248	33.42	4.323	5.754	0.001	649.3	6.245	41.3	381.7	195.3
pt50	3250	69.44	2.726	4.194	0.069	729.1	7.329	42.38	445.5	190.8
pt51	3249	103.1	2.383	3.326	0.001	805.4	8.55	43.59	505.5	185.4
pt52	3249	136.2	2.23	2.878	0.001	893.8	10.24	0	599.2	0
pt53	3249	168.9	2.058	2.507	0.001	1036	10.84	0	666.8	0
ref1	2999	137.2	2.251	2.896	0.001	859.6	9.074	0	605.7	0
ref2	2998	136.8	2.445	3.155	0.001	859.2	9.082	0	606	0
ref3	2999	137.1	2.115	2.851	0.009	848.7	8.994	0	603	0
ref4	2999	139.2	2.16	2.836	0.001	860.3	9.071	0	608.6	0

Table A.2: **OM611 with fuel two:** steady state operating parameters

	p_{amb} bar	p_{im} bar	p_{em} bar	p_{exh} bar	T_{amb} K	T_{im} K	T_{em} K	T_{exh} K	T_{egr} K	T^*_{ivc} K	m_{air} g/s	m_f g	m_{main} g
							OM611 - Fuel Two - 2 of 3						

	p_{amb} bar	p_{im} bar	p_{em} bar	p_{exh} bar	T_{amb} K	T_{im} K	T_{em} K	T_{exh} K	T_{egr} K	T^*_{ivc} K	m_{air} g/s	m_f g	m_{main} g
pt1	0.961	0.958	1.023	0.966	298	348	498.5	535.2	429	360.5	0.009	0.008	0.006
pt2	0.961	0.983	1.06	0.969	297.8	329.3	569.7	563.7	421.3	328.8	0.011	0.014	0.013
pt3	0.961	1.027	1.126	0.972	297.7	311.5	603.9	591.4	373.7	311.7	0.015	0.019	0.018
pt4	0.96	1.055	1.176	0.974	297.7	308.2	632.8	614.4	357.4	310.6	0.016	0.022	0.021
pt5	0.96	0.972	1.06	0.968	297.6	338.3	491.6	518.7	423.7	352.8	0.011	0.007	0.006
pt6	0.96	1.002	1.097	0.97	297.6	337.2	578.5	556.1	445.5	338.3	0.014	0.013	0.011
pt7	0.96	1.071	1.207	0.974	297.4	320.6	638.3	604.6	412.8	321	0.018	0.018	0.016
pt8	0.96	1.133	1.252	0.98	297.2	309.4	684.4	657.1	374.3	311	0.022	0.023	0.022
pt9	0.96	1.212	1.389	0.983	297.2	308	702.1	672.7	359.9	314.1	0.024	0.026	0.025
pt10	0.96	0.996	1.115	0.973	297.4	342.3	513.4	534.1	438.1	348.8	0.015	0.007	0.006
pt11	0.96	1.04	1.177	0.972	297.2	342	599.5	573.1	462	340.7	0.018	0.012	0.011
pt12	0.96	1.1	1.196	0.978	297.2	329.3	674.2	643.3	454.5	327.8	0.022	0.017	0.016
pt13	0.96	1.213	1.343	0.985	297.1	320.7	725.6	686.2	424.3	321.7	0.026	0.023	0.022
pt14	0.96	1.305	1.49	0.991	297.2	316.6	728	688.6	395.5	317.1	0.029	0.026	0.025
pt15	0.96	1.022	1.176	0.974	297.4	346.3	520.2	525.5	446.5	346.5	0.019	0.007	0.006
pt16	0.96	1.088	1.26	0.977	297.4	349.5	610.7	579.6	480.1	346.1	0.021	0.012	0.011
pt17	0.96	1.155	1.282	0.984	297.4	342.1	692.5	652.4	493.5	336.8	0.026	0.017	0.016
pt18	0.96	1.287	1.427	0.992	297.5	337.9	749.1	698	493.8	336.6	0.03	0.023	0.021
pt19	0.96	1.379	1.564	0.998	297.6	333.7	756	705	472.4	336.5	0.033	0.025	0.024
pt20	0.959	1.062	1.274	0.971	297.7	351.4	527.8	520.6	449.7	353.6	0.023	0.007	0.006
pt21	0.959	1.163	1.397	0.983	297.4	355.2	627.4	583.4	490.4	421.2	0.025	0.012	0.011
pt22	0.959	1.312	1.562	0.985	297.4	359.8	711.3	651.6	526.8	356.6	0.03	0.018	0.016
pt23	0.959	1.476	1.757	0.996	297.4	362.1	767.2	696.6	545.8	357.8	0.035	0.023	0.021
pt24	0.959	1.689	2.09	1.021	297.7	348.4	768.8	692.1	497.4	344.1	0.046	0.029	0.028
pt25	0.959	1.865	2.431	1.041	298.1	340.8	746.1	667.1	387.8	330.7	0.056	0.031	0.03
pt26	0.959	1.122	1.362	0.983	298.4	357.8	550.5	544.3	469.1	360.6	0.027	0.007	0.006
pt27	0.959	1.234	1.494	0.987	298.1	362.7	636.6	591.1	511.4	360	0.031	0.012	0.011
pt28	0.959	1.413	1.704	0.997	298.1	368.6	715.5	650.1	546.6	368.7	0.036	0.018	0.016
pt29	0.96	1.586	1.89	1.012	298.2	368	762.9	687	559.3	365.1	0.043	0.023	0.022
pt30	0.96	1.885	2.409	1.047	298.7	350.7	751.3	666.3	472.7	345.5	0.061	0.029	0.028
pt31	0.96	1.98	2.485	1.068	298.9	348	740.4	661.6	416.3	342.5	0.07	0.031	0.03
pt32	0.96	1.122	1.333	0.988	298.9	356.4	546.7	540.7	467.4	356.9	0.031	0.007	0.006
pt33	0.96	1.25	1.462	0.995	298.4	361.9	639.9	597.6	516.1	358.3	0.036	0.013	0.011
pt34	0.96	1.427	1.641	1.01	298.4	368.4	716.2	659.2	553.3	363.7	0.043	0.017	0.016
pt35	0.96	1.618	1.843	1.025	298.4	372.2	767.5	696	572	365.8	0.05	0.023	0.022
pt36	0.96	2.025	2.552	1.087	298.9	350.4	725.4	645.7	442.1	353.5	0.077	0.029	0.028
pt38	0.96	1.147	1.366	0.993	298.2	350.1	548.5	526.6	468.9	353.3	0.037	0.008	0.007
pt39	0.96	1.281	1.493	1.004	298.1	355.6	630.2	586.4	511.4	358.8	0.042	0.012	0.011
pt40	0.96	1.466	1.689	1.02	298.1	360.1	690.4	630.6	535.4	363.5	0.049	0.017	0.015
pt41	0.96	1.621	1.797	1.039	298.4	364	748.8	686.6	552.5	360.8	0.058	0.023	0.023
pt42	0.96	1.926	2.262	1.098	298.7	347.6	724.8	660.8	434.4	351.3	0.082	0.029	0.029
pt44	0.96	1.163	1.425	1.005	298.4	336.9	540.9	517.3	447.4	341.4	0.046	0.008	0.007
pt45	0.96	1.28	1.518	1.009	298.3	340.9	617.4	577.7	474.9	346	0.051	0.012	0.011
pt46	0.96	1.366	1.552	1.027	298.5	335.6	684.2	644.6	467	341.9	0.059	0.017	0.015
pt47	0.96	1.662	1.916	1.079	298.8	339.5	716.7	663.8	447.2	347.9	0.073	0.023	0.023
pt48	0.96	1.95	2.394	1.111	299.5	348.8	732.9	666.5	384.8	352.2	0.087	0.029	0.029
pt49	0.96	1.252	1.619	1.045	299.7	327.4	544.8	525	355.1	348.2	0.057	0.008	0.007
pt50	0.96	1.319	1.588	1.042	299.4	330	616.4	579.4	409.2	327.5	0.069	0.013	0.011
pt51	0.96	1.415	1.701	1.064	299.3	328.4	664.4	633.9	364.5	332.2	0.075	0.017	0.016
pt52	0.96	1.703	2.042	1.101	299.6	340.2	702.1	657.5	355.6	339.5	0.087	0.023	0.023
pt53	0.96	1.96	2.371	1.133	300.2	354.8	743.4	680.3	359.3	349.9	0.094	0.03	0.03
ref1	0.96	1.68	2.007	1.097	298.5	340.6	696.3	649.6	382.3	337.7	0.081	0.023	0.023
ref2	0.957	1.893	2.392	1.106	297.9	348.5	686.7	619.4	410.1	349.2	0.088	0.023	0.023
ref3	0.96	1.636	1.905	1.067	298.8	337.3	704.7	657.4	393.9	339.4	0.076	0.023	0.023
ref4	0.961	1.668	1.98	1.078	299.5	339.3	698.8	652.3	387.5	340.9	0.079	0.023	0.023

Table A.2: **OM611 with fuel two:** steady state operating parameters

	NO_x ppm	$BSEC$ g/kWh	$[EC]$ mg/m^3	DR -	FSN -	KL_{end} -	KL_{max} -	γ_{ox} -	K_{end} m^{-1}	K_{max} m^{-1}
				OM611 - Fuel Two - 3 of 3						
pt1	62.99	0.334	18.55	46.14	1.65	0.019	0.092	4.754	0.001	0.005
pt2	164.2	0.227	19.6	45.27	1.62	0.016	0.223	14.03	0.001	0.011
pt3	687.3	0.082	7.576	42.39	1.01	0.011	0.303	28.81	0	0.013
pt4	888.1	0.145	13.96	42.38	1	0.011	0.291	26.43	0	0.015
pt5	82.16	0.129	6.786	45.68	0.91	0.012	0.078	6.452	0.001	0.004
pt6	108.4	0.246	21.88	44.42	1.85	0.015	0.169	11.16	0.001	0.009
pt7	306.7	0.133	12.8	42.22	1.45	0.013	0.311	23.5	0.001	0.014
pt8	772.9	0.082	7.863	39.14	1.02	0.011	0.294	25.68	0	0.015
pt9	911.7	0.051	5.026	38.39	0.86	0.015	0.26	17.59	0.001	0.016
pt10	81.81	0.115	5.852	43.75	0.8	0.011	0.071	6.4	0	0.003
pt11	104.1	0.212	17.33	43.11	1.69	0.016	0.156	9.964	0.001	0.008
pt12	218.8	0.175	15.58	39.97	1.62	0.015	0.305	19.98	0.001	0.014
pt13	396.9	0.225	21.36	36.93	2.03	0.019	0.291	15.49	0.001	0.016
pt14	552.4	0.108	10.1	35.07	1.18	0.015	0.3	20.42	0.001	0.015
pt15	83.52	0.1	4.71	42.54	0.66	0.011	0.045	4.045	0	0.002
pt16	96.74	0.206	15.55	40.9	1.55	0.015	0.155	10.2	0.001	0.008
pt17	165.6	0.247	21.3	37.8	1.8	0.016	0.3	18.86	0.001	0.014
pt18	260.5	0.346	32.32	34.54	2.49	0.019	0.318	16.83	0.001	0.016
pt19	354.4	0.224	21.19	32.75	2.21	0.019	0.312	16.69	0.001	0.016
pt20	93.88	0.072	3.28	41.52	0.66	0.015	0.112	7.591	0.001	0.005
pt21	104.3	0.233	18.02	39.34	1.68	0.022	0.536	24.62	0.001	0.023
pt22	138.7	0.343	29.1	36.12	2.37	0.024	0.921	37.96	0.001	0.037
pt23	193.2	0.425	38.61	32.37	2.83	0.033	1.087	33.05	0.002	0.041
pt24	432	0.098	8.833	26.75	1.19	0.026	1.182	45.88	0.001	0.04
pt25	816.9	0.011	0.91	22.08	0.28	0.009	0.372	40.51	0	0.013
pt26	91.88	0.078	3.477	38.92	0.68	0.011	0.029	2.77	0	0.001
pt27	106.7	0.252	16.93	37.05	1.66	0.015	0.159	10.46	0.001	0.008
pt28	142.6	0.302	25.18	33.14	2.22	0.016	0.285	17.66	0.001	0.013
pt29	216.2	0.292	25.39	29.15	2.16	0.017	0.335	20.1	0.001	0.015
pt30	572.4	0.037	3.048	21.32	0.64	0.01	0.351	33.88	0	0.013
pt31	862.6	0.019	1.565	18.16	0.31	0.009	0.345	37.69	0	0.012
pt32	96.19	0.05	2.054	36.81	0.43	0.01	0.026	2.574	0	0.001
pt33	118.2	0.198	12.97	34.23	1.45	0.014	0.154	10.99	0.001	0.007
pt34	171.5	0.219	16.82	29.53	1.77	0.015	0.27	17.65	0.001	0.012
pt35	232.9	0.268	22.07	25.79	1.99	0.016	0.321	19.7	0.001	0.014
pt36	731.3	0.026	2.032	15.87	0.34	0.009	0.303	31.97	0	0.01
pt38	108	0.036	1.498	34.47	0.45	0.01	0.028	2.954	0	0.001
pt39	144.8	0.133	8.312	30.78	1.12	0.014	0.137	9.937	0.001	0.006
pt40	204.5	0.146	11.03	26.33	1.42	0.013	0.216	16.05	0.001	0.009
pt41	277.1	0.115	9.199	22.25	1.22	0.012	0.279	23.98	0	0.011
pt42	663.6	0.055	4.305	14.87	0.86	0.009	0.29	32.55	0	0.01
pt44	123.2	0.021	0.74	29.25	0.24	0.008	0.016	1.967	0	0.001
pt45	169.9	0.09	5.1	26.32	0.76	0.011	0.092	8.219	0	0.004
pt46	280.9	0.073	4.92	21.67	0.82	0.011	0.181	16.15	0	0.007
pt47	397.2	0.053	3.917	16.79	0.52	0.009	0.225	24.18	0	0.008
pt48	654.6	0.047	3.783	12.48	0.59	0.009	0.279	32.64	0	0.01
pt49	154.9	0.031	0.964	20.31	0.24	0.008	0.028	3.626	0	0.001
pt50	205.3	0.085	4.111	20.25	0.76	0.011	0.092	8.779	0	0.003
pt51	377.4	0.054	3.312	17.21	0.61	0.01	0.174	17.6	0	0.006
pt52	508.4	0.05	3.49	13.9	0.58	0.009	0.218	24.16	0	0.008
pt53	690.4	0.04	3.169	11.91	0.49	0.008	0.274	32.93	0	0.009
ref1	496.6	0.047	3.292	14.51	0.53	0.009	0.214	23.88	0	0.007
ref2	502.3	0.039	2.641	13.44	0.45	0.009	0.196	21.69	0	0.007
ref3	476.6	0.045	3.23	15.81	0.51	0.009	0.219	23.58	0	0.008
ref4	530.7	0.032	2.274	15.55	0.44	0.009	0.229	25.73	0	0.008

Table A.2: **OM611 with fuel two:** steady state operating parameters

A.2   Vehicle Model Parameters

Aerodynamic drag coefficient	C_d	0.4	-
Rolling resistance coefficient	C_r	0.01	-
Frontal area	A_f	2	m^2
Vehicle mass	m_v	1800	kg
Wheel radius	r_w	0.4	m
Differential gear ratio	R_{diff}	2.65	-
	$R_{trans,1}$	5.010	-
Transmission gear ratio	$R_{trans,2}$	2.830	-
	$R_{trans,3}$	1.790	-

Table A.3: Parameters used for the vehicle dynamics model (see section 4.2.1)

A.3   PASS Validation Measurements

To validate the AVL MSS and Dekati FPS system, simultaneous coulometric/gravimetric and MSS measurements were carried out on a well characterized test engine. The measurements were carried out on a Liebherr D914T, as outlined in table A.4. The considered operating points are listed in table A.5, while the resulting particle and soot measurements are giving in table A.6.

Maximum output	105 kW at 2000 rpm
Displacement	6.11 l
Number of cylinders	4
Bore	120 mm
Stroke	135 mm
Connecting rod length	228 mm
Compression ratio	15.9:1
Aspiration	Turbocharged
EGR System	N/A

Table A.4: Specifications of Liebherr D914T used for PASS validation measurements

	ω rpm	M_e Nm	m_{air} kg/h	$\dot{V}_{fuel}$ l/h	O_2 %	NO ppm	NOx ppm	p_{amb} mbar
1	1406	296	306	11.32	12.6	1240	1300	964
2	1002	150	184	4.75	15.36	780	860	964
3	1005	285	194	7.89	11.92	1450	1530	964
4	1007	345	202	9.33	10.46	1720	1800	964
5	1000	422	210	11.33	8.72	2080	2150	964
6	1407	152	282	6.7	15.6	560	640	965
1W1	1407	297	311	11.06	12.72	1190	1260	965
7	1400	440	345	19.82	10.25	1940	2020	965
8	2000	250	506	15.12	14.02	700	750	965
9	1000	567	233	15.31	5.66	2380	2460	965
10	1400	618	390	22.3	7.61	2510	2590	965
11	2000	538	668	29.69	10.68	1550	1630	965
1W2	1400	296	309	11.16	12.63	1210	1280	965

Table A.5: Operating points considered during MSS validation measurements

	$\dot{m}_{PM}$ g/h	BSPM g/kWh	m_{OC} mg	m_{EC} mg	m_{TC} mg	OC/TC %	EC/TC %	EC/PM %	OC/PM %	$[EC]$ mg/m^3
1	2.95	0.068	0.150	0.235	0.385	39.0	61.0	37.6	24.1	1.73
2	1.83	0.116	0.300	0.251	0.551	54.4	45.6	38.8	46.3	1.89
3	3.98	0.133	0.225	0.859	1.084	20.8	79.2	65.1	17.1	6.66
4	5.73	0.158	0.184	1.387	1.571	11.7	88.3	76.0	10.1	9.70
5	10.17	0.230	0.199	2.544	2.744	7.3	92.7	82.5	6.5	18.29
6	3.01	0.135	0.303	0.201	0.504	60.1	39.9	28.1	42.4	1.17
1W1	3.31	0.076	0.214	0.287	0.502	42.8	57.2	42.6	31.8	1.43
7	4.87	0.076	0.171	0.516	0.687	24.8	75.2	57.5	19.0	3.41
8	5.71	0.109	0.206	0.416	0.622	33.1	66.9	56.8	28.1	3.33
9	34.13	0.575	0.433	8.193	8.626	5.0	95.0	88.6	4.7	51.10
10	11.33	0.125	0.242	1.356	1.598	15.1	84.9	73.4	13.1	7.59
11	15.30	0.136	0.382	0.812	1.193	32.0	68.0	55.2	25.9	3.68
1W2	2.54	0.058	0.161	0.252	0.413	39.0	61.0	47.5	30.4	1.43

Table A.6: Gravimetric measurements for PASS validation. EC: Elementary Carbon; TC: Total Carbon; OC: Organic Carbon; PM:Particulate Matter. Coulometric measurements taken according to [99]. [EC] measured using AVL MSS included in this table for reference purposes.
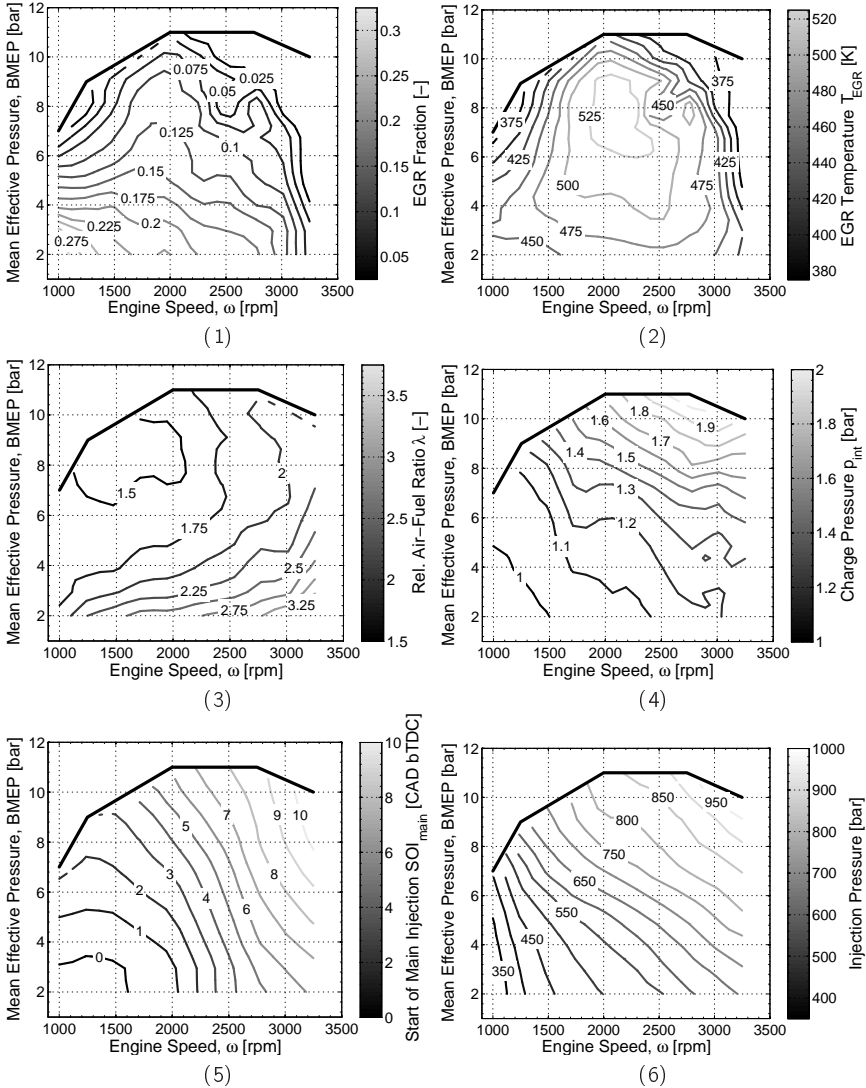
A.4   OM611 - Operating Maps

Figure A.1: OM611 steady state operating maps. (1) EGR rate; (2) EGR temperature; (3) relative air-fuel ratio; (4) intake charge pressure; (5) start of main injection; (6) injection rail pressure. Reference fuel
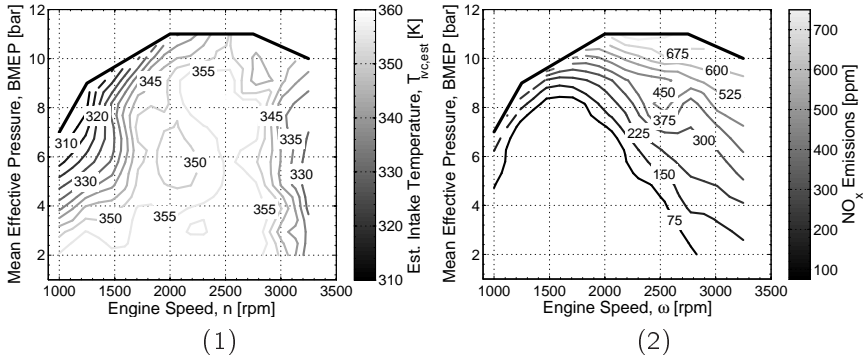
Figure A.2: OM611 steady state operating maps. (1) estimated intake charge temperature; (2) NOx emissions. Reference fuel

A.5 OM611 - Transient Parameters

Shown in figures A.3, A.4 and A.5 are the charge pressures, EGR rates, and relative air fuel ratios during the acceleration and tip-in transients.
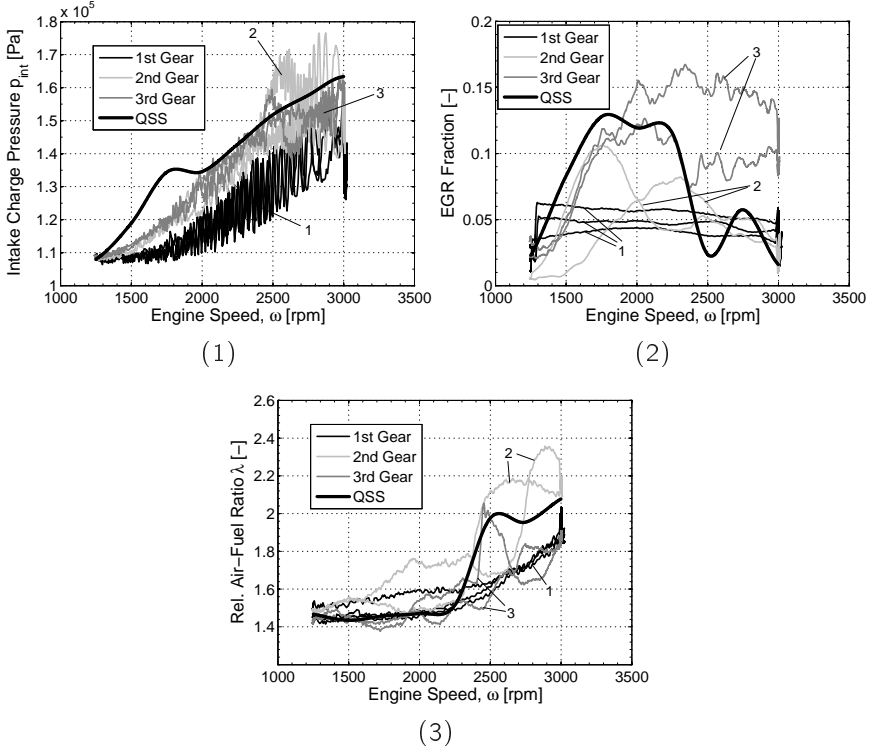

(1)

(2)

(3)

Figure A.3: Operating parameters during **acceleration transients**: (1) intake charge pressure; (2) EGR rate; (3) relative air-fuel ratio. OM611 with reference fuel.
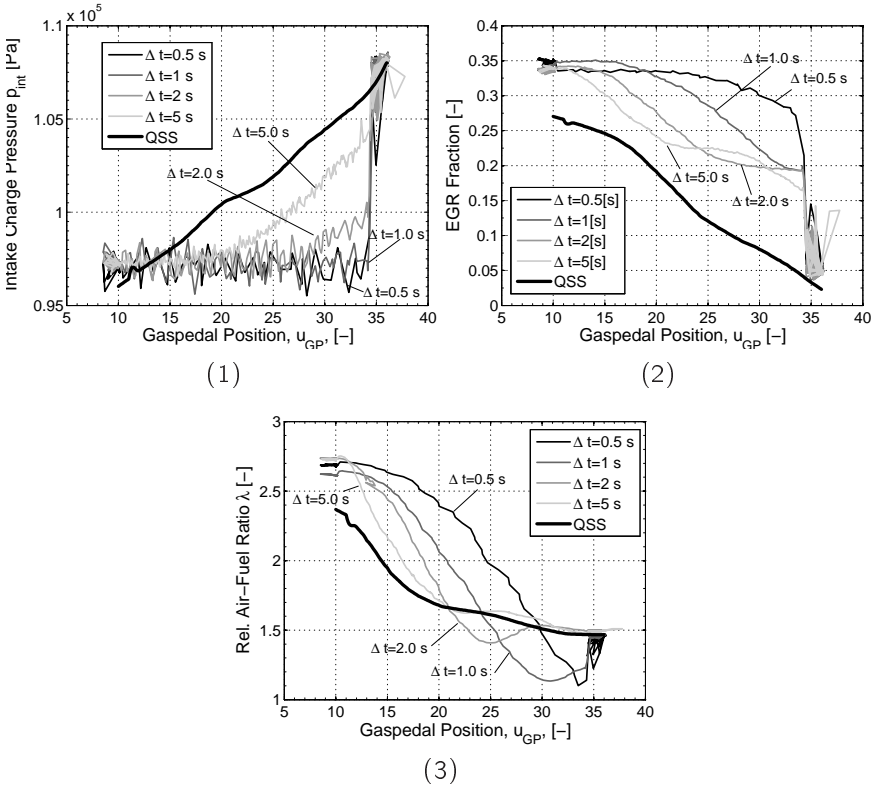
Figure A.4: Operating parameters during **tip-in transients at 1250 rpm**: (1) intake charge pressure; (2) EGR rate; (3) relative air-fuel ratio. OM611 with reference fuel.
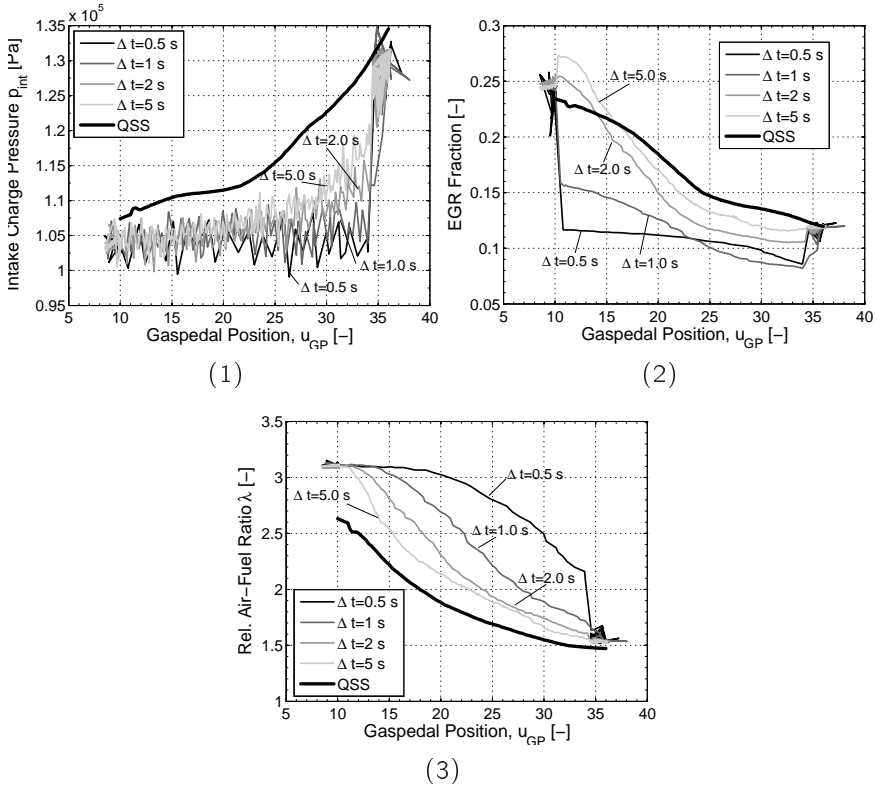
(1)

(2)

(3)

Figure A.5: Operating parameters during **tip-in transients at 2000 rpm**: (1) intake charge pressure; (2) EGR rate; (3) relative air-fuel ratio. OM611 with reference fuel.

A.6   Evolutionary Algorithm Parameters

Table A.7 outlines the parameters and details of the evolutionary algorithms used for the MVSM parameterization.

Objective function	Maximization of R^2
Initialization type	Stochastic
Number of individuals	200
Number of parents	100
Number of offspring	400
Fitness assignment	Linear ranking
Fitness selection pressure	1.75
Selection type	Tournament
Selection tournament size	20
Recombination type	Intermediate
Recombination range expansion factor	0.25
Mutation type	Continuous
Mutation domain adaptation type	Linear
Mutation domain adaptation rate	1...10
Mutation precision adaptation type	Linear
Mutation precision adaptation rate	0.2...0.05
Reinsertion type	Elitist
Reinsertion adaptation type	Linear
Reinsertion adaptation rate	0.8...0.4
Termination criteria	Number of generations (60)

Table A.7: Parameters of the evolutionary algorithm optimization routine. Descriptions of the various parameters can be found in [81]

Appendix B

CV and List of Publications

B.1   CV

Work Experience:

Research and Teaching Assistant - PhD Student
Mechanical Engineering, ETH Zurich, Switzerland   2005 - 2009

Teaching Assistant
Mechanical Engineering, University of Alberta   2002 - 2004

Research Engineer (Internship)
DaimlerChrysler AG, Stuttgart Germany   2001

Research Assistant - Combustion Research
Mechanical Engineering, University of Alberta   2000 - 2001

Education:

Ph.D. in Mechanical Engineering
ETH Zurich, Switzerland   2008

- Development and validation of a realtime model for the prediction of engine-out soot mass under steady state and transient operating conditions
- Measurement of in-cylinder and engine-out soot emissions from various engines (in-house and external)

M.Sc. in Mechanical Engineering
University of Alberta, Edmonton, Canada   2004

- Development, implementation, and validation of a thermo-kinetic model for the HCCI engine cycle

B.Sc. in Mechanical Engineering
University of Alberta, Edmonton, Canada   2001

- Mechanical Engineering, with focus on applied thermodynamics and combustion

High School Diploma
Bev Facey Composite High School, Sherwood Park, Canada   1996

B.2 Publications

B.2.1 Peer Reviewed Publications

1. P. Kirchen and K Boulouchos. Soot Emission Measurements and Validation of a Mean Value Soot Model for Common-Rail Diesel Engines during Transient Operation. *SAE 2009-01-1904*, 2009.

2. P. Kirchen and K Boulouchos. Development and Validation of a Phenomenological Mean Value Soot Model for Common-Rail Diesel Engines. *SAE 2009-01-1277*, 2009.

3. P. Kirchen and K Boulouchos. Phänomenologisches Mittelwertmodell für Ruß in transientem Motorbetrieb. *Motortechnische Zeitschrift*, 07-08(69):624–631, 2008.

4. A. Escher, P. Kirchen, and K Boulouchos. Experimental Investigations using a Transparent Single Shot Compression Machine for HCCI Combustion. *SAE*, (2007-24-0009), 2007.

5. A. Mayer, M. Kasper, T. Mosimann, F. Legerer, J. Czerwinski, L. Emmenegger, J. Mohn, A. Ulrich, and P. Kirchen. Nanoparticle Emission of Euro4 and Euro5 HDV Compared to Euro3 with and without DPF. *SAE 2007-01-1112*, 2007.

6. P. Kirchen, M. Shahbakhti, and C. R. Koch. A skeletal kinetic mechanism for PRF combustion in HCCI engines. *Combustion Science and Technology*, 179(6):1059–1083, 2007.

B.2.2 Conference Presentations and Publications

1. P. Kirchen and K Boulouchos. Phänomenologisches Modellierung der rohen Russemissionen eines Dieselmotors beim stationären und transienten Betrieb. In *17th Aachen Colloquium: Automobile and Engine Technology*, volume 1, pages 485–511, Aachen, Germany, 2008.

2. P. Kirchen and K Boulouchos. Erarbeitung eines Algorithmus zur Berechnung der Partikelbildung aus Motordaten. In *FVV Informationstagung Motoren*, volume R 541, pages 83–107, Frankfurt am Main, 2008. FVV.

3. P. Kirchen and K Boulouchos. Measurement and Analysis of Soot Emissions During Transient Operation of a Common Rail Passenger Car Diesel Engine. In *12th ETH Conference on Combustion Generated Nanoparticles*, Zurich, Switzerland, 2008.

4. P. Kirchen and K Boulouchos. Experimentelle Untersuchungen der Russemissionen des Common Rail Dieselmotors beim stationären und transienten Betrieb. In M. Bargende, editor, *11. Symposium Dieselmotorentechnik*, Ostfildern, Germany, 2008.

5. P. Kirchen, S. Walther, P. Obrecht, K Boulouchos, D. Karst, and C. Cavalloni. Correlation and Analysis of In-Cylinder and Engine-Out Soot Emission Measurements from a Multi-Cylinder Diesel Engine. In *8. Internationales Stuttgarter Symposium*, volume 2, pages 129–145, Stuttgart, Germany, 2008.

6. P. Kirchen, S. Walther, P. Obrecht, K Boulouchos, D. Karst, and C. Cavalloni. Measurement of the Instantaneous In-Cylinder Soot Temperature and Concentration in a Multi-Cylinder Engine. In *11th ETH Conference on Combustion Generated Nanoparticles*, Zurich, Switzerland, 2007.

7. P. Kirchen and K Boulouchos. Modellierung der rohen Russemissionen eines Dieselmotors. In *FVV Informationstagung Motoren*, volume R 537, Frankfurt am Main, 2007. FVV.